Diamond Growth in Low Pressure Flames

Thesis by

Nick Glumac

In Partial Fulfillment of the Requirements

for the Degree of

Doctor of Philosophy

California Institute of Technology

Pasadena, California

1994

(Submitted April 25, 1994)

Acknowledgements

The work described in this report was funded by grants from the National Science Foundation and Norton Corporation.

Many individuals deserve mention for their assistance in this work. First and foremost is my advisor, David Goodwin. I cannot express deeply enough my gratitude for the support, direction, and compassion which I received from Dave in my five years at Caltech. Working under Dave has been a positive, productive, and pleasant experience. I hope I can serve my future students as an advisor in the same way.

In my research, Evaldo Corat was of tremendous help in both carrying out some experiments as well as in tutoring me on the subtleties of optics, lasers, and signal processing. Insightful discussions with several others, including Mark Cappelli, Jay Jeffries, Steve Harris, and Joong Soo Kim, are gratefully acknowledged.

Personal support from those around me during the long years of my work here has made the Ph.D. experience very memorable. Deserving of special mention are some of my wonderful friends outside the institute: Michelle, Teresa, Tiffany, Lorena, Kim, Cindy, Susan, Pam, Ted, Suzanne, Marc, Neil, and Tim. They helped me much more than they know. Here at Caltech, Shifo and "Super" Dave Kaufman helped fill my graduate days with excitement, adventure, and plenty of laughs.

Lastly, I must acknowledge three very special people; Patti, Matt, and Farrell. I'll never forget the love, support, direction, and motivation, with which they provided me, especially when I really needed it. You made all of this possible.

The results of an experimental and computational study of diamond chemical vapor deposition in low pressure flames are presented. In acetylene/oxygen low pressure flat flames in a stagnation-point flow arrangement over a constant temperature substrate, experimental conditions were identified in which diamond particles and films were grown on the substrate surface. The effects of substrate temperature, burner to substrate distance, and equivalence ratio on the nature of the deposit were examined.

At low specific flow rates, only diamond particles on silicon and molybdenum substrates were grown. Only continuous non-diamond films were observed at these conditions. Diamond particle growth rates of up to 1 μm/hour (based on particle radius) were observed. The nucleation density in these flames was found to be low compared with other common diamond CVD methods. However, nucleation density was successfully increased by deposition of a small amount of non-diamond carbon on the surface early in growth experiments.

At higher specific flow rates, diamond films were deposited. Linear film growth rates of up to 1.0 μm/hour were observed. Film growth rates were observed to be temperature dependent. The diamond films exhibited excellent spatial uniformity of deposit quality and thickness. For the highest growth rate case, the deposition process required 40 standard liters of acetylene per milligram of diamond deposit. This deposition efficiency is comparable to those of atmospheric pressure torch reactors.

A flame model is used to analyze the experimental results. The model accounts for complex gas phase chemistry, some surface chemistry (including deposition and

etching of diamond and recombination of some radical species), and all transport processes. The results of the model were tested by diagnostic measurements using laser-induced fluorescence of OH and mass spectrometry. The flames tested were similar to those used to deposit diamond. The results of the diagnostic measurements indicate that the flame model predicts gas phase temperatures to within 175 K and that the predictions of the surface mole fractions of some important species are within experimental uncertainty. The predicted relative spatial OH concentration profile matches experiment very well, and the observed dependence of surface species mole fractions on equivalence ratio is well reproduced by the model for all measured species.

The model indicates that, at low specific flow rates, the acetylene/oxygen low pressure flat flame growth environment has a very low $[H]/[CH_3]$ ratio at the substrate and a large amount of surface $[O_2]$ as compared to other deposition methods. The results suggest that etching of non-diamond carbon by O_2 and possibly OH are essential reactions in the diamond growth process under these conditions. At the higher specific flow rates, the model predicts substantial increases in [H] and $[H]/[CH_3]$ and a significant reduction in surface $[O_2]$ under film growth conditions. For these conditions, etching reactions by OH and O_2 are likely less important.

Diamond growth in low pressure hydrogen/oxygen flames with post-flame injection of methane is also investigated. Deposition by this method offers the potential of an extremely high level of control over the chemical growth environment. Several experimental conditions for growth of diamond particles were identified. Modeling and

diagnostic studies were also performed for a single injection geometry. The results suggest that mixing of the injectant with the post-flame gases can be well approximated by a simplified flow model with limited chemistry. Further analysis suggests that the technique could be useful commercially if mixing at the substrate could be improved.

Contents

List of Figures

List of Tables

Chapter 1

Introduction

1.1 Background and Motivation

Diamond is a useful engineering material because of its unique combination of properties. Aside from being the hardest material known, diamond also exhibits the highest room temperature thermal conductivity of any material and is an electrical insulator. The high melting temperature, chemical inertness (below $\sim$ 700 °C), and wide transmission range of diamond are other distinctive properties. Thus, in cases where its cost is not prohibitive, diamond is a useful material for applications requiring wear-resistant coatings, extreme hardness, high heat fluxes, and survivability in harsh chemical environments. Figure 1.1 summarizes the key properties of diamond and many of the potential applications.

Wide use of diamond has been limited by the high cost of obtaining natural diamond. Synthetic diamond made by high-temperature high-pressure synthesis can be fabricated inexpensively and in large quantities. However, due to the high pressures involved, such synthesis methods are only capable of producing irregular diamond particles, usually less than 1 carat. Therefore, synthetic diamond, until recently, has been limited to engineering applications in which diamond grit, powder, or small crystals could be used. Diamond thin films and complex shapes are simply not manufacturable by high-temperature high-pressure synthesis.

Synthesis of diamond at low pressures was first demonstrated by Eversole in 1953 [1]. Since then, a wide variety of low pressure synthesis methods have emerged. These methods involve producing diamond at temperatures and pressures in which

Property	Possible Applications
Extreme hardness	Abrasion resistant coatings (cutting tools)
High thermal conductivity Electrical insulator	Heat sinks for electronic devices
Chemically inert	Coatings for prosthetic devices
Low friction coefficient	Bearing coatings
Wide transmission range Low thermal expansion High melting temperature	Window and lens materials Sensors for severe environments
High band gap High hole mobility Low dielectric constant Radiation resistive	High speed electronic devices

Figure 1.1: Properties of diamond and possible applications.

graphite is the thermodynamically stable phase of carbon. In low pressure synthesis, a substrate is placed in a chemical environment in which there is a substantial radical pool containing carbon-bearing species (e.g., CH_3, C_2H, C, etc.) as well as large amounts of atomic hydrogen and, sometimes, smaller quantities of molecular oxygen, atomic oxygen, and/or hydroxl radicals. Under appropriate substrate temperature conditions, carbon-bearing radicals are deposited on the substrate surface. Deposited carbon can bond with surface carbon with an sp^2 bond (as in graphite) or with an sp^3 bond (as in diamond). However, atomic hydrogen can, at common deposition

temperatures (700 -1200 °C) readily etch sp^2 bonded carbon [2]. Meanwhile, sp^3 bonded carbon cannot be readily etched by atomic hydrogen. Indeed, no etch rate for diamond by atomic hydrogen has been observed to date. If sufficient atomic hydrogen is present to suppress the formation of non-diamond carbon, then the carbon deposit will be primarily sp^3 bonded.

Chemical environments condusive to diamond growth have been created in a wide variety of reactors. Four of these are shown schematically in figure 2. In the case of the hot-filament, DC torch, and microwave methods, a mixture of primarily hydrogen and $\sim$ 1% methane is activated by some means. The hydrogen is dissociated, and hydrocarbon radicals are created. The substrate is held at the appropriate temperature by either heating or cooling. Thus, at the growth surface, large quantities of atomic hydrogen and smaller quantities of carbon-bearing radicals are present.

Film growth rates and quality of deposit vary depending on the method and run conditions chosen. All methods are capable of growing high quality diamond, but film growth rates can range from < 1 μm per hour for the hot filament methods to over 100 μm per hour for some DC torch reactors.

Some understanding of the process of diamond growth has been obtained through a series of experimental, theoretical, and computational studies. There is substantial evidence that methyl radicals are the dominant diamond precursor in most diamond CVD reactors [3, 4, 5]. However, the experimental work of Martin and Hill [4], Harris and Martin [5], and Loh and Cappelli [6] strongly suggests that acetylene may also

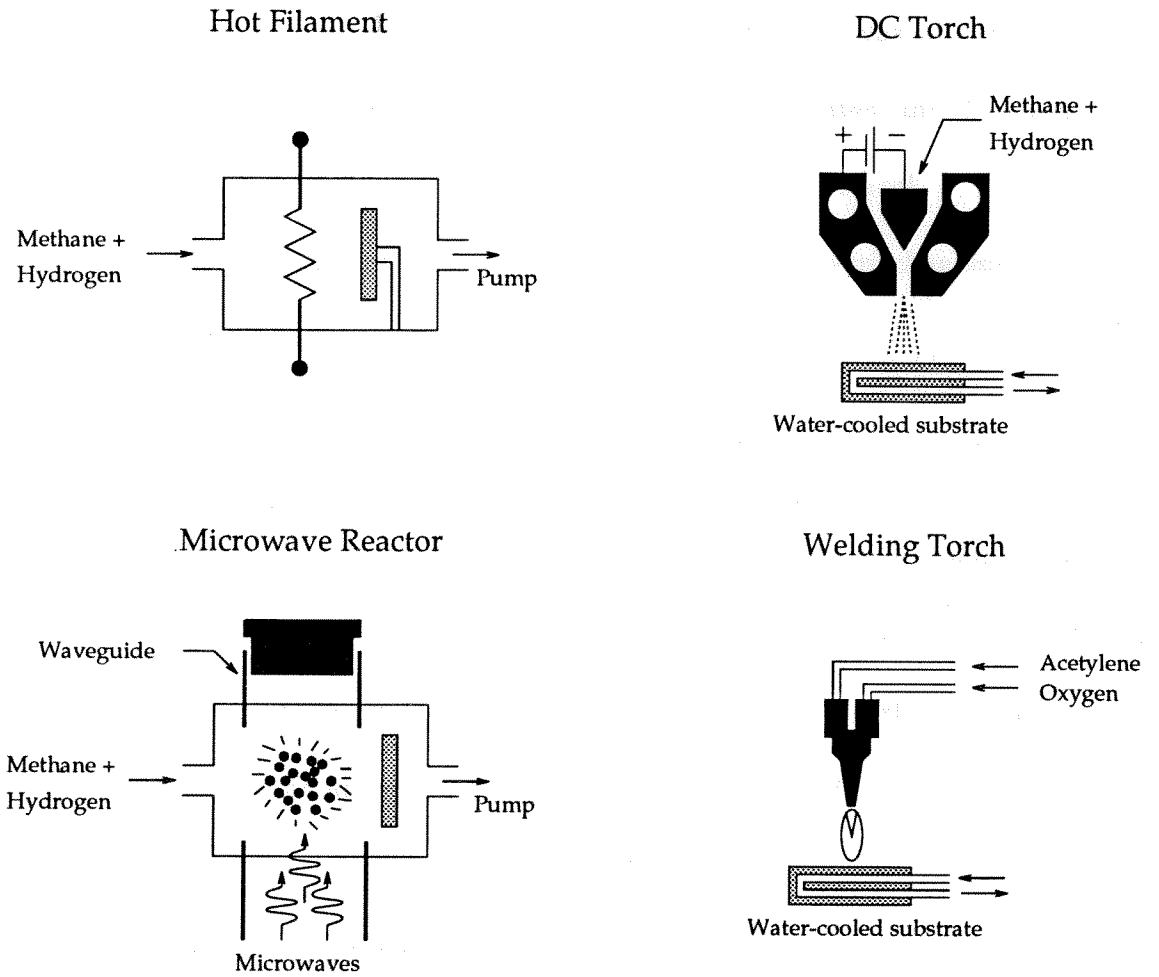

Figure 1.2: Common techniques of diamond chemical vapor deposition.

serve as a diamond precursor, although with lower associated growth rates.

Several potential growth mechanisms have been published [7, 8, 9, 10, 11] which are capable of predicting diamond growth rates given surface mole fractions of species such as H, CH_3, and C_2H_2. Perhaps the most common mechanism used is the Harris mechanism [9]. This mechanism assumes that diamond growth proceeds through the following 3 steps: 1), the hydrogen terminated diamond surface is activated *via*

abstraction of a surface H atom by an H radical from the gas phase; 2), methyl radicals from the gas phase attach to the surface at active sites; and 3), gas phase H removes the additional H atoms from the adsorbed methyl radical.

The growth rate of diamond (G) predicted by the Harris mechanism can be well fit to the following simplified form[12]:

$$G = 1.8 \times 10^{11} \frac{[CH_3][H]}{5 \times 10^{-9} + [H]}. \tag{1.1}$$

Concentrations are in moles/cm^2, and the growth rate is given in microns per hour. For the case where $[H] \ll 5 \times 10^{-9}$, the growth rate is simply proportional to $[CH_3][H]$. Equation 1 generally predicts the diamond growth rate in any of the common reactors (for a substrate temperature of 1200 K) to within a factor of 2[12].

1.2 Flame Synthesis

Diamond film growth in a flame was first demonstrated by Hirose and Mitsuizumi [13]. In these experiments a conventional welding torch was used. A fuel-rich mixture of oxygen and acetylene (approximately a 1:1 ratio of flow rates) was burned over a substrate cooled to around 1000 °C. Deposits over small areas (< 3 mm diameter) at film growth rates of 100-200 μm per hour were observed.

Though the flames contain many other species in addition to those required for diamond growth, the same essential conditions as in other reactors prevail. Acetylene/oxygen flames produce large quantities of atomic hydrogen and hydrocarbon

radicals. The oxygen in the rich flame appears at the surface primarily in the species CO, CO_2, and H_2O, all of which negligibly influence the carbon deposition process. Thus, under optimal conditions, flames provide all of the essentials for a diamond growth environment.

Indeed, several research groups have demonstrated high quality diamond deposition in atmospheric pressure acetylene/oxygen flames [14, 15, 16, 17]. Snail *et al.* have demonstrated growth in a torch using ethylene/oxygen and ethane/oxygen mixtures as well [18].

Because of its simplicity, the atmospheric pressure torch method has been the subject of many studies on diamond growth. Growth rates and diamond quality have been mapped out as a function of oxygen to acetylene ratio (R) and substrate temperature (T_S) [19]. For a given T_S, a small range of R values ($\sim$ 0.8 - 1.05) was observed to grow diamond. For R values below that range, only non-diamond carbon was observed. Above the maximum R value for diamond growth, the flame became too oxidizing for carbon deposition. In these cases, sufficient oxygen was present at the surface to etch both diamond and non-diamond faster than the diamond deposition rate. The result is no deposited carbon. Diamond growth on non-diamond substrates was observed for T_S from 700 -1200 °C. For a fixed value of R the diamond growth rate was found to increase with temperature; however, the sp^2 carbon content was also found to increase with T_S. Other studies have investigated numerous topics including homoepitaxial growth on diamond substrates [20] and reduction in system

pressures (to 300 Torr) [21].

Several diagnostics have been applied to atmospheric torches to investigate the gas-phase chemistry responsible for producing the diamond growth environment. Matsui *et al.* used optical emission spectroscopy to analyze their torch flames [22]. Several features common to most hydrocarbon flame spectra (i.e., OH, CH, and C_2 Swan band emission) were observed, but emission from H was not detected. Spatial profiles of electronically excited OH, CH, and C_2 were reported as were emission intensity vs. R profiles.

Fourier Transform Infrared (FTIR) spectroscopy was later used to measure gas phase temperature and species concentrations of CO, CO_2, H_2O, and OH in an oxy-acetylene torch under diamond growth conditions [23]. The observed flame temperatures in the freestream above the deposition surface were equal to or greater than the calculated adiabatic flame temperature ($\sim$ 3300 K). Flame temperatures in excess of the adiabatic flame temperature in oxygen/acetylene flames have been predicted by Meeks *et al.* in flame simulations[24]. The predicted temperature overshoot is attributed to an underdissociation of C_2H_2 in the gas phase, leading to a higher sensible enthalpy and, therefore, a higher temperature. At such high gas phase temperatures under atmospheric conditions, much dissociation has occurred, and thus the radical pool is likely very large.

Matsui *et al.* applied laser-induced fluorescence (LIF) and mass spectrometry to characterize their torch flames [15]. The LIF measurements were used to probe the

flame structure. The mass spectrometry measurements found that the main gaseous concentrations in the feather region of the flame were consistent with the equilibrium concentrations at the adiabatic flame temperature.

Further fluorescence studies were performed in an atmospheric torch by Cappelli and Paul [17]. Near-surface LIF measurements were performed to map the surface distribution of C_2H. The results were compared with the spatially non-uniform deposit. Diamond growth was observed in the regions of highest C_2H concentrations. The study revealed that the chemical environment produced by the flame at the growth surface was also highly non-uniform and that deposit non-uniformities could be correlated with gas phase non-uniformities.

Several computational studies used some of the experimental results to set up models to predict the chemical environment at the growth surface in an acetylene/oxygen torch. Goodwin made use of the idea that the gas in the flame freestream above the substrate is in chemical equilibrium to model the growth environment [25]. It was suggested that, with the equilibrium assumption and knowledge of the adiabatic flame temperature, the substrate temperature, appropriate gas phase transport properties, and estimates of surface reaction rates, a computational model could yield a good prediction of the chemical environment at the surface. Results of the calculations suggest that near-surface gases contain nearly 12% atomic hydrogen, 3% acetylene, .06% atomic carbon, and .005% methyl radicals. Mole fractions of O_2, O, and OH are below 10^{-6}. This work presents the first indications of the composition of a flame

diamond growth environment.

While great success in diamond quality and high growth rate have been obtained, application of the torch method to industrial processes has been limited by the size of the deposit. Most atmospheric torches produce a diamond deposit < 5 mm in diameter surrounded by a non-diamond carbon region. Multiple nozzle methods, some involving rotating substrates, have met with only limited success in obtaining large-area deposits. The exception is perhaps Ravi, Koch, and Olson who have deposited large area diamond with an atmospheric combustion method but reveal few details of the process (including growth rate and flow rates) in their publication [26].

1.3 Flat Flames

Deposit area has been increased into the 1-2 cm diameter range by Murayama and Uchida [27]. High flow rates and hydrogen addition were used to stablize an atmospheric acetylene/oxygen/hydrogen flame on the substrate surface above the injection nozzle. The stabilized flame is flat and parallel to the substrate over a radius of up to 1 cm. Growth rates of 40 μm per hour have been reported. McCarty *et al.* used a similar technique to grow larger area diamond films while minimizing the fraction of unburned acetylene in the flame [28]. While these techniques represent an improvement over the standard welding torch approach, scalability up to larger substrates does not appear to be elementary, the gas flow rates are extremely high, and the explosion hazards are significant. Thus, while atmospheric pressure combustion synthesis

offers simplicity, high growth rates, and good film quality, the industrial applicability of torch and torch-related methods may be limited.

Conventional low pressure flat flame burners, on the other hand, provide axisymmetric flames with uniform chemistry over radii roughly equal to the burner radius, which can be arbitrarily large. Typical burner radii are < 5 cm. Extensive studies of flames have been performed using low pressure flat flame burners due to the one-dimensionality of the flow and the expanded flame zones observed at low pressures. Since these flames offer a wide zone of uniform chemistry, combustion synthesis using flat flame burners could perhaps provide both the benefits of conventional combustion synthesis and large area deposition.

Cooper and Yarborough first demonstrated diamond growth by acetylene/oxygen combustion in low pressure (50 Torr) flat flames [29]. Isolated particles of diamond were obtained under various conditions. Carbon deposits were verified as diamond by observation of the peak at a shift of 1332 cm^{-1} in the Raman spectrum of the deposit. Substantial non-diamond carbon was observed both in the Raman spectrum and in the SEM photographs of the deposit.

The study identified several conditions in which diamond was deposited on silicon substrates. Most notable in the results was that the R values necessary to deposit diamond ranged from 1.2 – 1.3, substantially higher than those used in atmospheric methods. Growth rates were also much lower. Particle radii grew at rates < 1 μm per hour.

While the study proved definitively that diamond could be grown in low pressure oxyacetylene flat flames, several key issues remained to be addressed. First, the reported run conditions yielded isolated diamond particles but not continuous films. Since films are necessary for most industrial applications of CVD diamond, low pressure flames can only be considered as a practical alternative to other diamond CVD methods if film growth conditions can be achieved. The results of the study did not establish whether or not films were possible in low pressure acetylene/oxygen flames.

Second, the experimental matrix was performed over only a small region of the potential parameter space. Each experimental growth run is characterized by at least six experimental parameters; R, T_S, system pressure, total specific flow rate, burner to substrate distance (D_S), and burner surface temperature (T_B). In addition, substrate material and preparation are key variables. Results from fewer than 10 run conditions were reported. However, since growth conditions were achieved, the study formed an excellent starting point for further investigation of the large parameter space in search of film growth conditions, increases in growth rate, and improvements in diamond quality.

Lastly, the results were analyzed using the diagnostic results of Westmorland on *similar* acetylene/oxygen flames. This analysis pointed out that maximum temperatures in these low pressure flames might be as much as 1000 °C less than those observed in atmospheric pressure torches. Also, the H and CH_3 profiles were observed to decay quickly after reaching maxima close to the burner surface. This result sug-

gested that operating at short burner to substrate distances (D_S) might result in the best diamond. Though these results lent considerable insight into the flame environment, it is clear that application of diagnostics to the actual growth environment and modeling using detailed chemical kinetics would provide more information on the true nature of the growth environment in these flames.

1.4 The Present Study

Since deposition of diamond in low pressure flames was shown to be possible, and since the scope of the investigation was limited, further work in this area is warranted. The purpose of the experimental work described in this report is to investigate the potential of flat flames for large area deposition of diamond films. Since flat flames provide an excellent medium for modeling and diagnostics, analysis of flames which grow diamond might also lead to a better understanding of the fundamental processes of diamond growth.

The limited amount of data on the regions of parameter space condusive to diamond growth suggests that the first step is to perform a large matrix of growth experiments with some systematic variation of parameters. To assure repeatability, careful control over the experimental parameters has been built into the setup. The substrate temperatures are uniform over large areas, and each of the experimental parameters is measured accurately. A secondary goal of the matrix is then to identify conditions which grow high quality diamond films. Also, trends in diamond quality

and growth rate with changes in the experimental parameters are identified.

The results are analyzed by modeling and diagnostics. The model used contains large gas-phase and surface chemical mechanisms. The model predicts the chemical environment at the substrate surface, and results from the experimental matrix are interpreted in light of the predicted environment. Diagnostics are used to verify that the model correctly predicts at least some key elements of the flame structure.

The end result of this study is an assessment of low pressure flat flames as a diamond film growth method. The study also identifies the key issues in low pressure diamond film growth.

1.5 Outline of this Report

Chapter 2 of this report gives the general experimental details of the setup used in the study. Specific details of experiments performed are given in the appropriate chapters. Additional details of the design and construction of the burners and substrate holders are given in Appendix B and Appendix C.

The modeling approach is explained in Chapter 3, including the details of the assumptions made in the model and the specific chemical databases used. To verify that the model correctly predicts the chemical environment in the flames, several diagnostic measurements are performed on a series of flames, and the predictions of the model are compared with the experimental results.

The initial series of experiments with acetylene/oxygen flames is described and

analyzed in Chapter 4. An extensive matrix of run conditions is presented, and the results are analyzed in terms of the chemical environments predicted by the model. The conditions presented in this chapter yield only isolated diamond particles.

Analysis of the results from Chapter 4 led to the choice of a new operating regime. In this new regime, several film growth conditions were isolated. The results from these growth experiments are presented in Chapter 5. Analysis of the film growth conditions is also performed with the help of the flame model.

Chapter 6 presents the results of a series of experiments designed to exploit the ability of low pressure hydrogen/oxygen flames to produce copious amounts of atomic hydrogen. A short study of post-flame injection at the substrate of methane/hydrogen mixtures into hydrogen/oxygen flames is presented. Results from growth experiments, one- and two-dimensional modeling, and diagnostic investigations into the growth environment are all analyzed. The industrial potential for this particular growth method is evaluated.

Chapter 2

Experimental Setup

A general schematic of the experimental setup is shown in Figure 2.1. The facility, hereafter referred to as the Low Pressure Combustion Facility (LPCF), was designed for research into combustion environments at sub-atmospheric pressures.

The vacuum chamber is a water-cooled stainless steel bell jar (45 cm diameter, 75 cm height) which rests on top of a feedthrough collar. Vacuum in the system is maintained by a Stokes mechanical sliding vane vacuum pump with a rated pumping speed of 50 cubic feet per minute. Optical access to the system is provided by three fused silica 5 cm diameter windows. The fused silica windows transmit radiation in the visible and ultraviolet down to 200 nm. A larger (15 cm diameter) Pyrex window provides optical access to the front of the chamber. For fluorescence measurements which require detection of radiation at 310 nm, this window can be replaced with a fourth 5 cm fused silica window.

Vacuum feedthroughs to the system include six 0.25 inch OD liquid feedthroughs, a four conductor high current (100 A) feedthrough, a 20 pin electrical feedthrough, a 0.25 inch vent valve, and a 1 inch travel linear feedthrough for the ignitor.

Gases for the system are provided from compressed gas cylinders. Outlet pressures are maintained at 5-50 psi by pressure regulators on the cylinders. Flows to the system are controlled by electronic thermal mass flow controllers (MKS 1258C). Each feed gas is regulated by a separate mass flow controller. A central controller/programmer unit provides the control feedback signals for each flow controller. Set points for each of the feed gas flows can be set manually on the controller/programmer unit

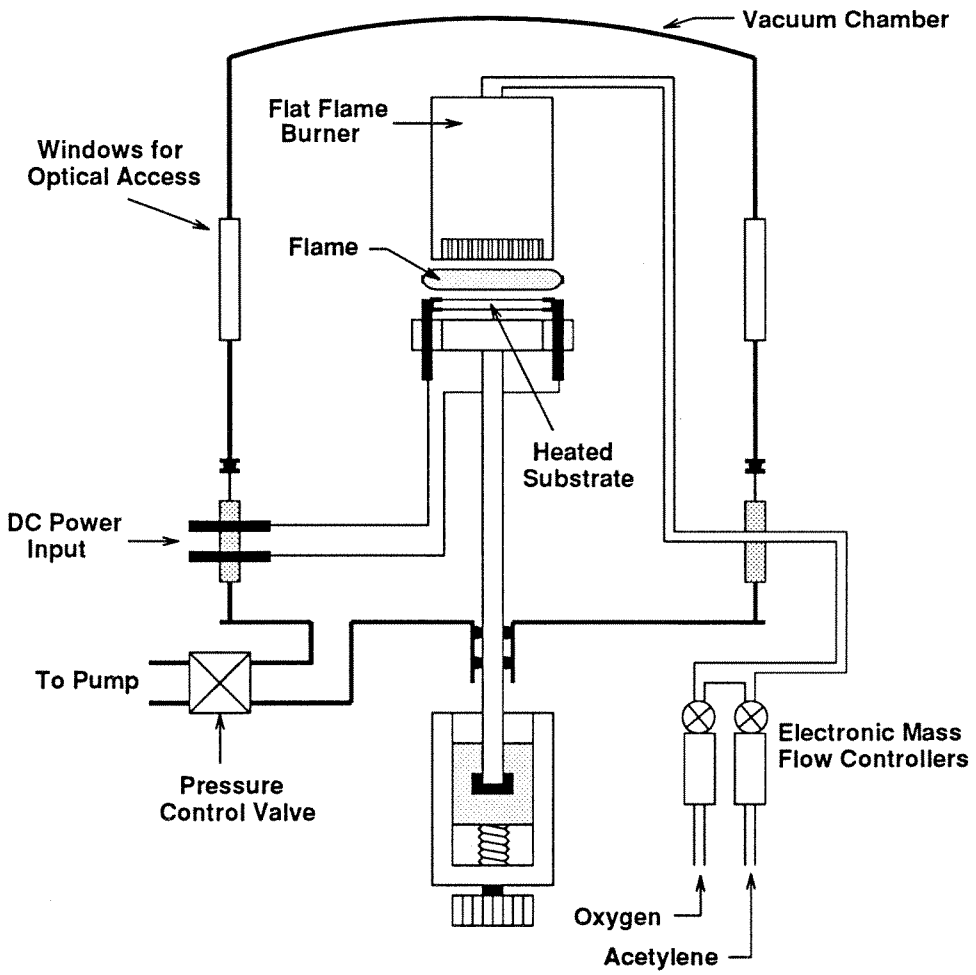

Figure 2.1: The Low Pressure Combustion Facility.

or programmed externally using a personal computer. Use of the computer for flow control allows for precise repeatability of startup, run, and shutdown conditions. The flow controllers are factory calibrated and accurate to 0.5% of full scale (10 standard liters per minute). Gases are mixed by a simple tee connection before passing through a flashback arrestor and entering the chamber through a liquid feedthrough line.

Premixed gases are fed to a flat flame burner for combustion. The burner is a custom design based loosely on that of Bittner [30]. The burner face consists of a

copper plate with an array of 1 mm diameter holes. The high thermal conductivity of the 13 mm thick copper plate, combined with the high thermal resistance of the thin walls, insures a relatively uniform burner surface temperature profile across the burner face. The details of the burner design and construction are given in Appendix B.

The burner is ignited by placing a resistively heated nichrome wire (at $\sim$ 1200 °C) a few mm from the burner surface as the flows are turned on. Ignition requires slightly leaner conditions than those used for runs. The flow rates are ramped by computer to run conditions within 1 minute after ignition.

Below the burner and parallel to the burner face is the substrate holder. Several different holder designs were used. The function of the holder was to maintain the position of the substrate with respect to the burner and to provide necessary heating or cooling to achieve the desired substrate temperature. Details of the individual substrate holder designs are given in Appendix C.

Both the burner and substrate were mounted on external translation stages to allow for positional control. The burner/substrate assembly was mounted on a primary translation stage which controlled vertical position of the entire assembly. This was used to translate the assembly within the vacuum chamber with respect to a fixed laser beam for optical profiles. A second translation stage, mounted atop the first, controlled the position of the substrate relative to the burner face. This degree of freedom allowed the burner to substrate distance (D_S) to be varied independently

of burner position during the course of a run. Both translation stages were motorized and could be controlled externally using a controller/driver unit and a personal computer. The translation stages were mounted outside the chamber, and the linear motion was fed through to the assembly by an o-ring sealed linear motion feedthrough of custom design with two concentric sliders.

For measurements of stable species concentrations at the substrate surface, a residual gas analyzer (Inficon Quadrex 200) was used. A schematic of the gas sampling setup is shown in Figure 2.2. In diagnostic runs, substrates with 1 mm holes were employed, and a sampling probe was placed immediately below the hole. The sampling probe consisted of an $\sim$ 0.5 m length of 1 cm internal diameter quartz tubing drawn at one end to create an orifice of 200 – 400 microns in diameter. A vacuum pump maintains the pressure in the probe at 0.5 Torr. A rapid pressure drop to 0.5 Torr across the probe orifice has been shown previously to quench gas phase chemistry, except for radical recombination [31]. The quartz surface of the probe is also non-reactive. Only radical recombination occurs at the walls. Sampled gases then pass through a length of stainless steel bellows, and portions of the gas enter the quadropole mass spectrometer by passing through an orifice valve. These gases are analyzed for the atomic mass distribution by the mass spectrometer. Mass peaks from 1 to 200 atomic mass units are displayed by the controller unit. A turbopump and mechanical backing pump clear the sampled gases from the mass spectrometer. The residence time in the system for gases sampled by the probe is less than 1 second. To

obtain information about the presence of specific molecules in the system, the mass peak corresponding to the species of interest is monitored. To obtain absolute mole fraction data, relative ionization cross sections with respect to argon of each species of interest are determined. This is accomplished by filling the chamber with a calibration mixture of the species of interest in argon. The ratio of mass peak amplitude of the species of interest to the mass peak amplitude of argon, divided by the ratio of mole fractions of the two species, yields the relative ionization cross section. Then, since argon is non-reactive in the gas phase, it is assumed that its mole fraction can be accurately calculated at the substrate surface. With the knowledge of the argon mole fraction, the argon mass peak amplitude, the cross section ratio, and the mass peak amplitude of the species of interest, the absolute mole fraction of the species of interest can be calculated.

Since substrate temperature (T_S) and burner temperature (T_B) are two key experimental temperature parameters, they must both be measured and experimentally controlled. To monitor burner surface temperatures and some substrate temperatures, type K thermocouples are used. For burner temperatures, a type K thermocouple junction is placed in a hole in the burner face near the center of the array. The thermocouple voltage is ice-point corrected by a controller inside the vacuum chamber, and the voltage across the junction is read by a digital voltmeter. For molybdenum plate substrates, thermocouple wires were individually inserted into two 0.5 mm holes spaced 2 mm apart in the surface of the substrate. The temperature given by the

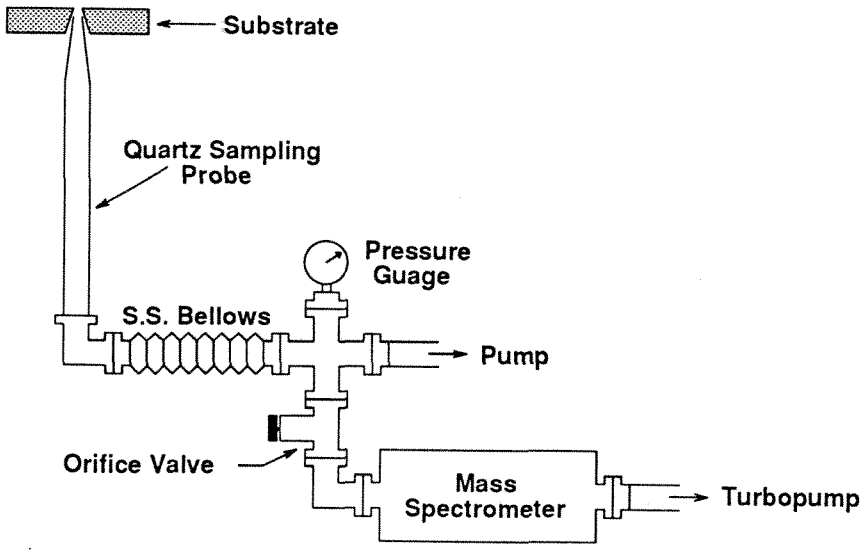

Figure 2.2: Schematic of the gas sampling setup for analysis using the residual gas analyzer.

thermocouple voltage in this case is the average temperature in the region between the holes.

For silicon substrates and as an additional temperature diagnostic for molybdenum substrates, infrared pyrometers were used to estimate surface temperatures. Two different pyrometers were employed in the study, a one-color Leeds and Northrup (Model 8622-C) pyrometer and a two-color Ircon (Modline Plus) pyrometer. The one-color pyrometer measures the brightness temperature at 0.665 μm of an object in the range of 750 – 2500 °C relative to an internal calibrated filament. The resolution of the one-color measurement was 5 K. The measurements require correction for the emissivity of the sample and transmission losses through system windows.

The two-color pyrometer measures relative intensities of two emission bands, the

first extending from 0.7 to 1.08 μm and the second covering a small range of wavelengths centered at 1.08 μm. An assumed emissivity slope setting is required to compute a temperature. The two-color pyrometer operates over a range of 700 – 1400 °C and has a measurement resolution of 5 K. Due to the geometry of the setup, it was necessary to operate the pyrometer at a grazing angle ($\sim$ 10° – 20°) with respect to the substrate. Such a measurement angle subjects the instrument to temperature errors resulting from radiation reflected by the surface. Indeed, a variation in temperature reading of up to 15 K was observed as the measurement angle was varied. Comparison of molybdenum substrate temperatures measured by thermocouple, which are assumed to be accurate to better than 5 K, yielded agreement always to within 35 K for both one and two-color pyrometers. Thus, we infer that our substrate temperature uncertainty for pyrometer measurements was 35 K.

Deposits obtained in the facility are analyzed using optical microscopy for particle size distributions and nucleation density, scanning electron microscopy for high resolution images, and micro- and macro-Raman spectroscopy for characterization of film quality.

Chapter 3

Modeling and Diagnostics

In order to analyze the experimental results of growth runs in terms of the chemical environment near the substrate surface, a reacting flow model is used. Experimental diagnostics are used to test the predictions of the model, thereby assessing its validity.

3.1 The Model

The deposition environment to model is represented schematically in Figure 3.1. The burner resides parallel to and above the substrate. Both the burner and the substrate have surface temperatures which are approximately constant over their respective areas. The premixed gases flow downward through the burner face and react in the gap. The flow has a stagnation point on the surface of the substrate on the system axis.

Both gas phase and surface chemistry are occurring in the system. The premixed gases are reacting to form combustion products, and radicals are recombining and, in some cases, depositing on the burner and substrate surfaces. Because of the low operating pressures (20–60 Torr), the reaction zone of the flat flames is expanded. Such a system cannot be well approximated by a one or two step combustion model with a simple flame front. Gas phase chemistry must be calculated continuously throughout the flowfield in order to accurately predict the chemical environment in the system.

Surface chemistry is also non-negligible. Radical recombination at surfaces is rapid and can affect the spatial concentration profile of the gas phase species throughout

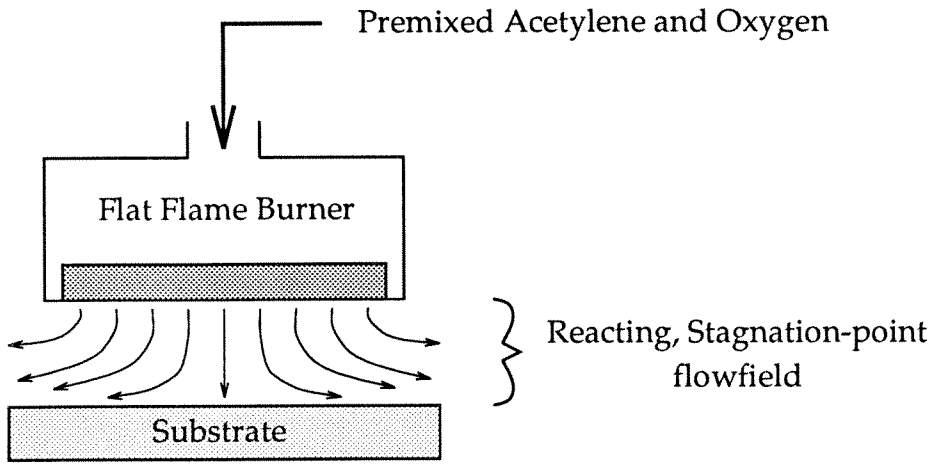

Figure 3.1: The general problem to model.

the flowfield. Also, in deposition environments, two other types of surface reactions are occurring: deposition of certain species on the surface and removal of certain surface species back to the gas phase. The substrate serves as a sink for the reactants in these surface reactions and a source for the reaction products. Some estimation of the surface processes occurring during deposition must be incorporated.

Typical Reynolds numbers for our flames, based on the burner to substrate distance (D_S), are less than 5. Thus, viscosity plays a key role in the structure of the flowfield. Diffusion velocities are also of the same order as flow velocities at many locations in the flame. Finally, there is large heat release and sharp thermal gradients in the flow. Consequently, all transport properties are important and must be calculated at each point in the flowfield.

The model used was created by Goodwin [32] and will be described briefly here. A similarity solution, first proposed by von Kármán [33], to the conservation equa-

tions forms the basis for the fluid mechanics of the model. The solution assumes an infinite burner and substrate radius, a purely axial inlet flow, and constant temperature burner and substrate surfaces. In addition, the Mach number at any point in the flowfield is assumed to be much less than 1 (i.e., incompressible flow). In this case, the continuity, species continuity, momentum, and energy equations reduce to a coupled set of one-dimensional differential equations in the axial coordinate x. Only the radial velocity and the pressure gradient retain radial dependence while species concentrations, temperature, and axial velocity are all independent of the radial coordinate r.

Clearly, the similarity solution will not hold for the entire flowfield, but two-dimensional simulations in silicon deposition reactors [34] suggest that the solution is quite accurate for up to 90% of the burner diameter. The uniformity of deposit quality and thickness over diameters equal to the burner area, as observed in our experiments (see Chapter 5), suggest that this is also the case in our reactor.

To obtain the velocity, temperature, and composition at each axial point in the flowfield, the variables $U(x)$ and $G(x)$ are first introduced. They are defined as follows:

$$U(x) = \frac{1}{2} \times \text{axial mass flux} = \frac{1}{2}\rho u \tag{3.1}$$

$$G(x) \equiv \frac{dU}{dx} \tag{3.2}$$

In equation 3.1 ρ is the local gas phase density, and u is the axial velocity. The following boundary value problem, which consists of continuity, momentum, energy, and species continuity equations, is then solved for $U(x)$,$G(x)$,$T(x)$, and $Y_i(x)$ for $i = 1, 2, ...n$, where Y_i is the mass fraction of species i in a system of n species [35].

$$\text{(continuity)} \quad \frac{dU}{dx} = G \tag{3.3}$$

$$\text{(momentum)} \quad \frac{d}{dx}\left[\mu\frac{d}{dx}\left(\frac{G}{\rho}\right)\right] - 2\frac{d}{dx}\left(\frac{UG}{\rho}\right) + \frac{3}{\rho}G^2 + H = 0 \tag{3.4}$$

$$\text{(energy)} \quad 2U\frac{dT}{dx} - \frac{1}{c_p}\frac{d}{dx}\lambda\frac{dT}{dx} + \frac{\rho}{c_p}\sum_{k=1}^{K} Y_k c_{pk} V_k \frac{dT}{dx} + \frac{1}{c_p}\sum_{k=1}^{K} h_k \dot{\omega}_k = 0 \tag{3.5}$$

$$\text{(species)} \quad 2U\frac{dY_k}{dx} + \frac{d}{dx}(\rho Y_k V_k) - W_k \dot{\omega}_k = 0 \tag{3.6}$$

The terms appearing in these equations are defined as follows: $H \equiv (1/r)(\partial P/\partial r)$, the radial pressure gradient eigenvalue; λ, the thermal conductivity; μ, the viscosity; V_k, the diffusion velocity of species k; c_p, the mixture specific heat; ρ, the density; T, the temperature; W_k, the molar mass of species k; h_k, the specific enthalpy of species k; $\dot{\omega}_k$, the molar chemical production rate of species k; Y_k, the mass fraction of species k. All the mentioned variables are functions of x alone, except for H which can be shown to be a constant of the flowfield [35].

The diffusion velocities for each species are calculated using mixture averaged diffusion coefficients. For each species i, the diffusion velocity is given by:

$$V_i = -D_i\frac{1}{X_i}\frac{\partial X_i}{\partial x} - \frac{D_i^T}{\rho Y_k}\frac{1}{T}\frac{\partial T}{\partial x} \tag{3.7}$$

For a particular species i, D_i^T is the thermal diffusion coefficient, D_i is the mixture averaged diffusion coefficient, and X_i is the mole fraction. The mixture averaged diffusion coefficients are calculated from the binary diffusion coefficients D_{ij} according to the relation:

$$D_i = \frac{1 - Y_i}{\sum_{j \neq i}^{n} X_j / D_{ji}} \tag{3.8}$$

The computational method must solve $F(\phi) = 0$, where F corresponds to the left hand side of equations 3.3-3.6, and

$$\phi = (U(x), G(x), T(x), Y_1(x), ..., Y_k(x)). \tag{3.9}$$

At the burner surface ($x = x_B$), a temperature T_B, an inlet gas composition (Y_i for $i = 1, 2, ...n$), and an inlet gas velocity u_B must all be specified. These specifications set the boundary conditions at the burner substrate to the following:

$$U = \frac{1}{2}\rho_B u_B, \;\; G = 0, \;\; T = T_B, \;\; Y_k = Y_{kB} \tag{3.10}$$

Similarly, at the substrate surface ($x = x_S$) there is again a fixed temperature (T_S). Since there is deposition occurring at the substrate surface, the mass flux to the surface will not be zero (i.e., $U_S \neq 0$). Instead, the mass flux at the surface will be equal to the sum over the molar production rates for each species ($\dot{s}_j$) multiplied by the molecular weight for each species (M_j). Thus, the boundary conditions at the substrate are:

$$U = -\frac{1}{2}\sum_j \dot{s}_j M_n, \;\; T = T_S \tag{3.11}$$

Species production rates are determined through incorporation of gas phase and surface chemical mechanisms. Transport properties are calculated using formulae from kinetic theory [36].

The computational method makes second-order, finite difference approximations to reduce the problem to a system of algebraic equations. The system of algebraic equations is solved using a combination of Newton's method and time integration.

The gas phase chemical mechanism is that of Miller and Melius [37]. The mechanism contains 50 species and 210 reactions. The mechanism is designed to modify the Miller/Bowman mechanism [38] to more accurately model near-sooting conditions in hydrocarbon flames. The gas phase chemical mechanism is given in Appendix E.

The Miller/Bowman mechanism and its variants have been tested extensively in hydrocarbon flat flames. Numerous diagnostic measurements in hydrogen/oxygen and methane/oxygen (e.g., [39, 40]) flames have established that the mechanism models C_1 oxidation kinetics and hydrogen/oxygen chemistry well enough to predict major stable species concentrations and several key radical concentrations to within experimental uncertainties. However, in nearly all cases, the temperature profile produced by the model significantly overpredicts the post-flame temperature, sometimes by as much as several hundred degrees. Therefore, the model calculations often use the experimentally determined temperature profile as an input to the model. The energy equation is not solved in these cases. Possible sources of error which might lead to the inaccurate temperature predictions include additional heat losses at the burner

surface, flame radiation, and radial heat transfer to the surrounding gas.

Other studies have investigated the ability of the mechanism to model C_2 oxidation kinetics. Bernstein *et al.* [40] used REMPI and LIF to characterize unstrained, burner-stabilized, near stoichiometric ethylene/oxygen flat flames. The temperature profile was experimentally determined using radiation-corrected thermocouples. Though the model did not predict radical concentrations of O, CH, CH_3, and OH to within experimental uncertainty, predicted concentrations were accurate to within a factor of 2. Additionally, the predicted spatial concentration profiles showed good qualitative agreement with experiment.

Miller *et al.* performed a series of experiments on similar unstrained acetylene/oxygen/argon flames at equivalence ratios of 1.0, 1.67, and 2.0 [41]. The temperature profiles were experimentally determined using LIF of OH, and LIF was also used to obtain spatial OH, CH, and H concentration profiles. Spatial profiles of stable species were obtained using mass spectrometry. For the $\Phi = 1.0$ and 1.67 cases, the predicted stable species concentrations were accurate to within the experimental uncertainty of the measurements. In all three cases, the predicted radical concentrations were again usually within a factor of 2 or 3 of the experiments, and there was fair qualitative agreement among predicted and observed concentration spatial profiles.

Thus, while the hydrocarbon combustion mechanism cannot be considered definitive, experiments suggest that it is capable of predicting important aspects of acetylene/oxygen and methane/oxygen flame structure. In most cases, major species con-

centrations can be predicted to within 25–50% and key radical species to within a factor of 2 in unstrained, burner-stablized low pressure flames. However, the model predictions of the gas phase temperature profile appear to be too high in general, especially in the post-flame gases. Therefore, in order to obtain the highest accuracy in the species concentration profiles, an experimentally measured temperature profile must be used as an input to the model.

To account for surface chemistry, the surface is sectioned into sites. Each molecule which strikes the surface from the gas phase hits a site on the surface. To select a site density for a diamond surface, it is noted that the diamond surface in a hydrogen atmosphere is hydrogen terminated with a density of surface hydrogen of 3×10^{-9} moles/cm^2. Therefore, this is chosen as the overall site density. Several different types of sites are assumed to exist. A hydrogen atom bonded to a surface carbon forms a C_dH site. If that hydrogen is removed, leaving a surface carbon atom with an unpaired valence electron, an active site (C_d*) is formed.

In the Harris mechanism for diamond growth, a methyl radical attaches to an active site, forming a third type of site labeled C_dM. In a simplified treatment suggested by Goodwin [12], hydrogen from the gas phase abstracts a hydrogen from the C_dM site forming a C_dM* site, and a second abstraction from the C_dM* site converts it to a C_dH site. In the process, a single carbon atom is incorporated into the diamond lattice.

A detailed description of the relevant reactions and associated rates of the reduced

form of the Harris diamond growth mechanism is given by Goodwin[12]. The mechanism predicts a linear growth rate for diamond based upon the surface concentrations of H and CH_3. Certain reaction rates are chosen such that the linear growth rate matches the experimentally observed growth rates in reactors operating with T_S = 1200 K. Since many of the runs cataloged in this report have substrate temperatures less than 1200 K, the growth rate will be overpredicted by the surface mechanism in these cases.

The reaction rates in the surface mechanism are also specified such that the experimentally measured hydrogen recombination probability at 1200 K [42] and its dependence on temperature [43] are accurately reproduced. O and OH recombination at the surface are also included. It is assumed that heterogeneous O and OH recombination occur predominantly by H abstraction at the substrate through the following reactions:

$$O + C_dH \rightarrow OH + C_d* \tag{3.12}$$

$$OH + C_dH \rightarrow H_2O + C_d* \tag{3.13}$$

The reaction rates for the abstraction reactions are chosen to match experimental data for the reactions:

$$O + i\text{-}C_4H_{10} \rightarrow OH + i\text{-}C_4H_9 \tag{3.14}$$

$$OH + i\text{-}C_4H_{10} \rightarrow H_2O + i\text{-}C_4H_9. \quad (3.15)$$

Reactions 3.14 and 3.15 are chosen since they resemble closely the anticipated reaction dynamics for abstraction of an H atom from a hydrogen terminated diamond surface.

Also included in the mechanism is a simplified diamond etching mechanism for O_2 based on the data of Sun and Alam [44] for oxidation of CVD diamond films. The experimental data suggest a reaction order of 0.6 and an activation energy of 54.7 kcal/mole. The rate data were obtained for temperatures up to 1073 K. Thus, data used in our mechanism are extrapolated to higher temperatures. The uncertainty in this rate is at least a factor of two.

Etching of diamond by OH and O is also considered, though no experimental rate data exist on the appropriate etch rates. For each case investigated by the model, two separate runs are performed. In the first run, only etching by O_2 is considered. This run then projects the diamond etch rate if O and OH did not appreciably etch diamond. In the second run, the following two reactions are added to the surface mechanism:

$$O + C_d* \rightarrow CO + C_d* \quad (3.16)$$

$$OH + C_d* \rightarrow CO + C_dH. \quad (3.17)$$

The sticking probabilities for these two etching reactions are set to 1.0. Then each O or OH radical which hits an active surface site removes a carbon atom to the gas

phase in the form of CO. This approach is a reasonable estimate of the maximum possible etch rate by O and OH. The range of etch rates predicted by the model for the two cases can then be assumed to contain the true etch rate. A complete listing of all the reactions and associated rates in the surface chemistry mechanism is given in Appendix D.

The inputs to the model are the six experimental parameters: oxygen to acetylene ratio in the premixed gases (R), total inlet mass flow rate, burner to substrate distance (D_S), system pressure (P), burner surface temperature (T_B), and substrate surface temperature (T_S). Upon convergence, the model returns $\phi(x)$, which contains all the relevant chemical and thermodynamic information in the flowfield.

3.2 Diagnostics

The accuracy of the predictions of the model described in the previous section is uncertain. Several similar one-dimensional stagnation-point reacting flow codes [24, 45, 46, 32, 35, 47] are presently being used to model strained flames. However, there are few experimental measurements to test the model predictions.

Smooke *et al.* [47] have obtained spatial temperature and stable species profiles in counterflowing, premixed, methane/air flames. The model used to predict the temperature and species concentrations was similar to the one used in this study. The gas phase chemical mechanism was basically a subset of the Miller/Bowman mechanism, and was chosen specifically for methane combustion studies. The biggest

difference between the model used in this study and that of Smooke *et al.* is in the choice of boundary conditions at the plane perpendicular to the axis of symmetry at the stagnation point. In the counterflowing flames, temperature and concentration gradients are set to zero at the symmetry plane. Using this model, good agreement between model predictions and experiment was found for species spatial concentration profiles. However, the temperature measurements showed significant deviation from the model's predictions, possibly due to the thermocouple acting as a flameholder. For the case of stagnation-point flames impinging on a constant temperature substrate, there are, to our knowledge, no experimental data to compare with model predictions.

Considering the previously mentioned successes in flame modeling of unstrained, burner-stabilized flat flames using similar combustion mechanisms, there is reason to believe that the stagnation-point model may also be fairly accurate. However, several new features (e.g., surface chemistry) are present in the stagnation-point flow problem which do not occur in the simpler, unstrained case. Also, the extent to which the temperature profile in low pressure stagnation-point flames varies from prediction has yet to be evaluated. Considering the observed temperature overprediction in unstrained flames, it is possible that the predicted temperatures in strained, stagnation-point flames may also be too high.

In this section, we present measurements of temperature and species concentrations in a stagnation-point flame, and compare the results to model predictions. The measurements reported here are for acetylene/oxygen flames similar to those used to

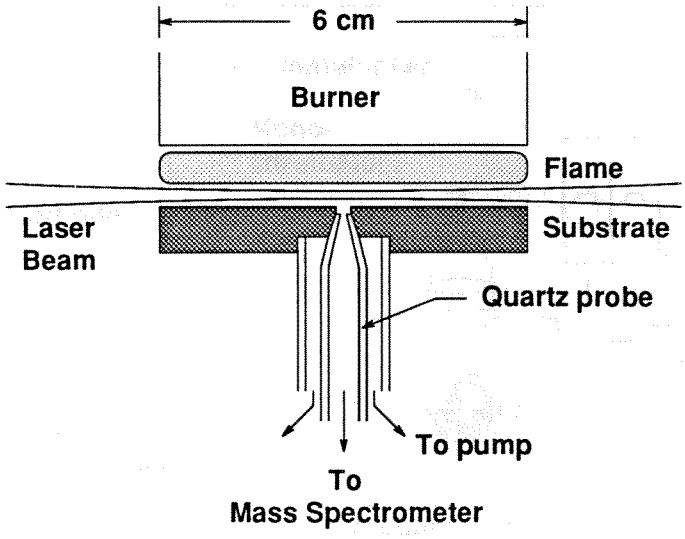

Figure 3.2: Schematic of experimental setup.

deposit diamond films. Axial OH relative concentration and rotational temperature profiles have been determined using laser-induced fluorescence (LIF). In addition, absolute mole fractions of C_2H_2, CH_4, H_2, and CO at the substrate have been measured using mass spectrometry for a range of equivalence ratios.

3.3 Experimental

The experimental configuration is shown schematically in Figure 3.2. The 6 cm diameter burner, described previously, is mounted in a downflow configuration. The burner surface temperature is measured by an ice-point-corrected thermocouple in one of the burner face holes near the center of the array. The substrate is mounted horizontally, approximately 1 cm below the burner surface. For the LIF experiments, the substrate consisted of a thin (0.5 mm) silicon wafer (10 cm diameter) which was

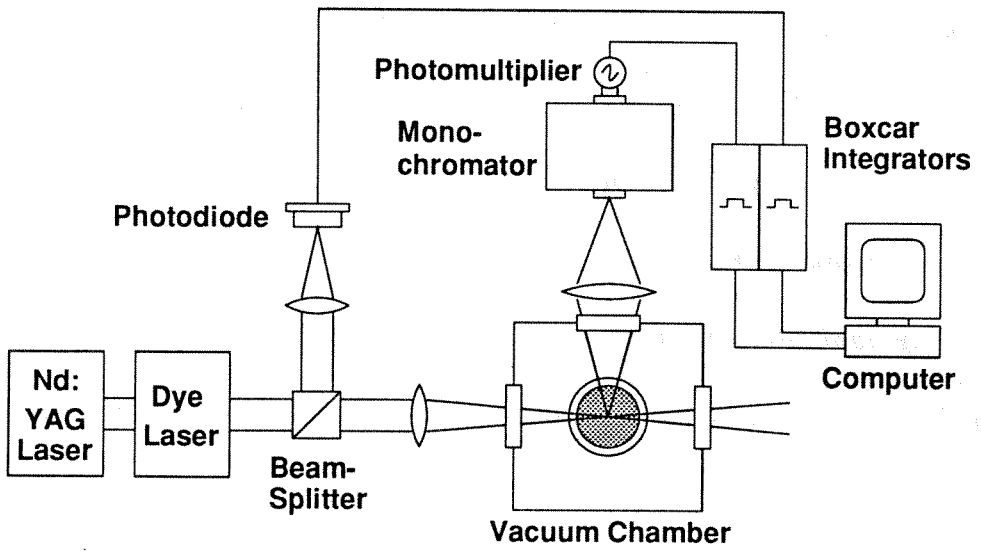

Figure 3.3: Experimental setup for LIF measurements.

thermally isolated from its holder by narrow ceramic supports. In the presence of the flame, the wafer rose to a steady-state temperature which was fairly uniform, to within ±25 K as measured by the two-color pyrometer, over at least the innermost 4 cm. The temperature was measured by an ice-point-corrected thermocouple cemented to the top of the substrate. For the mass spectrometry work, the silicon wafer was replaced by a 1 cm thick copper plate, 7.5 cm in diameter. A 1 mm hole in the center was drilled to allow gas to be sampled from near the surface.

The experimental arrangement for the LIF measurements is shown in Figure 3.3. To obtain axial profiles of rotational temperature, the experimental protocol established by Rensberger *et al.* [48] was used. A Nd:YAG laser pumps a dye laser (bandwidth 0.08 cm^{-1}) using DCM, and the output is frequency doubled and attenuated, yielding 7–8 ns pulses of $\sim$ 1 μJ energy tunable over the wavelength range from 309.2

to 309.7 nm. The beam is focussed into the flame with a 50 cm focal length lens. The laser is scanned over seven P and Q rotational branch lines with N″ ranging from 1 to 9 in the (0-0) band of the $A^2\Sigma^+ \rightarrow X^2\Pi$ transition in OH. Fluorescence is collected at right angles to the laser beam using f/5 optics through a 1/8 m monochromator to a photomultiplier. The monochromator slits are set with a narrow front slit (0.5 mm) and wide exit slit (3.0 mm) such that it serves as a flat bandpass filter (with bandwith 20 nm) over the entire rotational manifold of the (0-0) band. The fluorescence signal is sampled using a boxcar integrator (Stanford Research Systems SR250) with a short (10 ns), prompt detector gate to minimize effects of rotational-level-dependent collisional quenching [48]. A small portion of the beam is reflected from a sapphire beam splitter and directed to a UV sensitive PIN-type photodiode (Hamamatsu S1722-02). The photodiode measures laser power on a shot-to-shot basis, and these data are used to normalize the fluorescence signal. The linearity of the fluorescence signal with laser power is assured by operating at low laser energies. This was verified by plotting the fluorescence vs. laser power signal for laser power levels ranging from 0.8 to 2 μJ per pulse. These data are shown in figure 3.4. The data shown in figure 3.4 concur with the results of other investigators [48, 39], who found linear OH fluorescence signal behavior with laser power using Nd:YAG lasers, 50 cm focal length lenses, and laser energies of ≤ 1 μJ per pulse. Optical depth effects were measured by a separate absorption experiment, and the maximum uncertainty due to optical depth was calculated.

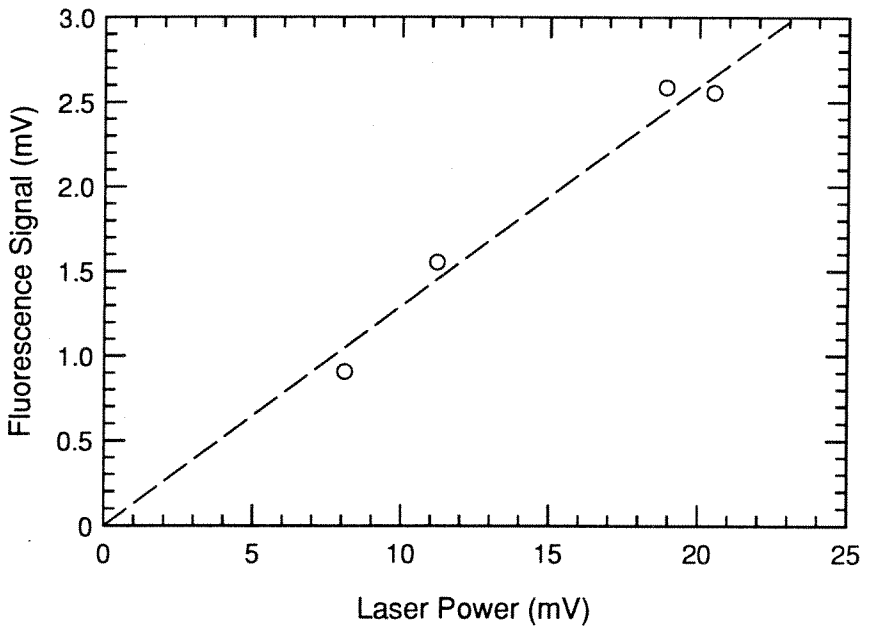

Figure 3.4: Fluorescence signal vs. laser power. 10 mV of laser power is $\sim 1\mu$J per pulse.

The burner and substrate can be translated relative to the laser beam. In this way, rotational temperature and relative OH concentration measurements were obtained at four locations in the flame. Blockage of the collection optics limits us to measurements further than 1 mm from the burner or substrate. The positional uncertainty is roughly $\pm$ 0.2 mm.

The experimental arrangement for the mass spectrometry measurements is also shown in Figure 3.2. Gas near the surface is sampled through the 1 mm diameter, 0.5 mm deep hole in the substrate by a quartz probe with an orifice opening of 400 μm. The pressure in the probe is maintained at 0.3 Torr. Gas in the region surrounding the quartz probe beneath the substrate is differentially pumped away to insure that

gas entering the mass spectrometer originates from the flame. After passing through a 0.5 m length of quartz tube, the sampled gas is directed to a quadropole mass spectrometer and analyzed. Absolute mole fractions were determined by calibrating the ionization signal of each species relative to Ar, using calibration mixtures of known composition (10% CO in Ar, 1% H_2 in Ar, and 0.5% CH_4 in Ar, all from Matheson Gas Products, Inc.). Ar mole fractions in the flame are then calculated using the flame model, and the mole fractions of the other species are inferred using Ar as a reference.

Several factors contribute to the uncertainty of these measurements. For the major species, background signal levels were negligible, and the uncertainty arises from the statistical variation in the measurements of relative ionization cross sections. This uncertainty is roughly $\pm 15\%$. For the minor species (C_2H_2 and CH_4), the signal to noise ratio is much lower, and thus there is additional statistical variation in the measurements themselves. This uncertainty varies depending on the species and concentration and can be appreciable at concentrations near the system detection limit.

Results: Fluorescence

The OH fluorescence measurements were carried out for a single flame with $P = 34$ Torr, $\Phi = 1.67$, total flow rate = 4 slm, $T_B = 993$ K, $T_S = 1068$ K, burner to substrate distance (D_S) = 0.92 cm. The flow rate corresponds to a cold gas velocity of 2.2 m/s.

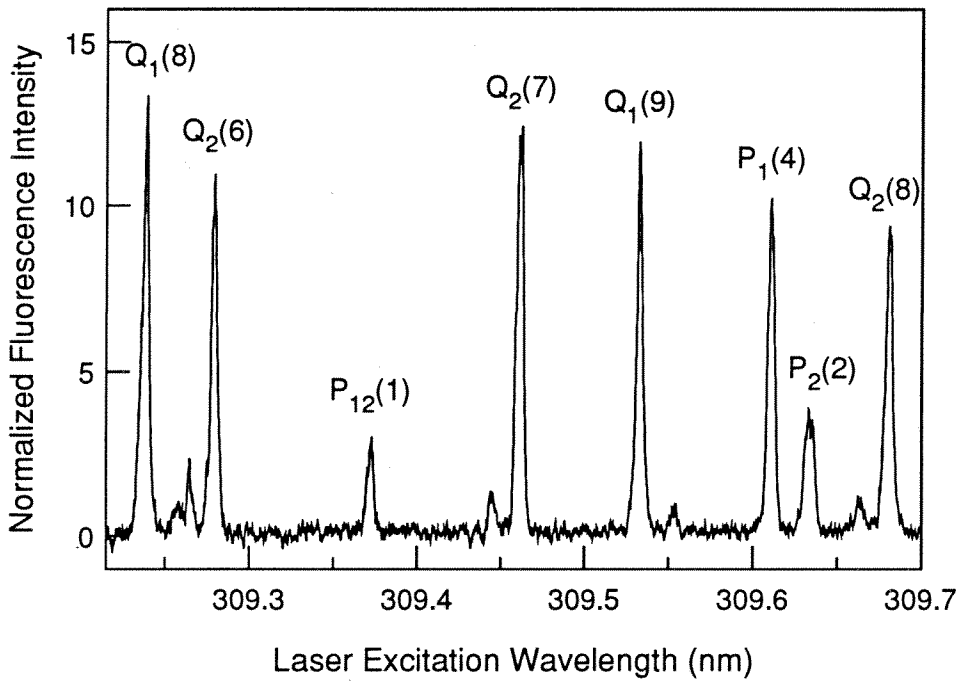

Figure 3.5: Typical fluorescence scan at x = 3 mm.

The maximum strain rate calculated from the flame model is 340 s^{-1}.

The normalized LIF spectra are analyzed by comparing the relative areas of the fluorescence lines. For most positions, the data are averaged over 2-3 scans. A typical scan is shown in Figure 3.5, and the resulting Boltzmann plot in Figure 3.6. Temperatures measured at four different locations in the flame are shown in Figure 3.7 along with the predictions of the flame code. The error bars show the statistical uncertainties in the linear fit to Boltzmann data, using 2σ uncertainties in the peak areas.

Absorption of the laser beam by the flame was below our detection limits, which is about 4%. From calculations assuming 4 percent absorption of the strongest line, we calculate a maximum temperature correction of -35 K. That is, the reported

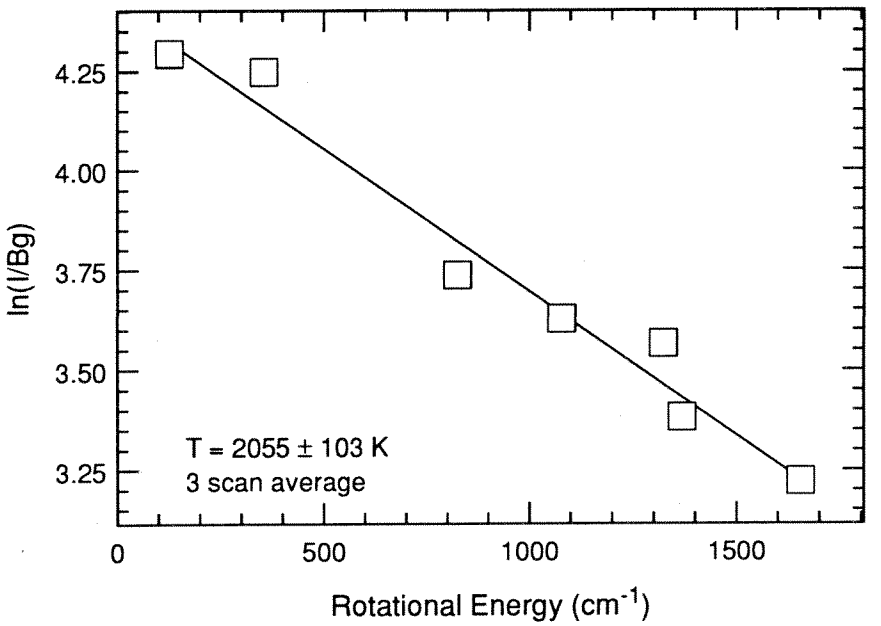

Figure 3.6: Boltzman plot for scans at x = 3 mm.

temperature is at most 35 K larger than the actual temperature.

The uncertainty varies from ± 100 K to ± 175 K. Within this level of uncertainty, the agreement of experiment and theory is good. Figure 3.7 also shows the calculated temperature for a flame with the same input flame parameters and no substrate. It can be seen that the predicted peak temperature of the flame with a substrate present is lower than that of the flame with no substrate, and our measurements support this prediction as well.

The agreement in the temperature profile between prediction and measurement is slightly better than that observed in many unstrained burner-stabilized flames. There are at least two possible reasons for this. First, in unstrained flames, the temperature is usually overpredicted the most in the post-flame zone where heat losses due to

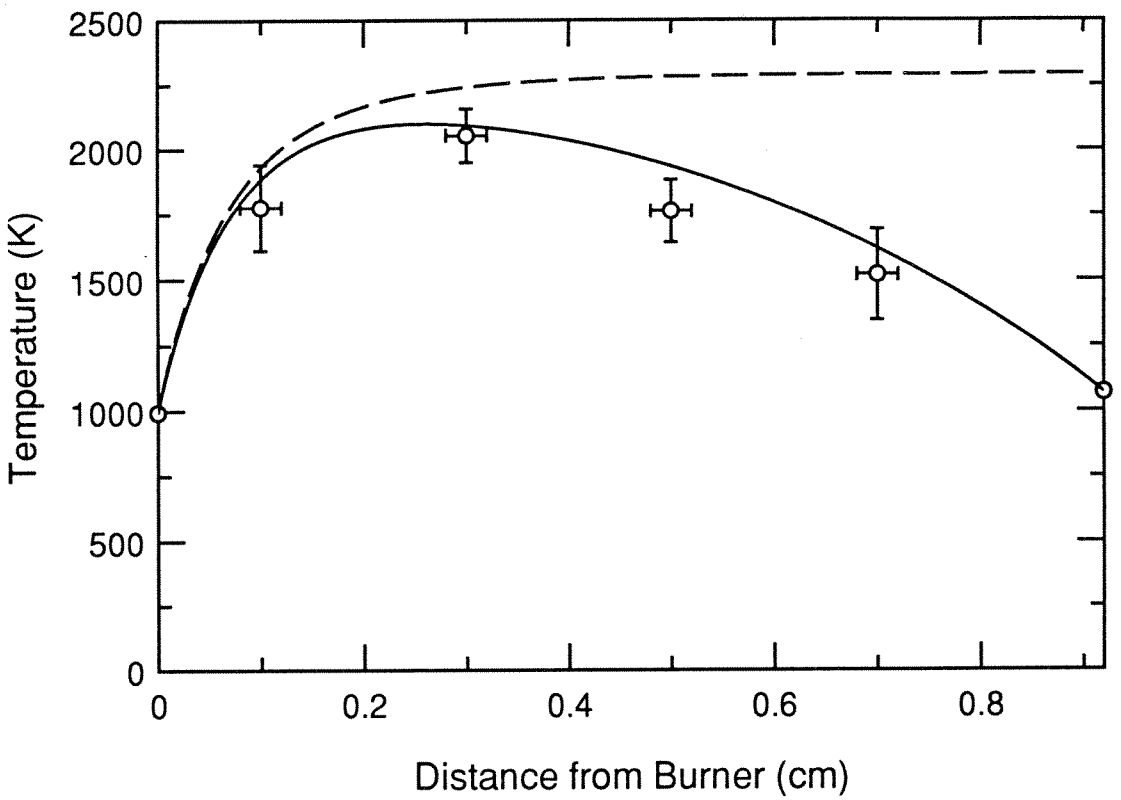

Figure 3.7: OH rotational temperature data and predictions of the model. The solid curve shows the predicted flame temperature with the substrate in place, and the dashed curve shows the temperature with no substrate.

radial conduction and radiation have accumulated enough to be appreciable. The predicted temperature profile in the reaction zone of the flame is often much closer to the measured profile. In the strained flames at 34 Torr, the reaction zone covers a substantial portion of the gap width, and there is only few mm of the gap which can be considered a post-flame region. Thus, because of the lack of a large post-flame zone, better agreement between predicted and measured temperatures is anticipated.

Second, in the region of the flame past the reaction zone, the primary heat loss mechanism is conduction to the substrate, which is accounted for in the model. It is possible that the heat loss to the substrate dominates any heat losses by radiation in these strained flames. In that case, better agreement in such flames is expected because the dominant heat loss mechanisms in the post-flame gases are accounted for, whereas in the unstrained flames the heat loss mechanisms in the post-flame gases typically are neglected.

Relative OH concentrations were obtained by measuring the relative area of the $Q_1(6)$ line at each location and correcting for the variation in Boltzmann fraction. The relative concentrations are shown in Figure 6, normalized to theory at $x = 3$ mm. Again, agreement with theory is good. The predicted effect of the substrate, in this case, is to reduce the OH concentration to 5% of its maximum value at $x = 8$ mm. This is compared to the case of a flame without the substrate in which the OH concentration at 8 mm is 95% of its maximum value. Our measurements are in agreement with the 5% prediction. It is to be noted that the surface recombination

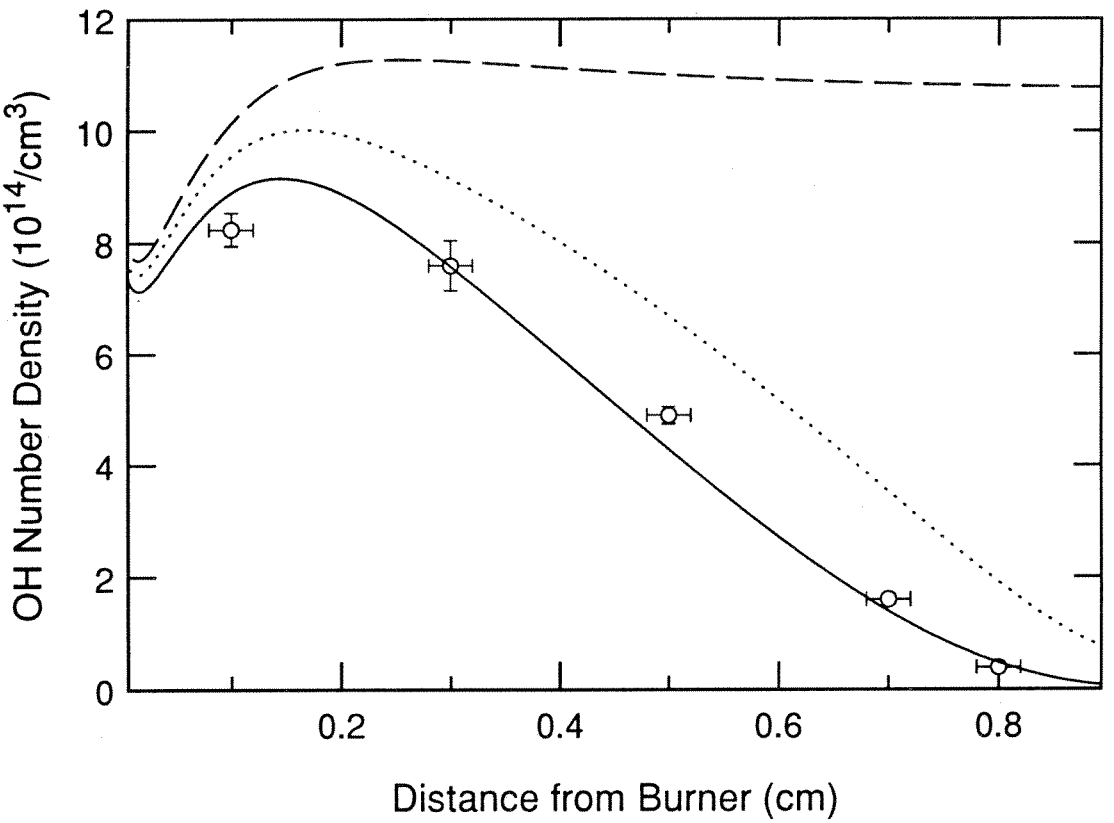

Figure 3.8: OH number density profiles. The measured values are normalized to the theoretical predictions at $x = 0.3$ cm. The curves are predictions of theory as follows: solid line, surface chemistry included; dotted line, no surface chemistry; dashed line, no substrate

of H, OH, and O strongly affects the OH concentration profile throughout the flame, not just near the substrate surface. However, when normalized to the predicted OH concentration profile obtained while neglecting surface chemistry, the experimental data fit equally well. Thus, though there are significant predicted differences in the absolute OH concentration when the surface chemistry mechanism is altered, our data cannot be used to evaluate the accuracy of the surface mechanism. However, the data clearly show the decrease in OH near the substrate due to the lower flame temperature.

Results: Mass Spectrometry

Absolute surface mole fractions for C_2H_2, CH_4, H_2, and CO were obtained at several gas mixture ratios ranging from $\Phi = 1.67$ to $\Phi = 2.25$. For these measurements, the experimental parameters are as follows: $P = 35$ Torr, total flow rate = 3.91 slm, $T_S = 900$ K, $T_B =\sim 840$ K, $D_S = 15$ mm, Ar dilution = 10%. Results of these measurements are shown in Figures 3.9–3.11. Also shown are the predictions of the flame model with and without a substrate present (for CO the two curves are indistinguishable). For H_2, the results match the predictions of the model to well within the experimental uncertainty. For CO, the agreement is not as good. However, the predicted mole fractions of CO are typically 10–15% below the predicted mole fractions, which is still within the experimental uncertainty. For C_2H_2 and CH_4 there is larger statistical uncertainty in the measurements, especially at low values of Φ, due

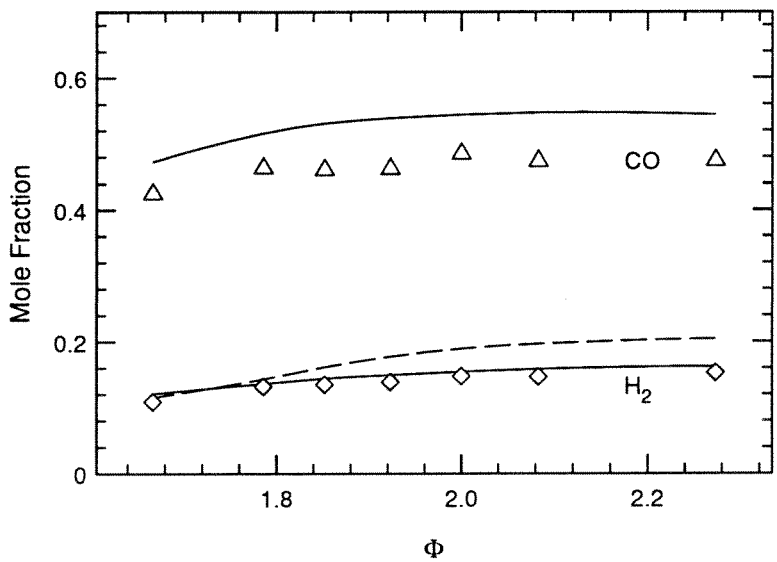

Figure 3.9: H_2 and CO surface mole fractions. The symbols represent experimental data, and the curves are the predictions of the flame model.

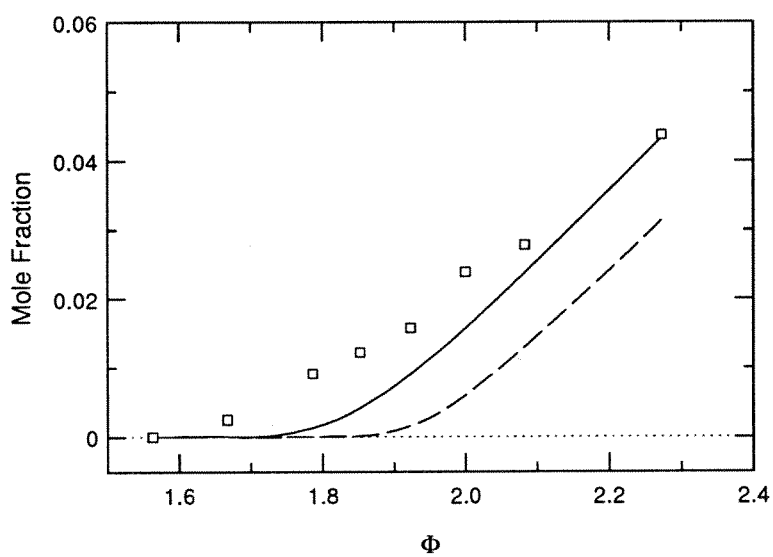

Figure 3.10: C_2H_2 surface mole fractions. The symbols represent experimental data, and the curves are the predictions of the flame model with a substrate present (solid line) and without a substrate (dashed line).

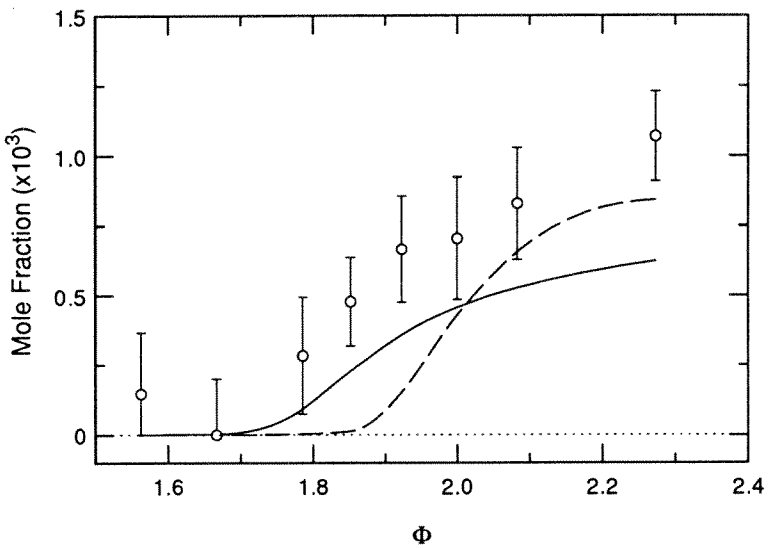

Figure 3.11: CH_4 surface mole fractions. The symbols represent experimental data, and the curves are the predictions of the flame model with a substrate present (solid line) and without a substrate (dashed line).

to the fact that both hydrocarbons are only present in amounts near or below our detection limit ($\sim 10^{-4}$ mole fraction). To ascertain background levels for C_2H_2 and CH_4, Φ was decreased until the signal level no longer dropped, and this was chosen as the background level, assuming that, for small Φ, both C_2H_2 and CH_4 are below detection limits. Even with the larger uncertainty, the predicted rise in both C_2H_2 and CH_4 mole fractions is fairly close to the rise observed in the experiments. In both cases, the model appears to slightly underpredict the concentration at the surface.

3.4 Discussion

Experimental observations of OH rotational temperature, OH axial profiles, and stable species surface concentrations have reproduced many of the flame features predicted by our stagnation-point flame model.

The OH rotational temperature measurements suggest that the model predicted temperature is good at least to within 175 K throughout the gap region. The predicted OH relative concentration profile shows excellent agreement with the LIF measurements.

The mass spectrometry data also indicates that the model is capable of predicting major species to within experimental uncertainties and minor species to within a factor of two. Perhaps more importantly, the decay trends in C_2H_2 and CH_4 concentrations at the substrate with decreasing Φ are predicted well qualitatively.

No conclusions can be drawn about the accuracy of the surface chemistry mecha-

nism, although the model predictions indicate that an absolute measurement of OH concentration a few mm above the substrate may be sensitive to changes in OH surface chemistry. Such a measurement might be useful in refining surface reaction rates for OH.

Chapter 4

Low Pressure Acetylene/Oxygen Flames

4.1 Overview

The work described in this chapter attempts to further the understanding of diamond growth in low pressure, acetylene/oxygen flat flames. Initially, an extensive set of deposition experiments was performed. The results of these experiments yield information on which experimental conditions lead to growth of diamond particles and which do not. This set of experiments also provides information on diamond growth rates and nucleation densities in these environments.

The model described in Chapter 3 is used to analyze the experimental data in terms of the chemical environment at the growth surface. Comparisons of the typical growth environment in a low pressure flat flame with that of an atmospheric pressure torch and a hot filament reactor are made, and the important differences are noted.

The model is also used to help explain why diamond grows under the observed experimental conditions. Several flames at or near diamond growth conditions are analyzed with the model, and the results are used to help explain why small variations in experimental conditions lead to either non-diamond deposits or no deposit.

Lastly, the results of the initial study are used to suggest reasons why continuous diamond films are difficult to grow in low pressure flat flames and also to speculate on experimental conditions which might lead to continuous films.

4.2 Experimental

For the experiments discussed here, the standard setup described in Chapter 2 was used. The experimental parameters varied were the oxygen to acetylene ratio in the premixed gases (R), the total specific flow rate, the burner temperature (T_B), the substrate temperature (T_S), the burner to substrate distance (D_S), and the system pressure (P).

To minimize the area of parameter space to search, the system pressure was fixed at either 35 or 40 Torr for most of the runs. Total specific flow rates of either 0.126 or 0.159 slm/cm^2 of burner surface were used. At 0.159 slm/cm^2, the burner surface temperature rose to its maximum design value of 1000 K. Thus, with this burner, this was the maximum flow rate possible. The remaining three parameters were then altered to find appropriate conditions for diamond growth.

Since heat from the flame alone, in the chosen operating regime, provided insufficient substrate temperatures for diamond growth ($T_S < 700$ °C), a substrate heater was employed. Heating was accomplished either indirectly by exposing the underside of the substrate to a nichrome heating element, or directly by passing current through the substrate. The resistive heating method offers the greatest range of operation, allowing for temperature control from below 970 K to the melting point of silicon (~1700 K). Details of the substrate holders used are given in Appendix C.

Each of the experimental variables has an associated uncertainty. Pressure in the chamber was maintained either manually to within ± 2 Torr, or, in later experiments,

by a throttle valve controller to within ± 0.5 Torr. The burner to substrate distance (D_S) was measured accurately to within 0.25 mm. Substrate surface temperatures were measured by one- and two-color pyrometers on silicon. One-color and two-color (using emissivity slope of 1.0) pyrometer measurements were shown to agree with thermocouple temperature measurements to within ±35 °C on molybdenum substrates. Similar uncertainties are expected for silicon substrates.

The chemical environment near the substrate surface and over the bulk of the flame was predicted by the model to be insensitive to the burner surface temperature T_B in our regime of operation. Thus, the burner surface temperature was not measured in each run. For the purposes of computation, the burner temperatures for each run were estimated using burner temperature data from a set of similar runs. Thus, the uncertainty in T_B is estimated at ± 100 K and is not expected to affect the accuracy of the predictions of the model.

The most significant uncertainty in any parameter is in the determination of the oxygen to acetylene ratio R. The source of the uncertainty is a variation in mass flow rates due to impurities in the feed gases. The thermal mass flow controllers used employ a calibration factor for each gas which is related to its heat capacity. Significant amounts of impurities can alter the thermal properties of the gas enough to induce errors in flow rate much larger than the standard instrument error, specified at 0.5% of full scale. Industrial acetylene has a listed purity of 98.5%, not including acetone. Acetone arises as a by-product of acetylene reacting with the binder in

the acetylene bottle. Acetone content varies with bottle discharge pressure and can be several percent when the bottle is near empty. In our setup, the acetylene feed gas is passed through one, or in some cases two, activated charcoal filters to control acetone content. In addition, before each run, the mass flow controller is calibrated relative to previous runs. If the flow varies from the average of previous runs by more than $\pm 2.5\%$, the bottle is not used. Use of high purity acetylene has, for some runs, helped to minimize the deviation to within 1%. However, the bulk of the growth runs were performed with industrial acetylene, and this leads us to an uncertainty in R of $\sim 2.5\%$. Additional uncertainties due to unknown effects of impurities and acetone in the feed gases are not quantified.

4.3 Results

Growth Conditions

Several regions of the experimental parameter space were found to grow faceted diamond. In all cases, when diamond was observed, it was only in the form of isolated diamond crystals. No continuous films were observed in these initial experiments. (Film growth conditions were later achieved with a modified setup. Those experiments are discussed in Chapter 5.) A partial listing of growth conditions is given in Table 4.1. Detailed results of over 70 growth runs are given in Appendix A.

Diamond deposits were observed at 35–40 Torr and T_B of 750–1000 K for R values

Case	R	Flow (slm/cm^2)	T_S (K)	P (Torr)	D_S (mm)
1	1.35	0.126	1198	40	6
2	1.30	0.126	1223	40	6.6
3	1.30	0.126	1223	40	7.3
4	1.20	0.159	1223	40	6.7
5	1.30	0.159	1238	40	8
6	1.34	0.159	1238	40	8
7	1.38	0.127	1223	35	7.5
8	1.25	0.127	1123	35	7.5

Table 4.1: A listing of some observed conditions for diamond growth.

ranging from 1.2 to 1.4, for T_S from 1123 K to 1238 K, and for D_S from the extinction limit ($\sim$ 6 mm at 40 Torr) to 8 mm.

Deposits were screened for diamond content by optical and scanning electron microscopy and verified as diamond by macro-Raman spectroscopy. Typical laser spot sizes for the Raman spectra were < 100 μm. The Raman spectrum in Figure 4.1 is typical of the better quality diamond deposits obtained. The sharp peak near 1332 cm^{-1} corresponds to the C-C stretch in the diamond lattice. The shoulder at 1300 cm^{-1} and the broad peak near 1550 cm^{-1} correspond to various forms of disordered carbon [49]. Raman spectroscopy is especially sensitive to diamond impurities. Even in cases where faceting is clearly observed in the deposit, the non-diamond broad peaks can sometimes be large enough to obscure the diamond signal. Thus, a clear sharp peak at 1332 cm^{-1} indicates the presence of high quality diamond with small non-diamond impurities.

Deposited diamond varied in quality over a wide range. Examples are shown in Figures 4.2–4.5. Flames slightly on the rich side yielded heavy secondary nucleation on diamond facets as seen in the Figures 4.6 and 4.7. Etched diamond particles were also observed in some of the leaner flames. An example is shown in Figure 4.8. If a diamond deposit was subjected to a flame too lean to deposit diamond, then the diamond deposit was oxidized. Figure 4.9 is a photograph of the remnants of a deposit in which a lean flame has etched away the diamond and left tiny diamond fragments.

Several forms of non-diamond carbon were observed. Some of them are shown

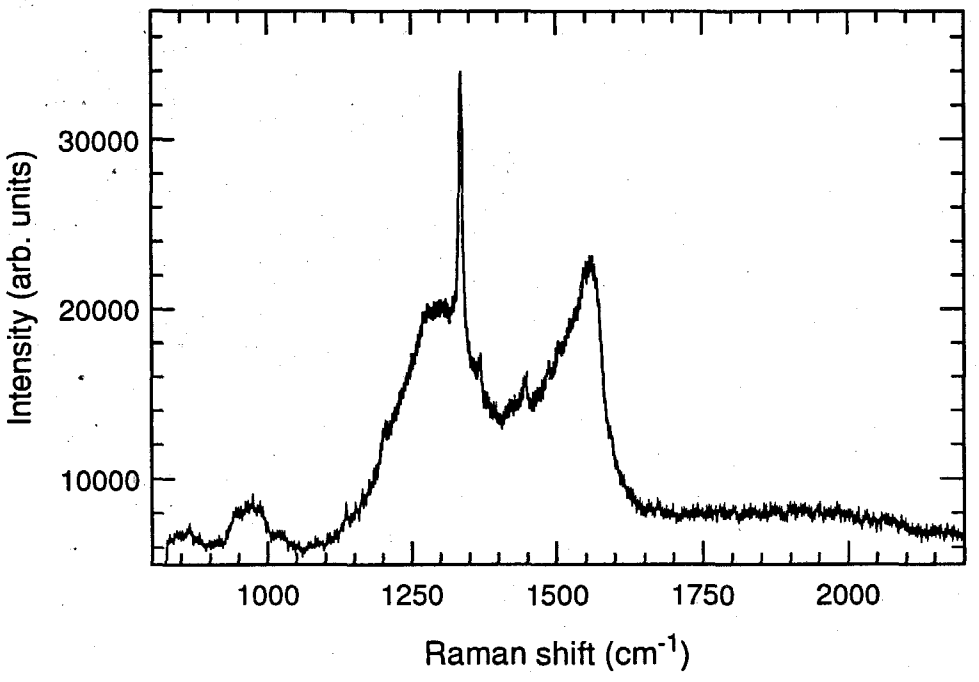

Figure 4.1: Typical Raman spectrum from isolated diamond crystals.

in Figures 4.10–4.12. Figure 4.10 shows a deposit of micro-crystalline graphite while Figure 4.11 shows a more commonly seen deposit of disordered, non-diamond carbon. This type of deposit was the most common form observed in growth runs too rich for diamond growth. Figure 4.12 shows isolated ball-like carbon particles. These were also often seen in areas of the parameter space near diamond growth conditions.

No continuous diamond films were grown in this region of the parameter space. When isolated diamond particles grew to sizes in which the deposit approached a semi-continuous film, the chemical environment at the substrate shifted from conditions of diamond deposition to conditions in which only non-diamond carbon was deposited. An example of this is shown in Figures 4.13 and 4.14. Figure 4.13 shows a deposit

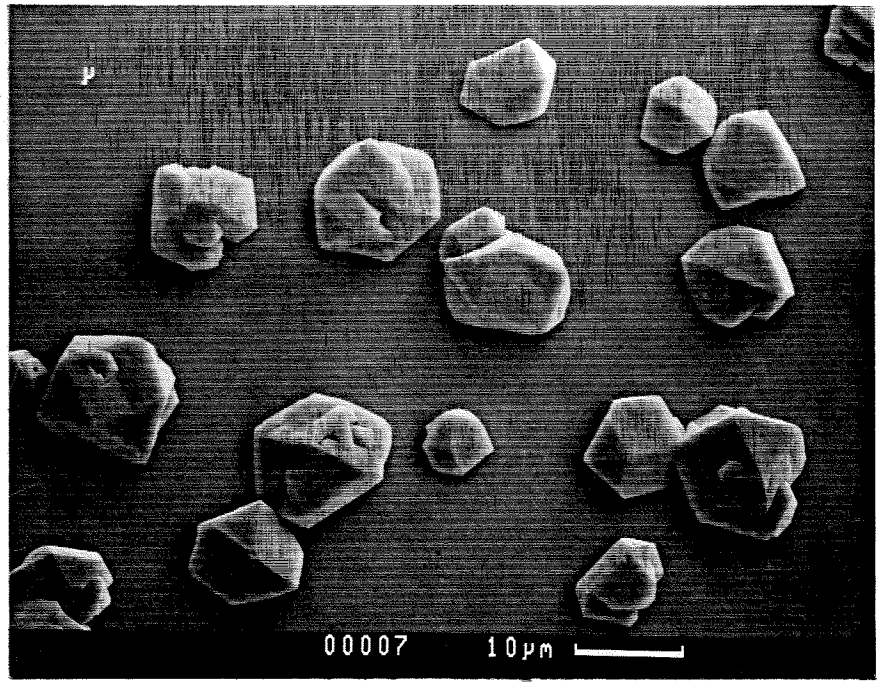

Figure 4.2: High quality isolated diamond particles.

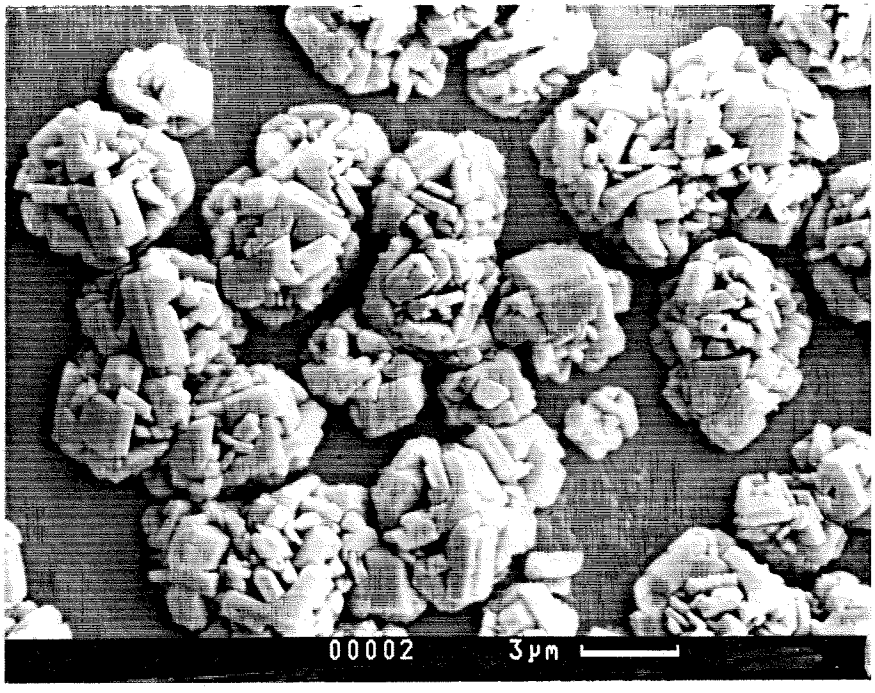

Figure 4.3: High quality diamond with some etch pits.

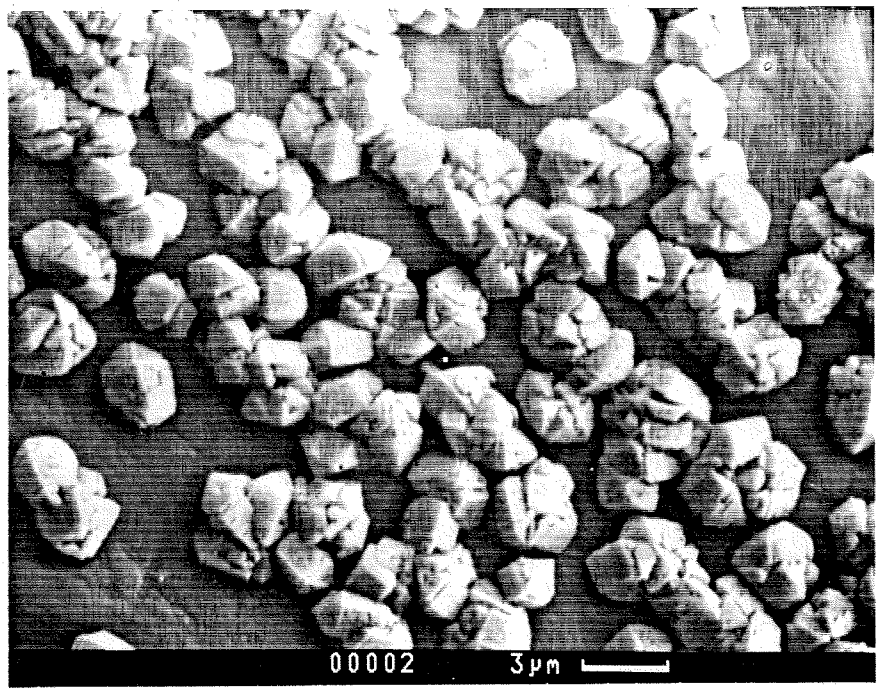

Figure 4.4: Lower quality diamond with less faceting.

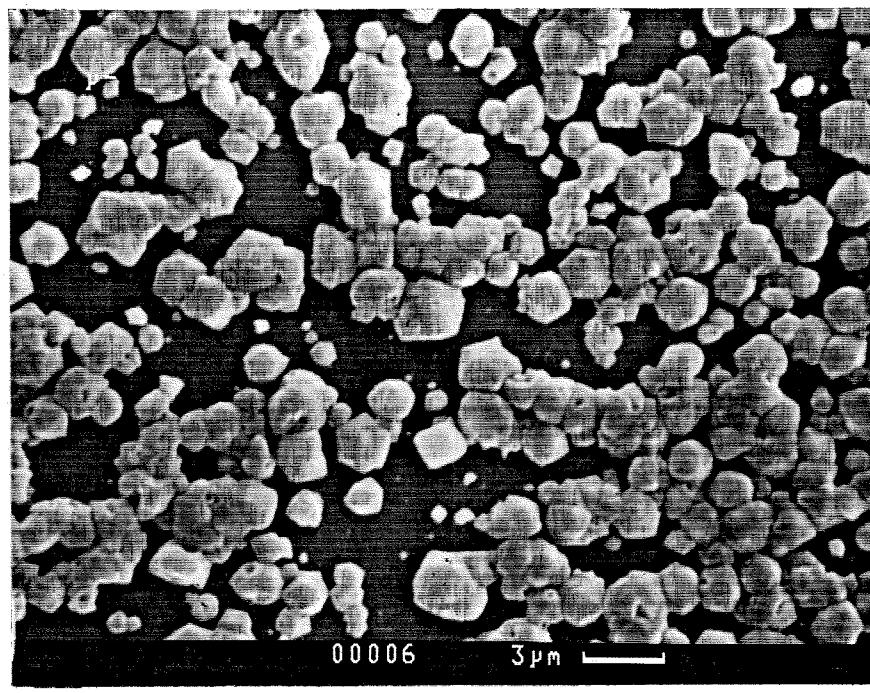

Figure 4.5: A diamond deposit with minimal faceting.

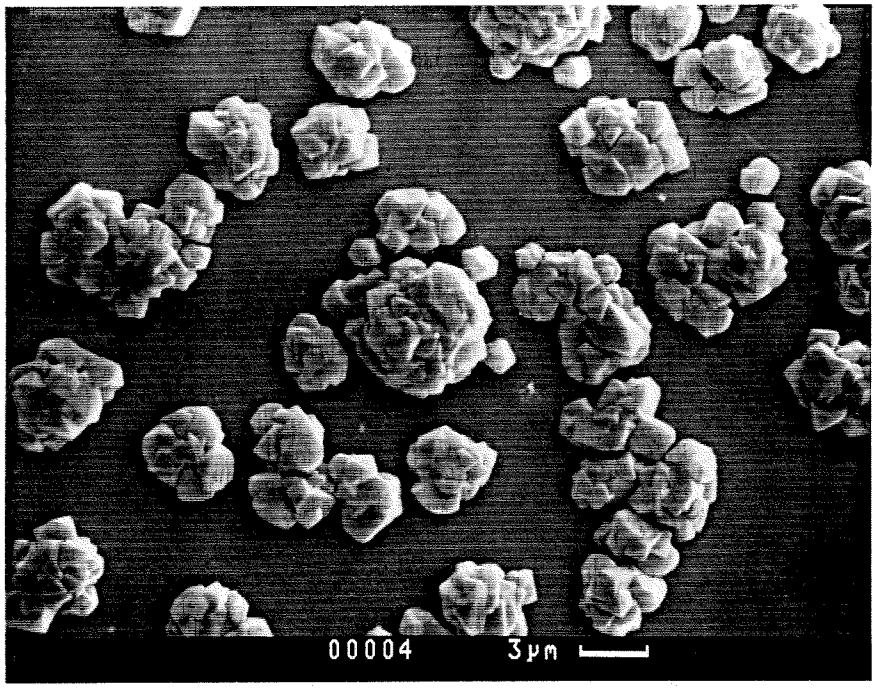

Figure 4.6: Diamond with some secondary nucleation.

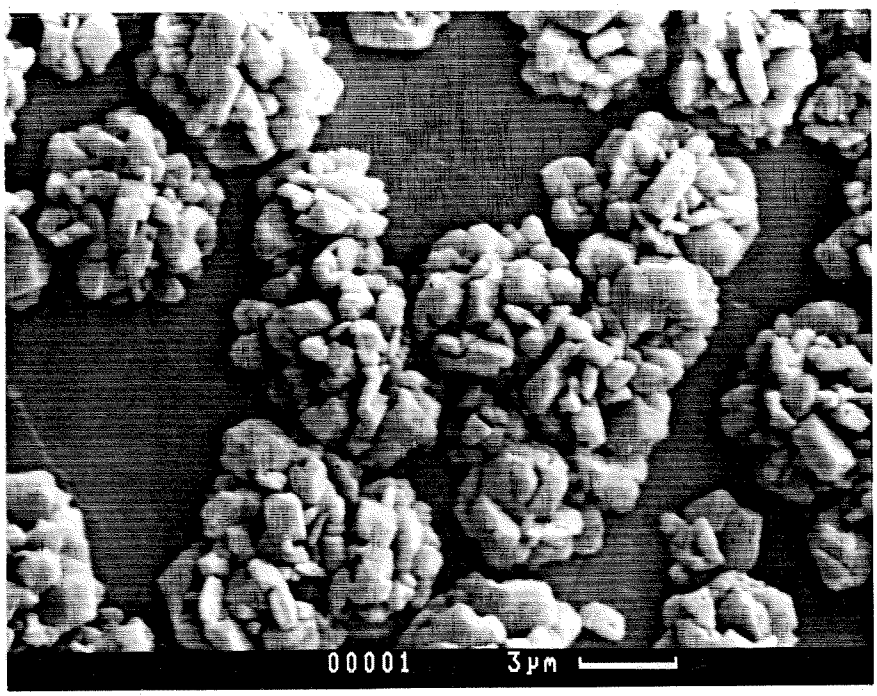

Figure 4.7: A diamond deposit with extensive secondary nucleation.

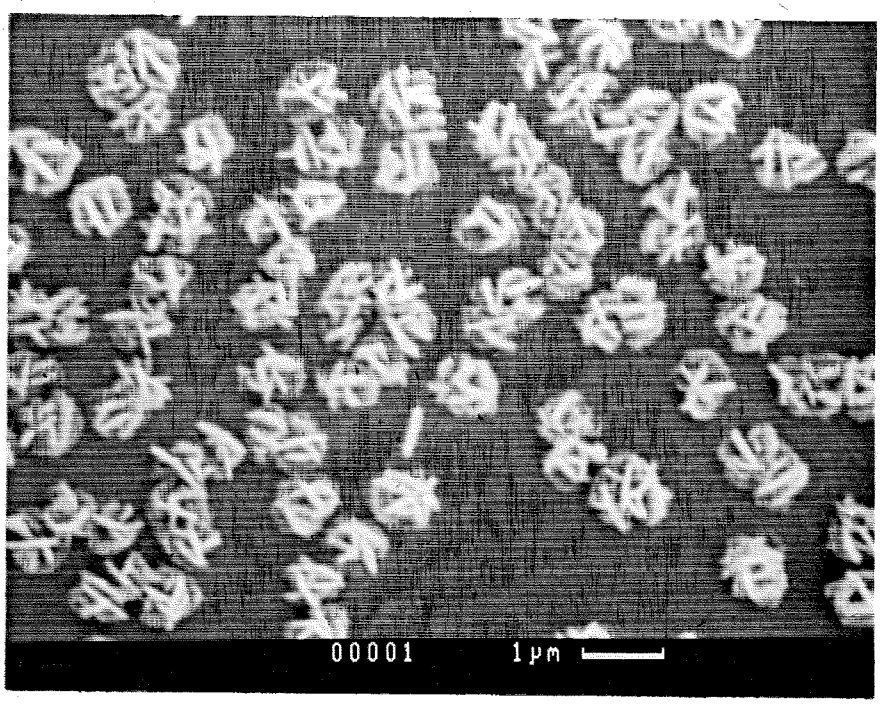

Figure 4.8: Etched diamond particles.

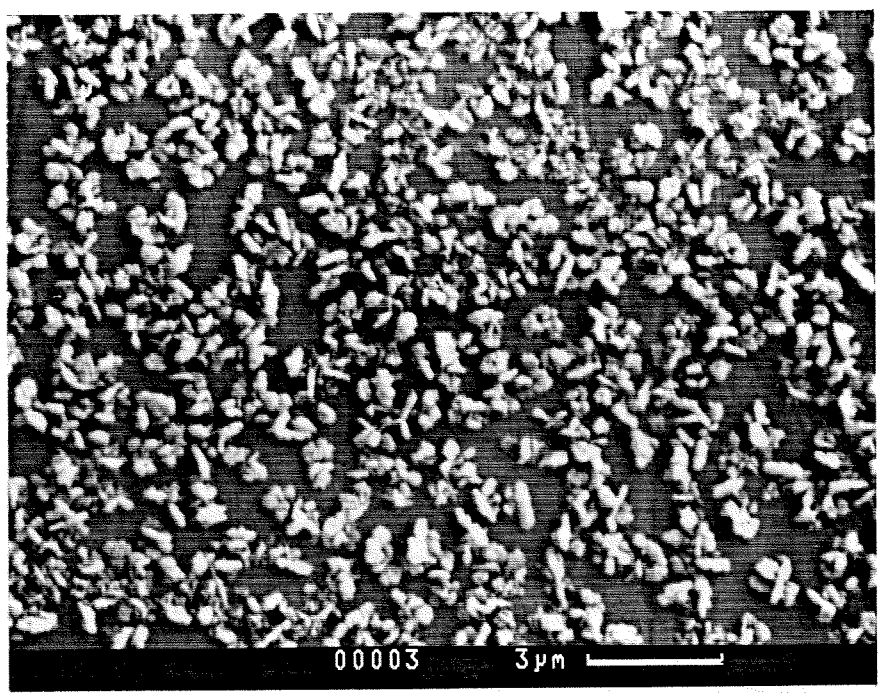

Figure 4.9: Etched remnants of a continuous film.

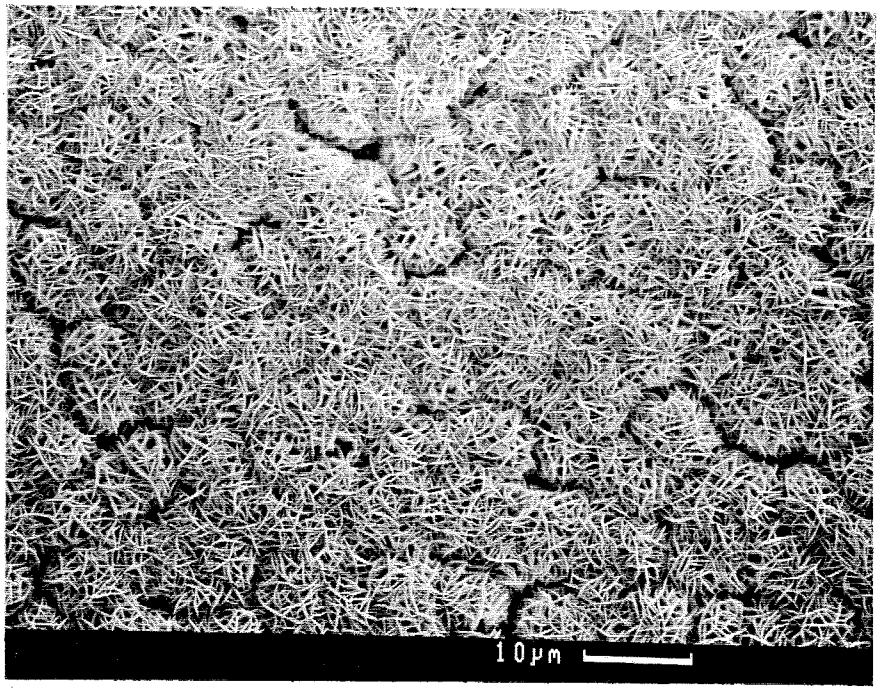

Figure 4.10: Micro-crystalline graphite deposit.

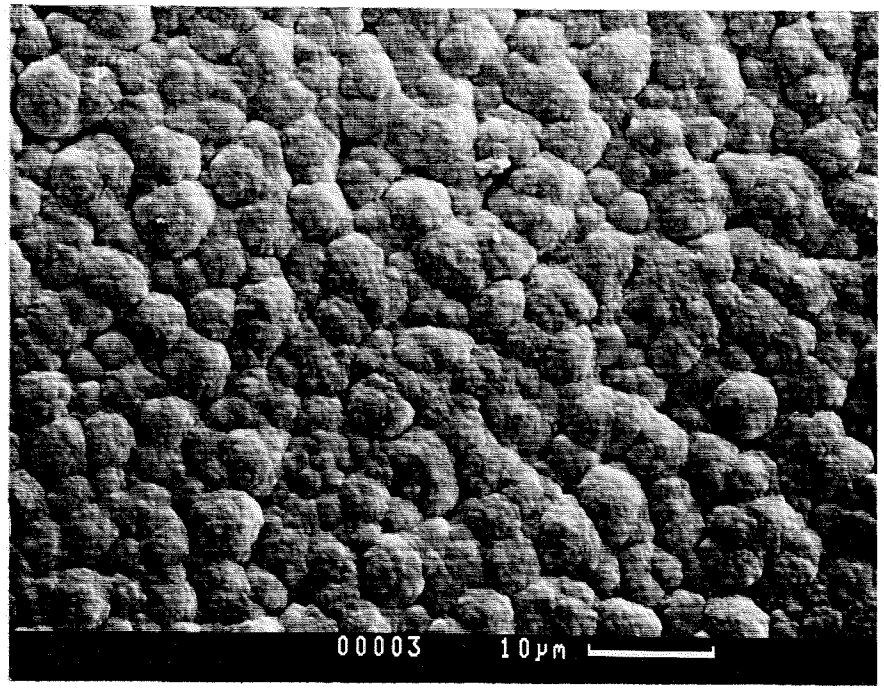

Figure 4.11: Disordered, non-diamond carbon.

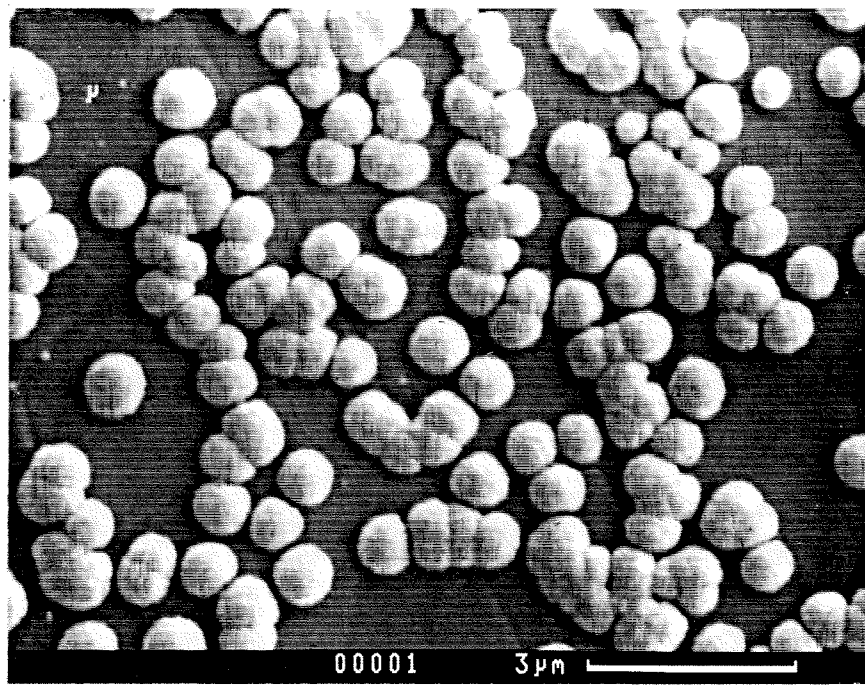

Figure 4.12: Ball like carbon deposit.

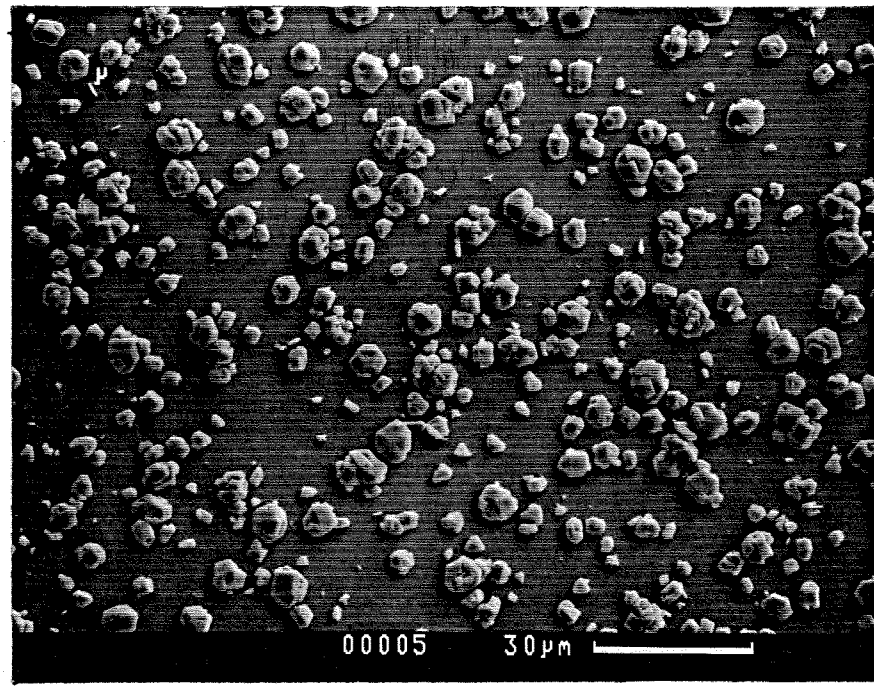

Figure 4.13: Diamond deposit after 6 run hours.

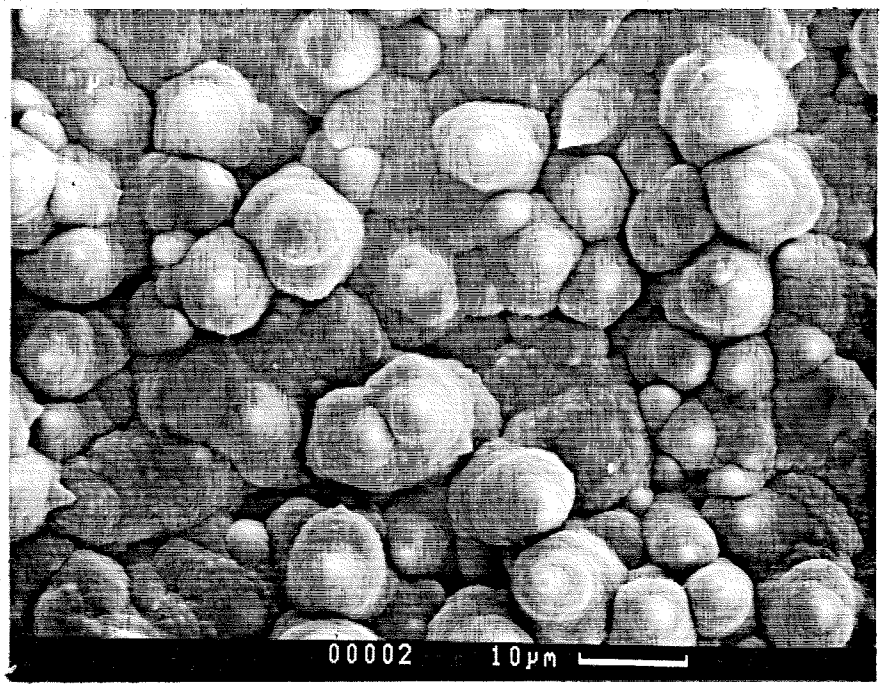

Figure 4.14: Film obtained after 20 run hours (same run conditions as in Figure 4.13).

obtained after six hours of deposition. The diamond quality and faceting are excellent. The presence of etch pits on some of the particles suggests even that the environment was more oxidizing than a typical flat flame deposition environment. However, when the same experimental conditions were run for 20 hours, the continuous film of Figure 4.14 resulted. Note that some diamond exists, but the predominant deposit is non-diamond. No peak at 1332 cm^{-1} in the Raman spectrum was observed.

To counteract this effect, several runs were performed in which the flame was shifted to slightly leaner (more etching) conditions as the film became continuous. The observed result was that the deposit was simply etched away. This phenomenon was observed in all diamond growth conditions which were run until continuous films

developed.

In an effort to grow continuous films, cycling of flame chemistry was attempted. Such a procedure has met with considerable success in work with hot filament reactors [50] and other methods. In this procedure, a short period of nucleation enhancement (see below) is followed by a longer run at a flame condition known to produce diamond particles. The growth proceeds until the film is nearly continuous. After this, the flame is cycled between a growth condition and an etching condition. The intent is to deposit diamond and non-diamond during the growth cycle and to etch away the non-diamond and some (but hopefully not all) of the diamond during the etch phase. Approximately 20 growth runs (cataloged in Appendix A) were performed using known growth and etching conditions and varying cycle times and ratio of growth to etch durations. The results yielded the highest density of isolated diamond particles with no visible non-diamond deposit. An example is shown in Figure 4.15. However, despite this increased success, no diamond film growth conditions were found. Some partially faceted continuous films were grown (e.g., Figure 4.16), but the diamond quality was extremely poor, and the non-diamond content was very high.

Nucleation

Nucleation density varied with substrate material, preparation, and experimental conditions. In general, richer flames led to higher nucleation densities. This is shown in Figure 4.17 which shows nucleation density data for a short series of runs on

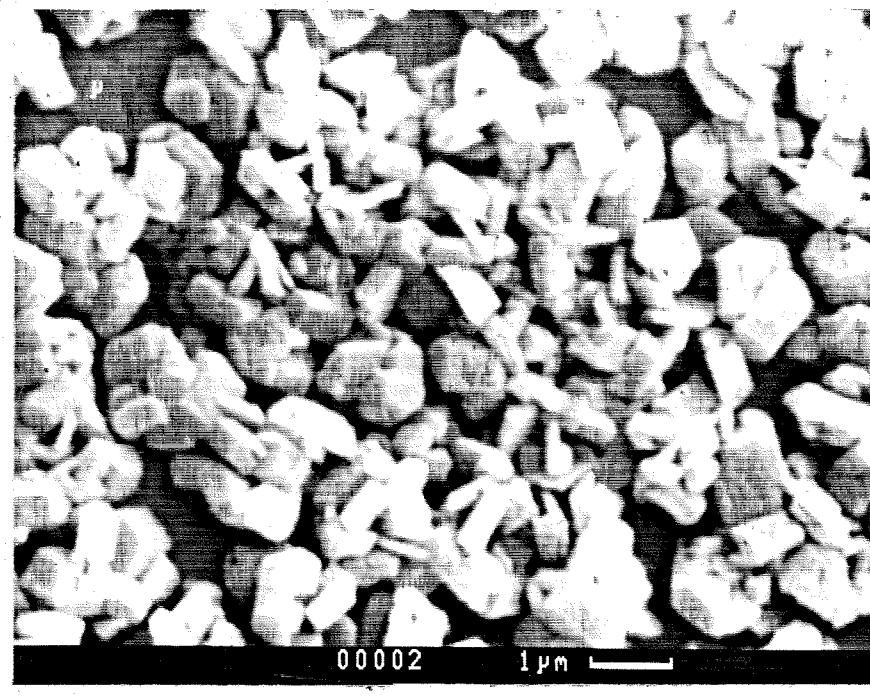

Figure 4.15: A semi-continuous diamond film grown by cycling of R.

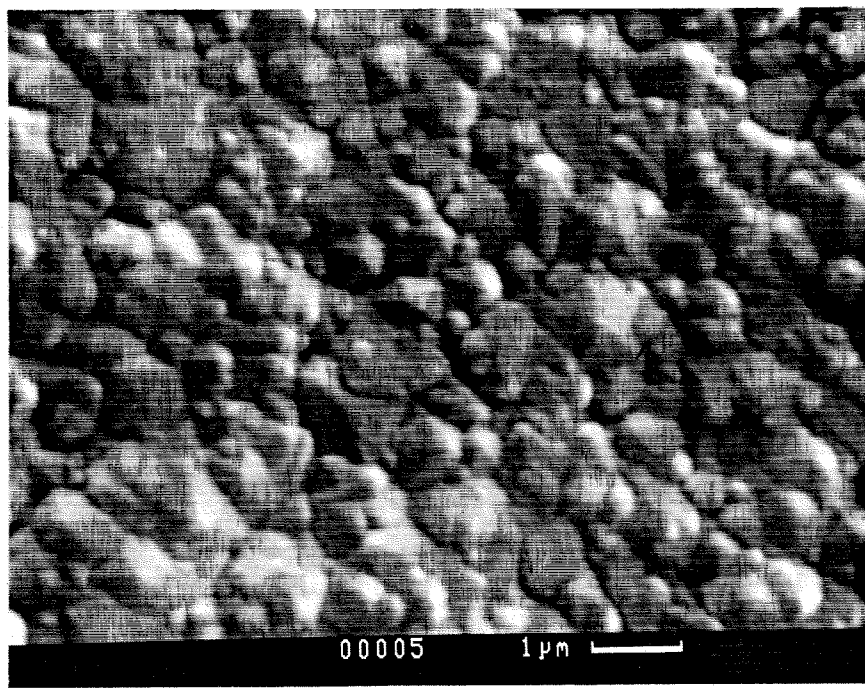

Figure 4.16: Continuous film with some faceting grown by R cycling.

molybdenum with T_S = 1223 K, D_S = 7.5 mm, 0.126 slm/cm^2, and R ranging from 1.29 to 1.38. This phenomenon was used in many runs to increase nucleation density by running the flame rich for a short period early in the experiment, then switching to the run condition. Considerable success was achieved with this method. However, if the initial nucleation enhancement period was sufficiently long to allow nuclei to form a continuous film of poor quality diamond or non-diamond, then the subsequent deposit would be non-diamond, even if a condition which normally yielded diamond isolated particles was used. If the subsequent flame was too oxidizing for diamond growth, then the non-diamond deposit would simply be etched away. No growth of diamond on non-diamond carbon or on a continuous film of diamond was ever observed.

The observed nucleation density under deposition conditions was sparse compared to other diamond growth methods of similar growth rate. (e.g., hot filament). When using polished silicon or molybdenum substrates scratched with diamond paste before deposition, the average distance between nuclei under hot filament conditions is usually less than 1 micron. Thus, isolated diamond crystals form a film when crystal radii exceed 0.5 microns. Typical average distances between nuclei in the flat flame environment on unscratched substrates were 5-100 microns. For scratched substrates, nucleation occurred predominantly in and along the scratches on the substrate made by the diamond particles in the paste. Overall, the nucleation density was much higher but still nearly an order of magnitude smaller than typical hot filament con-

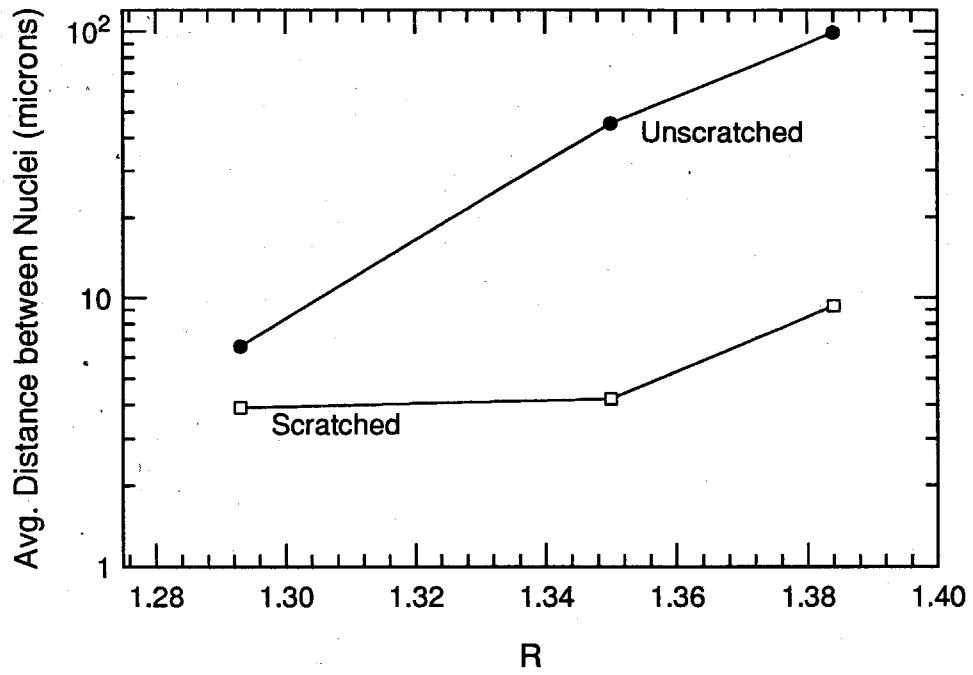

Figure 4.17: Nucleation density vs R for a series of runs.

ditions. A series of runs using molybdenum substrates with one quadrant scratched and the other three left untouched was performed to test the effect of scratching on nucleation density. The results are also shown in Figure 4.17. In general, scratching increased nucleation density by up to a factor of 10 or more.

The growth rate also varied somewhat with nucleation density in many samples. In higher areas of nucleation density (e.g., scratched portions of the substrate), the growth rate was often lower by as much as a factor of 2. Several examples are shown in Figure 4.18. The plot also suggests that the particle growth rate often exhibits a stronger dependence on nucleation density than on R.

In cases in which there was a non-uniform deposit due to either a slight T_S non-

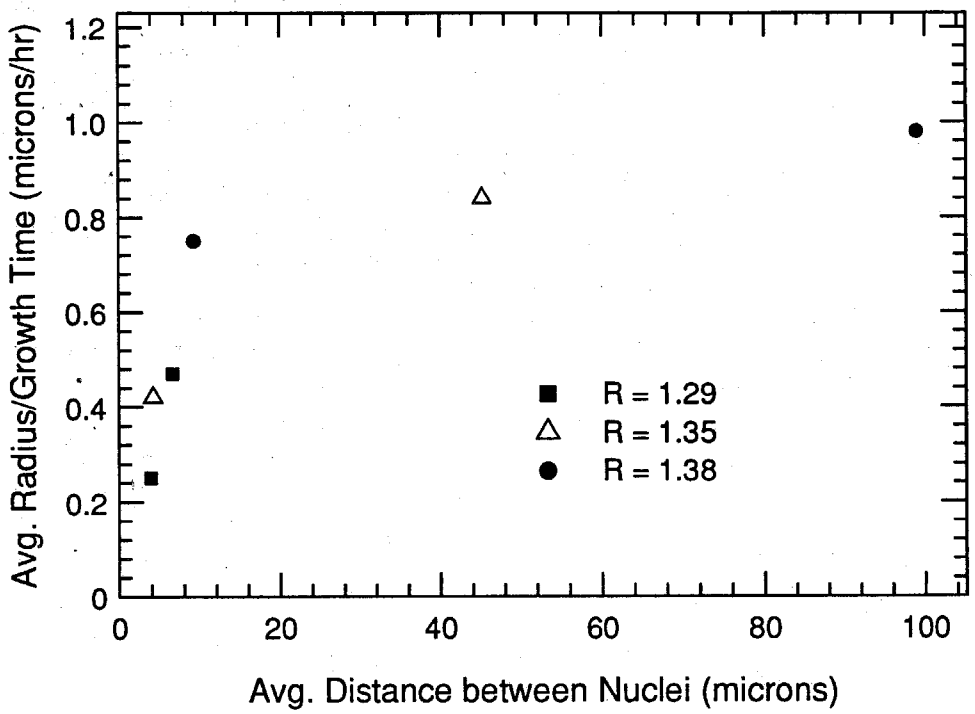

Figure 4.18: Growth rate vs. nucleation density. This is the same series of runs as Figure 4.17

uniformity or some other factor, often the lowest growth rates of diamond were observed at the edges of the deposit region. This was also where the highest quality diamond would be observed. In many cases, the central deposit would be non-diamond, and the edge of the deposit would be diamond. The four photographs of Figures 4.19–4.22 show a clear example of this.

Observed Trends

In general, the following trends were observed when moving within the parameter space near a diamond growth condition. If the value of R was increased above that

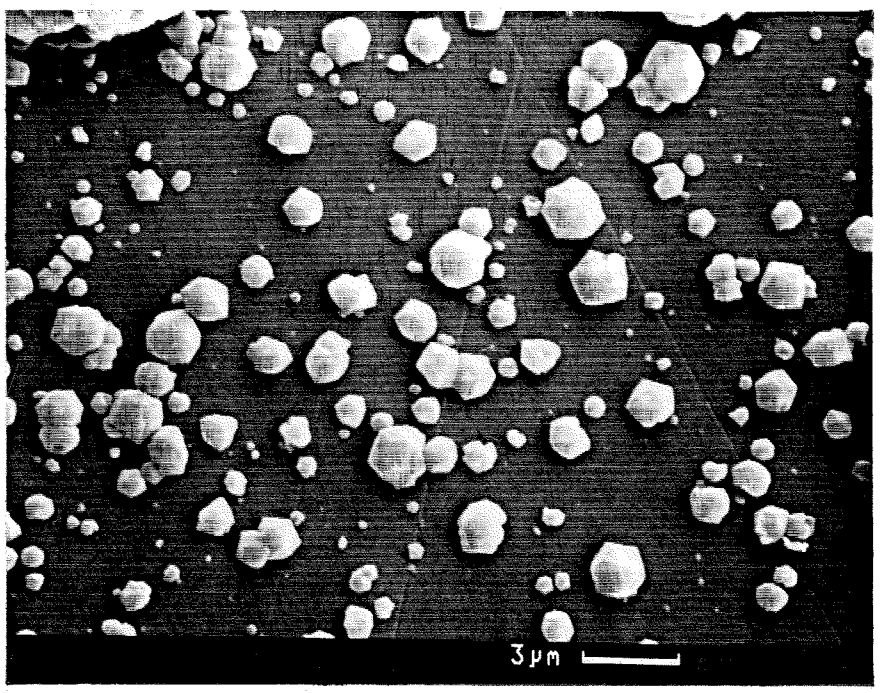

Figure 4.19: Faceted diamond at the edge of a deposit region.

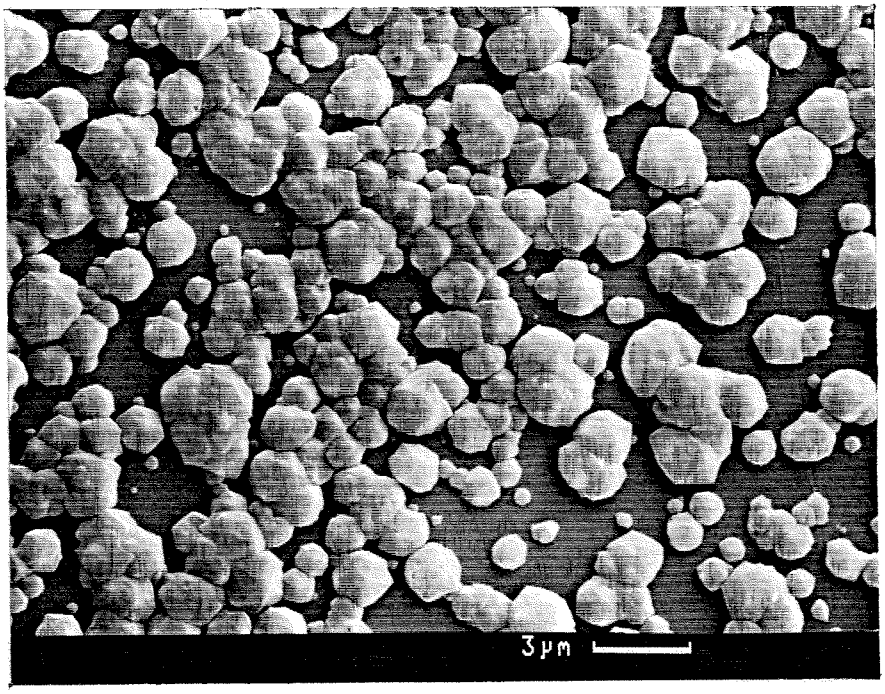

Figure 4.20: The same deposit as Figure 4.19 but slightly closer to the deposit center.

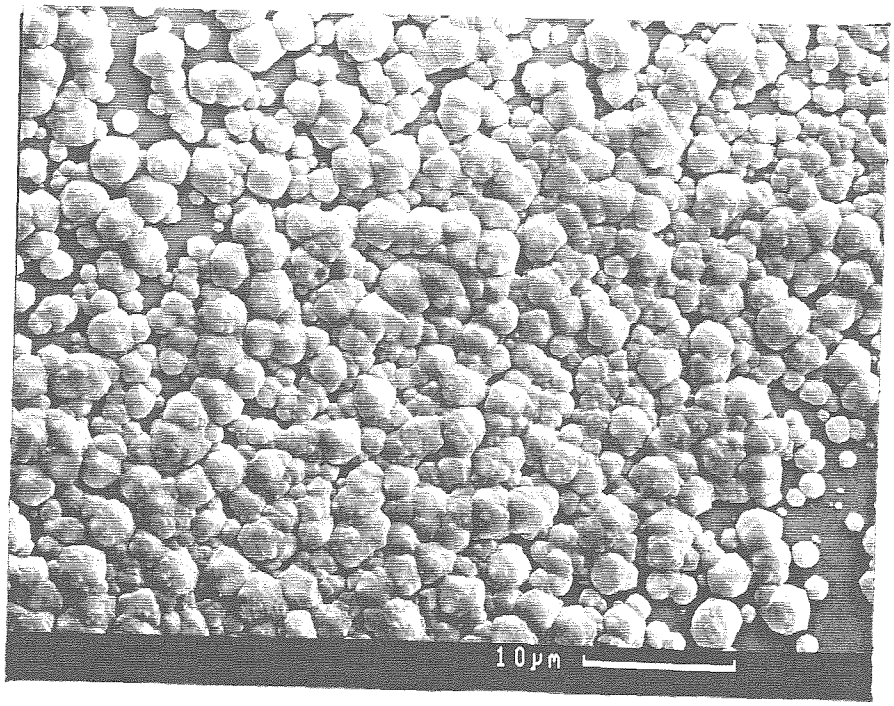

Figure 4.21: Particles still closer to the deposit center than those in Figure 4.20.

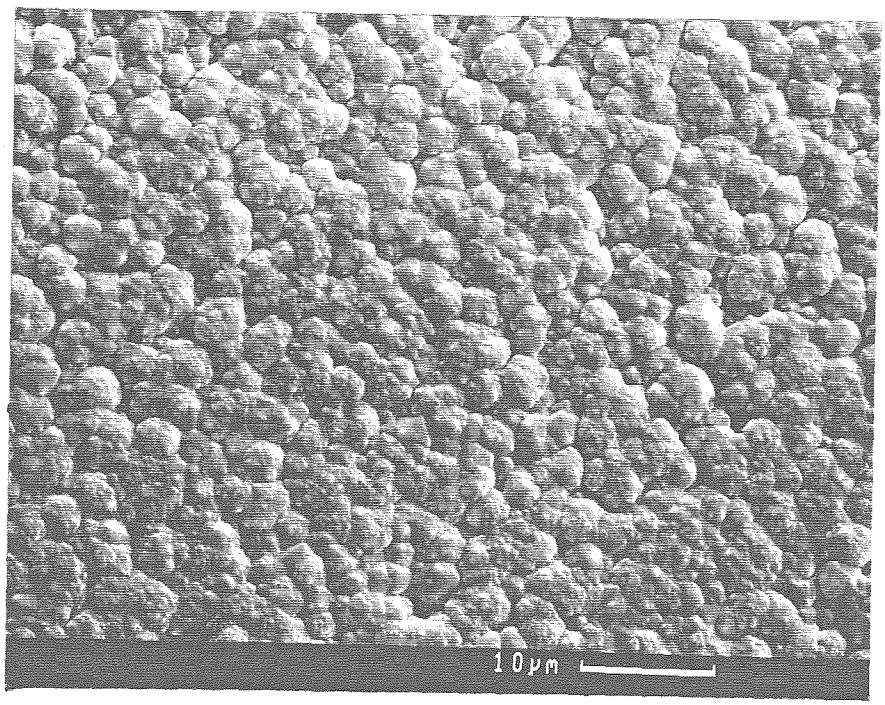

Figure 4.22: Particles near the center the of deposit.

of a growth condition, eventually the flame became too oxidizing for growth, and no deposit was observed. Decreasing R eventually reached a limit beyond which only non-diamond carbon was observed in the deposit.

Decreasing the value of T_S from that of a growth condition led to a more oxidizing environment at the surface, and no deposit was observed. In some cases diamond could be grown at the lower T_S if R was decreased or D_S increased.

Lastly, increasing burner to substrate distance D_S from that of a growth condition led eventually to a non-diamond carbon deposit. Success at growing diamond at the larger D_S could sometimes be achieved by lowering the substrate temperature or increasing the R value of the flame.

These trends are shown explicitly and analyzed in the following section.

4.4 Analysis

Using the model, some insight into the observed trends can be obtained. A typical growth condition for isolated diamond particles is as follows: $R = 1.34$, $T_S = 1233$ K, $D_S = 8$ mm, $P = 40$ Torr, and total flow rate = 0.159 slm/cm^2. This condition was run, after 20 minutes of nucleation enhancement (at R = 1.3, all other parameters the same), for 7 hours. Isolated, faceted diamond particles of 4 to 5 microns in diameter were observed on the pre-scratched silicon substrate. Particle radii thus grew at approximately 0.27 - 0.34 microns per hour, neglecting nucleation time.

The growth phase of this run was modeled using the flame code. The predicted

maximum gas phase temperature is 2085 K at 2.4 mm below the burner surface. The maximum strain rate is predicted to be 410 s^{-1} at 3.2 mm above the substrate. Plots of major stable species and key radical species with distance from the burner are shown in Figures 4.23 and 4.24.

The composition of the surface gas is given in Tables 4.2 and 4.3. All species predicted to be present at greater than 1 ppm are listed. The second column in these tables shows the equilibrium composition of an acetylene/oxygen mixture of $R = 1.34$ at 40 Torr and 1233 K. This column represents the composition which would be observed if the premixed gases were in chemical equilibrium at the substrate. The third column shows the molecular beam mass spectrometry measurements of Hsu [51] for a hot filament reactor under growth conditions. The final column represents the predicted growth environment for an atmospheric pressure torch reactor from the calculations of Goodwin [25].

Clearly the gases at the substrate surface in the flat flame reactor are far from chemical equilibrium. Only CO approaches its equilibrium value. Even the major species CO_2, H_2O, and H_2 are more than 25% from equilibrium. Similarly, the radical species are nearly all several orders of magnitude higher than their predicted equilibrium values.

In fact, few reactions are near partial equilibrium at the substrate surface. The following five fast reactions are often assumed to be in partial equilibrium in the post-flame zone of flat flames or, in the case of reaction 4.1, at the surface of a hot

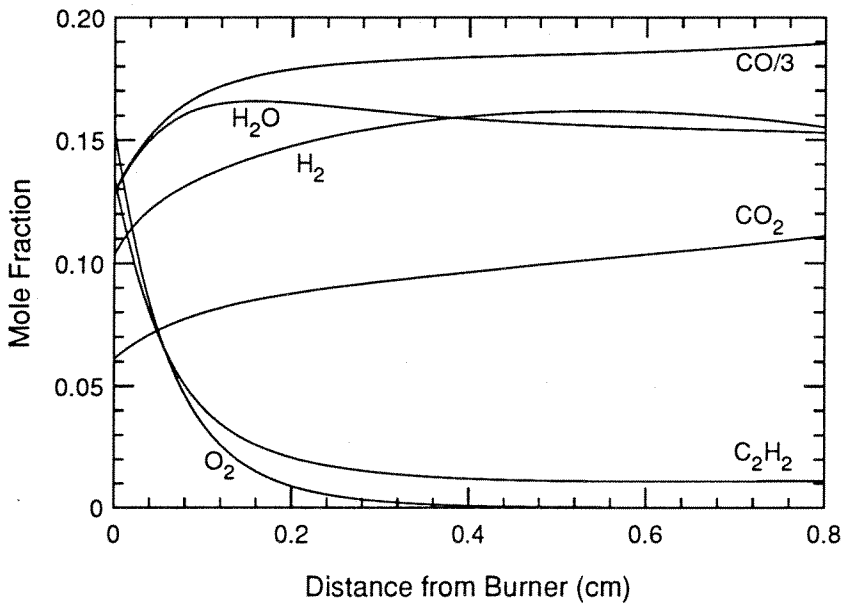

Figure 4.23: Major species spatial profiles in a deposition flame.

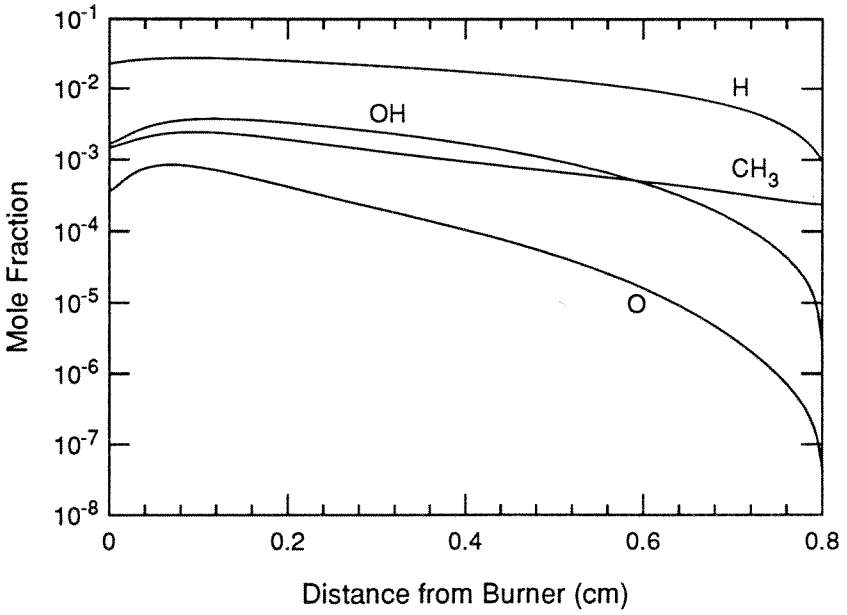

Figure 4.24: Key radical species spatial profiles in a deposition flame.

Species	Flat flame	Equilibrium	Hot filament	Torch
Major Stable Species				
CO	.57	.53	0	.59
CO_2	.11	.14	0	3.0e-7
H_2O	.15	.24	0	8.6e-7
H_2	.16	.24	.99	.22
C_2H_2	1.1e-2	9.7e-14	3.6e-3	2.6e-2
CH_4	4.5e-4	5.1e-8	3.9e-4	No data
O_2	5.5e-5	1.7e-15	0	1.5e-13
Major Radical Species				
H	9.3e-4	7.7e-7	2.3e-3	.16
CH_3	2.3e-4	3.7e-12	9.1e-5	3.2e-5
CH_2	1.1e-7	1.0e-17	No data	No data
C	6.5e-8	1.7e-24	No data	4.1e-4
C_2	4.8e-12	1.5e-30	No data	2.4e-4
C_2H	2.2e-8	4.4e-23	No data	1.4e-3
OH	3.1e-6	8.9e-15	0	2.4e-7
O	5.2e-8	2.9e-9	0	9.6e-8

Table 4.2: A comparison of predicted and observed diamond growth environments

Species	Flat flame	Equilibrium
Larger hydrocarbons etc.		
C_2H_3	3.4e-6	1.6e-19
C_2H_4	3.9e-5	7.9e-15
C_2H_6	6.8e-6	1.0e-17
C_3H_3	5.1e-6	7.3e-23
C_3H_2	1.0e-4	2.5e-24
C_4H_2	1.0e-4	1.9e-27
C_5H_2	9.0e-6	0.0
C_5H_3	2.7e-6	0.0
CH_2O	2.4e-6	6.9e-9
CH_2CO	7.0e-6	2.4e-13

Table 4.3: Some other model-predicted surface species mole fractions for a diamond depositing flame.

filament diamond CVD reactor:

$$CH_4 + H \leftrightarrow CH_3 + H_2 \tag{4.1}$$

$$OH + H_2 \leftrightarrow H_2O + H \tag{4.2}$$

$$O + H_2 \leftrightarrow OH + H \tag{4.3}$$

$$O_2 + H \leftrightarrow O + OH \tag{4.4}$$

$$CO + OH \leftrightarrow CO_2 + H \tag{4.5}$$

However, only reactions 4.1-4.3 are within 20% of partial equilibrium at 1 mm above the substrate, and only reaction 4.5 is within a factor of 2 of partial equilibrium at the surface. This is in sharp contrast to the atmospheric torch environment in which the mixture near the substrate is close to equilibrium and the high radical concentrations result from the high temperatures alone [15].

In general, there seem to be few similarities between the flat flame growth environment and the other two diamond CVD environments. The flat flame has 7 times the methyl mole fraction of the torch and 2.6 times that of the hot filament reactor. Also, the flat flame produces less than half as much H as the hot filament and more than 100 times less than the torch. Consequently, the flat flame has the lowest $[H]/[CH_3]$ ratio of all the methods at 4.0 compared to 25 for the hot filament and 5000 for the torch.

Also of importance is the fact that the flat flame produces 3 times the acetylene at the surface as the hot filament method and that it is the only method with an

appreciable amount of surface O_2 at 55 ppm. Since O_2 is known to etch diamond and non-diamond, it can play a role in deposition if present in large enough quantities.

Both atomic oxygen and hydroxl can also potentially etch diamond and non-diamond. In both flat flames and the atmospheric pressure torch, O mole fractions are predicted to be very small (less than 10^{-7}). OH in the atmospheric pressure torch is also present at less than 1 ppm. In a torch environment, diamond growth precursors are present in quantities on the order of 10 ppm. Thus, it is unlikely that OH or O plays a significant role in growth or etching in the torch flame. The same is true for O in the flat flame; however, OH may play a role since it is present at a few ppm in the flat flame. To do so, however, would require relatively fast carbon etching kinetics for OH.

Another important observation about the flat flame growth environment is that some important surface species concentrations are diffusion limited while others appear to be reaction rate limited. Figure 4.25 shows the predicted near surface mole fractions of H, CH_3, O_2, and OH. For this plot, the etch rate of diamond by OH was set to zero. The plot clearly shows that while [H] and [OH] are predicted to be diffusion limited, $[O_2]$ and $[CH_3]$ are not. Since the actual consumption rate of OH at the surface will be even higher due to etching reactions with sp^2 and sp^3 carbon, neglecting these etch rates does not affect the conclusion that surface [OH] is diffusion limited.

To understand why diamond grows in this particular area of parameter space,

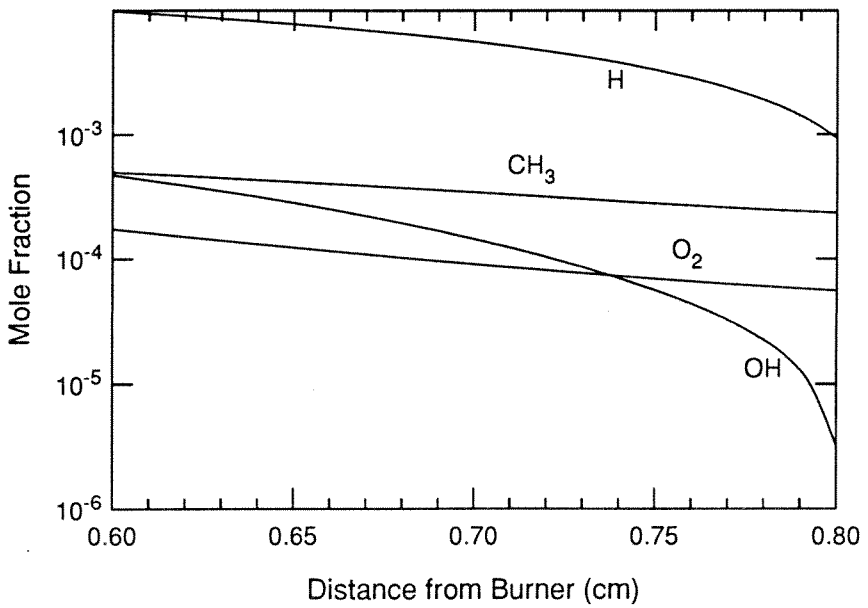

Figure 4.25: Spatial mole fraction profiles of some key species near the substrate. The substrate is at $D_S = 8$ mm.

three different case studies are presented. Each case looks at a particular series of experiments using the flame model to analyze the experimental results.

The analysis of the growth environment assumes that 4 basic deposition processes are occurring at the substrate surface. First, sp^3 carbon is being deposited from the gas phase, and it is also being etched back into the gas phase. The rate of deposition is referred to as G_D, and the rate of removal is referred to as E_D. Thus, the net rate of diamond growth is G_D - E_D. Similarly, the analysis assumes that sp^2 (non-diamond) carbon is being deposited and etched. Rates are given by G_{ND} and E_{ND}, respectively. The net rate of non-diamond carbon deposition is then G_{ND} - E_{ND}.

A negative net diamond deposition rate would be the rate at which a diamond

substrate is etched away. Of course, for our runs in which the substrate was silicon or molybdenum, the actual etch rate can be no larger than the growth rate since the surface diamond concentration goes to zero when $E_D = G_D$. In the analysis below, the calculated E_D is often the *potential* etch rate of diamond, i.e., as if the substrate were diamond. To distinguish from the actual E_D, potential etch rates will be denoted with a '$\star$.' The predicted potential etch rates can be related to the actual etch rates to first approximation by the site fraction, assuming first order kinetics and a reaction rate limited surface etchant concentration. For example, for the diamond etch rate on a surface with an sp^3 site fraction of N_3,

$$E_D = E_D^\star N_3. \tag{4.6}$$

For a diamond or mostly diamond deposit, $N_3 \approx 1$ and $E_D^\star \rightarrow E_D$.

The main etchant species capable of removing an sp^2 or sp^3 bonded carbon atom from the surface are assumed to be H, O_2, OH, and O. Certainly, other species (e.g., HO_2) can also remove surface carbon, but their concentrations are predicted to be extremely low near the surface, and so their contribution is neglected. Since the etch rate of diamond by H at deposition temperatures is probably extremely low, its contribution to the diamond etch rate is also neglected.

Since there are insufficient data to assemble a comprehensive mechanism for deposition of various types of sp^2 carbon, non-diamond deposition is not accounted for in the surface chemistry mechanism. Similarly, etching of non-diamond carbon by O, OH, and H is not explicitly included. For cases in which the surface site fraction of

sp^2 carbon is small (i.e., diamond depositing or etching conditions), neglecting these surface reactions probably has little effect on the near-surface species concentrations. For cases in which the deposit is predominantly sp^2 carbon, however, the effects will certainly be more appreciable. Thus, the surface chemistry will be most accurately predicted by the flame model at or near diamond growth conditions.

Case 1: The effect of oxygen

The fact that $[H]/[CH_3]$ is so low in the flat flame growth environment is surprising. Indeed, no other growth method reports diamond growth at such low $[H]/[CH_3]$ ratios. This case investigates how growth can be possible at these low ratios.

In terms of the analysis methodology stated above, in order to deposit pure diamond, at least three conditions must be met at the substrate surface. First, sufficient [H] and $[CH_3]$ must be present to produce a measurable growth rate. The Harris mechanism empirically establishes whether this condition is met or not. Though the prediction has a large uncertainty, a prediction of a few microns per hour of growth is a strong indication that significant [H] and $[CH_3]$ are available to produce an observable diamond deposit.

The second condition is that there must be sufficient surface concentrations of etchant species such that the potential etch rate of non-diamond ($E^{\star}_{ND}$) far exceeds the deposition rate of non-diamond (G_{ND}). The reason for this is given in the following simplified analysis. Assuming first order kinetics for all sp^2 etchant species, the net

rate of non-diamond deposition can be represented as:

$$G_{ND} - E_{ND} = G_{ND} - N_2 \sum_j k_j C_j = G_{ND} - N_2 E^{\star}_{ND} \tag{4.7}$$

In this equation, the sum is over the etchant species, k_j are the first order rate constants for etching of sp^2 carbon, C_j are the concentrations of the etchant species, and N_2 is the site fraction of sp^2 carbon. To achieve a deposit with a significant fraction of diamond, the etch rate of sp^2 carbon must equal the deposition rate of sp^2 carbon. This does not insure a pure diamond deposit, but does insure that the site fraction of sp^2 carbon (N_2) will be less than 1. Then, terms in equation (4.7) can be rearranged to obtain an equation for N_2.

$$N_2 = \frac{G_{ND}}{\sum_j k_j C_j} = \frac{G_{ND}}{E^{\star}_{ND}} \tag{4.8}$$

Thus, the steady state sp^2 site fraction is equal to the ratio of the non-diamond deposition rate to the potential non-diamond etch rate. In a typical diamond CVD reactor with a hydrogen/hydrocarbon environment, the non-diamond carbon deposition rate should scale with the gas phase hydrocarbon concentration. A rough approximation is that $G_{ND} \sim [CH_3]$. The potential non-diamond carbon etching rate is proportional to the surface H concentration. Then, since $[H]/[CH_3]$ is an indirect measure of $E^{\star}_{ND}/G_{ND}$ in cases where no oxygen is present, the $[H]/[CH_3]$ ratio provides some measure of the purity of the diamond deposit.

The third and final condition for diamond growth is that the etch rate of diamond must not exceed the growth rate of diamond. That is, $E_D/G_D < 1$.

Since it has been reported that oxygen addition to hot filament reactors can improve diamond quality [52], some speculation has arisen that O_2 (or OH or O) can play the same or similar role as H in diamond reactors. Certainly, in the removal of deposited sp^2 carbon, O_2 can help. O_2 would be extremely helpful if it could preferentially etch diamond. Some experimental data suggests that this may be the case, though O_2 is clearly not as effective as H at preferentially etching sp^2 carbon over sp^3 carbon. The extrapolated data from the experiments of Joshi, Nimmagada, and Herrington suggest a ratio of the etch rate by O_2 of graphite to diamond at 1223 K is only $\sim 1 - 3$ [53]. It is likely that the ratio is similar for other forms of sp^2 carbon. It is possible that the presence of O_2 at the surface could enable diamond growth with full non-diamond carbon removal at lower $[H]/[CH_3]$ ratios than observed in hydrogen/hydrocarbon environments. In a system characterized by a low value of $E^{\star}_{ND}/G_{ND}$, the addition of oxygen could push the ratio higher by increasing $E^{\star}_{ND}$. Then it is possible that growth can occur at low $[H]/[CH_3]$ ratios if there is sufficient [H] and $[CH_3]$ for growth, there is sufficient O_2 to etch excess non-diamond carbon, and $[O_2]$ is low enough such that $E_D/G_D < 1$.

To evaluate whether oxygen plays a significant role in the deposition process in our flames, the following two experiments were performed. In both cases, the run conditions were $R = 1.35$, $T_S = 1223$ K, total flow = 0.127 slm/cm^2, and $P = 35$ Torr. The first case was a diamond growth condition at $D_S = 7.5$ mm. In the second case, D_S was moved to 11.2 mm. Only non-diamond carbon was observed in the

deposit. The flame code predictions for the surface mole fractions of several key species are represented in Table 4.4. Predicted diamond growth rate (G_D) and etch rate due to O_2, OH, and O ($E^{\star}_{D,O_2}$, $E_{D,OH}$, and $E_{D,O}$), all in microns/hour, are also given.

The etch rates for O and OH represent the case in which each O or OH radical which strikes an active site etches a single carbon atom (as described in Chapter 3). This is likely an upper limit on potential etch rates, especially at lower deposition temperatures. The sticking probability of 1.0 is extremely high for even fast surface reactions. Also, other possible reactions of OH and O with active sites are possible. Adsorption followed by abstraction back into the gas phase *via* collision with a gas phase radical is a plausible reaction which would compete with the etching of diamond by OH and O. Since there are no available data for etch rates of diamond by OH and O, for the purposes of this study, only an upper and lower limit of $E_{D,OH}$ and $E_{D,O}$ can be predicted.

Compared to the 7.5 mm case the $D_S = 11.2$ mm case exhibits a larger [H]/[CH_3] ratio and, indeed, shows a greater ratio of [H] to [C_2H_2] or any other major hydrocarbon species at the surface. If atomic H was solely responsible for the removal of sp^2 carbon, then higher quality diamond, albeit at a lower growth rate, would be expected in the second case. This would result from an increased sp^2 potential etch rate combined with a decreased rate of deposition of both diamond and non-diamond carbon.

D_S	H	CH_3	C_2H_2	O_2	OH
7.5 mm	9.8e-4	4.4e-4	1.8e-2	5.3e-4	3.7e-6
11.2 mm	6.5e-4	1.9e-4	1.1e-2	1.5e-5	1.7e-6
D_S	$\frac{H}{CH_3}$	G_D	$E^{\star}_{D,O_2}$	$E_{D,OH}$	$E_{D,O}$
7.5 mm	2.2	3.0	2.6	0.96	.035
11.2 mm	3.5	0.85	0.31	0.45	.0043

Table 4.4: Predicted surface species mole fractions and diamond growth and etch rates (in μm/hr) for two cases with different D_S.

However, such is not the case. Non-diamond carbon predominates at the higher D_S value. For the case of the larger D_S, the surface hydrocarbon concentrations have decreased by at least 30%. Thus, G_{ND} is expected to decrease by at least 30%. H has also decreased by about 30%, and so its potential etch rate should also decay by the same amount, assuming first-order kinetics for etching of sp^3 carbon by H. Additionally, since the appearance of non-diamond carbon at only the larger D_S value dictates that the non-diamond site fraction at the substrate has increased, the actual etch rate of non-diamond carbon by H has probably decreased by a percentage less than the percentage decrease in [H]. Thus, while the experiments indicate that the difference G_{ND} - E_{ND} went from negative to positive with the increase in D_S, the difference G_{ND} - $E_{ND,H}$ could not have changed sign. Clearly, there must be an additional important term in E_{ND} which allows G_{ND} - E_{ND} to be negative for the

smaller D_S and thus enables diamond growth. In the case in which diamond growth was observed, the large predicted etch rate of diamond by O_2 suggests that O_2 is also responsible for a sizable non-diamond etch potential. Therefore, it is quite likely that E_{ND,O_2} is the critical component of E_{ND} which decides whether or not the deposit will be pure diamond.

It is also notable that the predicted etch rate of diamond under growth conditions is more than 80% of the predicted diamond growth rate. This suggests that, in this region of parameter space with very low $[H]/[CH_3]$ ratios, conditions which result in a primarily diamond deposit require O_2 levels which result in a significant amount of the diamond deposit being etched away with the non-diamond. This is not surprising. If indeed O_2 is required to etch a large amount of non-diamond carbon, its limited preferential etching ratio implies that a significant amount of diamond will also be removed. Thus, while O_2 may assist in the etching portion of the diamond growth process, it is clearly a less effective substitute for H.

OH may also contribute by etching non-diamond. The model predicts that if OH were capable of etching a single carbon atom each time one hit an active surface site, then the etch rate of diamond by OH ($E_{D,OH}$) would be nearly 1 μm/hr, or about 40% of $E^{\star}_{D,O_2}$. At the larger D_S, $E_{D,OH}$ also drops, but only by a factor of two. If the ratio $E_{ND,OH}/E_{D,OH}$ is much larger than that of O_2, then it is possible that the decrease in surface OH is at least partially responsible for the change in deposition conditions with increasing D_S. However, additional experimental data on the etching

rates of sp^2 and sp^3 carbon by OH are required in order to more accurately assess the role of OH.

Case 2: The effect of substrate temperature

The effect of a change in substrate temperature (T_S) is considered in Case 2. For this case, two identical runs were performed with the only difference being T_S. For both runs, $R = 1.3$, $D_S = 7.5$, $P = 35$ Torr, and the total flow rate is 0.127 slm/cm^2. In the first run, $T_S = 1223$ K, and the result is isolated diamond deposit with some secondary nucleation. This is a slightly rich growth condition. In the second run, $T_S = 1123$ K, and there is no deposit after 5 hours of run time.

In a similar experiment a diamond growth condition was used to deposit isolated diamond at 1223 K, and then T_S was lowered to $\sim$ 1148 K. The deposit was etched away, leaving only some small sections of the substrate with regions of isolated, heavily etched diamond. Indeed, the growth surface chemistry is changing from growth to oxidation with the decrease in substrate temperature. For these runs then, G_D - E_D is changing from positive to negative with the decrease in T_S. This change was observed in several similar runs.

The model predictions of the surface mole fractions of key species for the two runs are given in Table 4.5. There are only small predicted changes of less than 20% in H, CH_3, C_2H_2, and [H]/[CH_3]. Surface O_2 increases 25% due to a decreased diamond etch rate, and OH is predicted to decay by 20%. Though there is more O_2

T_S	H	CH_3	C_2H_2	O_2	OH
1228 K	9.2e-4	5.0e-4	2.4e-2	4.0e-4	3.1e-6
1123 K	9.7e-4	4.7e-4	2.4e-2	5.1e-4	2.2e-6
T_S	$\frac{H}{CH_3}$	G_D	$E^{\star}_{D,O_2}$	$E_{D,OH}$	$E_{D,O}$
1228 K	1.8	3.2	2.0	0.81	.020
1123 K	2.1	3.0	0.30	0.47	.018

Table 4.5: Predicted species concentrations and growth and etch rates (in μm/hr) for two cases with different T_S.

present at the surface, all significant diamond etch rates have dropped, and thus it appears as though the environment has become more conducive to carbon deposition. The experimental results dictate just the opposite. The observed difference in results must then be accounted for by considering the temperature dependence of surface processes.

At the lower temperature, for a given chemical environment, the diamond growth rate will be lower. This effect is not included in the growth mechanism used to predicted growth rates (the mechanism is designed to match experimental results at 1200 K). Thus, the diamond growth rate predicted for the two cases is roughly the same. Assuming an activation energy of 23 kcal/mole [54], the mechanism will predict a growth rate at the lower T_S that is a factor of 2 too large. Thus, a more accurate growth rate prediction at 1123 K is $\sim$1.5 μm/hr.

The etch rate of diamond by O_2 and OH will also decrease. The temperature dependence of the O_2 etch rate is included in E_D, and, with an activation energy of 54.7 kcal/mole, it is predicted to drop by a factor of 6 over this temperature range. The predicted etch rates for OH and O have no temperature dependence in their etching reactions, though it is likely that the etch rates are temperature dependent. The sticking probability for both species for reaction with an active site on the surface to etch diamond is set to a constant value (1.0). Consequently, while $E_{D,OH}$ and $E_{D,O}$ are overpredicted for all conditions, the amount of overprediction increases with decreasing T_S, assuming a positive activation energy for these etching reactions.

If there is a balance between growth of diamond and etching by O_2 and OH, as we suspect is the case, then this balance will be shifted upon lowering T_S by the decaying growth and etch rates — unless the difference G_D - E_D remains constant. Since the lower temperature yields no diamond, we can assume that G_D - E_D is not constant. For the low temperature case, we can say that G_D - $E_D \leq \epsilon$. We can estimate an upper limit for ϵ by assuming that diamond particles exist on the substrate at just below the resolving power of the microscope. In that case, ϵ could be no larger that 0.02 μm/hr for T = 1123 K, whereas G_D - $E_D \approx .47$ μm/hr at T = 1223 K as measured experimentally. The data suggest clearly that E_D has decayed slower than G_D over this temperature regime.

Experimental rate data suggest that additional factors other than the predicted growth rate of diamond and potential etch rate of diamond by O_2 must be in-

volved. Previous experiments based solely on growth rate and substrate temperature correlations have placed the activation energy for diamond growth in a hydrogen/hydrocarbon environment at 8–25 kcal/mole [54, 55]. The measured activation energies for O_2 oxidation of diamond range from 36–55 kcal/mole [44]. Based on these values alone, G_D should decay slower than E_{D,O_2}.

In this case, OH may play the key role in the results. Surface OH has dropped by less than 30% with the change in T_S. If the activation energy for sp^2 and sp^3 carbon deposition are both substantially larger than the activation energy for etching of sp^2 carbon by OH, then OH might be capable of removing a greater fraction of the deposited sp^2 and sp^3 carbon at the lower temperature.

Still the predicted growth rate far exceeds even the sum of the maximum etch rate of diamond by OH and the predicted etch rate of diamond by O_2, while at the higher T_S case, G_D - E_D = 0.4 – 1.2 μm/hr which compares well with the observed 0.47 μm/hr. Thus, it appears as if the model does not predict the temperature dependence of the growth and etching processes very well. The temperature dependence of E_{D,O_2} could easily have been overestimated. The chosen activation energy (54.7 kcal/mol) is at the high end of the experimentally observed range, and the activation energy has been observed to be a strong function of the quality of diamond deposit [44]. Considering this possibility and the factor of 2 uncertainty in predicted growth, it is conceivable that $E_{D,O_2} + E_{D,OH}$ could be larger than G_D at the lower T_S. For this to be the case, however, would require a substantial contribution to the overall diamond

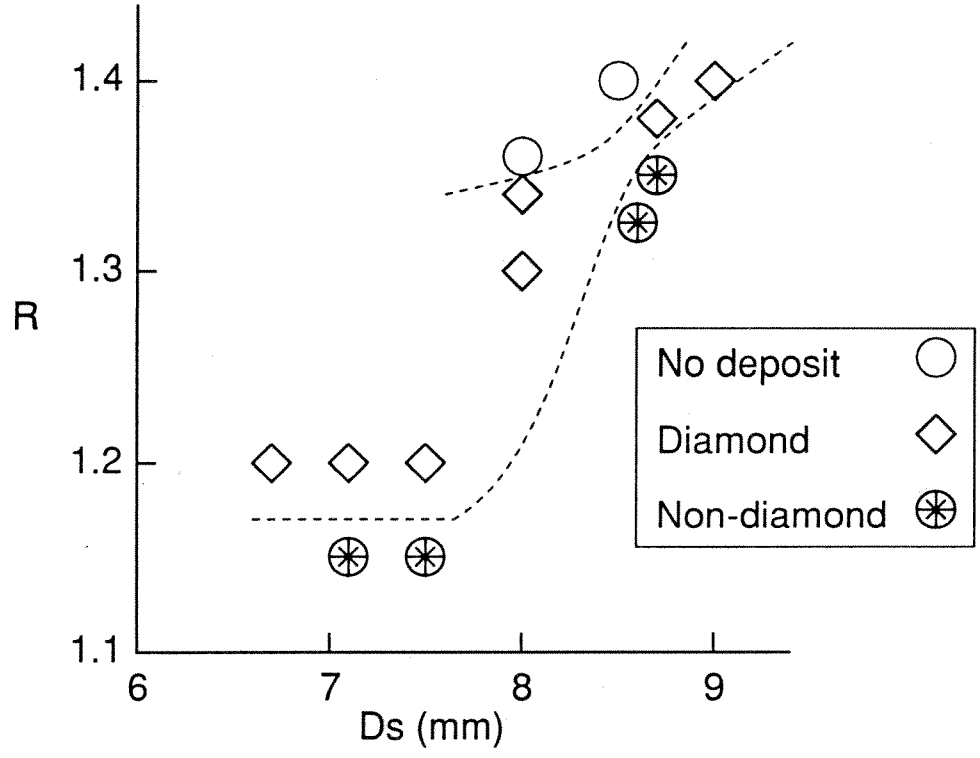

Figure 4.26: Deposition results for several growth runs.

etch rate by OH.

Case 3: The effect of oxygen to acetylene ratio

The third case examines why this particular range of R (1.2 – 1.4) is responsible for diamond growth. Compared to atmospheric pressure torches which deposit best below $R = 1$, low pressure flat flames deposit diamond only under much leaner conditions. To investigate why this is, we look at some data from a series of runs. Figure 4.26 shows a plot of runs at 40 Torr and T_S= 1203–1253 K at 0.159 slm/cm^2.

The dashed lines represent roughly the boundaries of etching, diamond growth,

and non-diamond growth. To analyze the effect of varying the flame stoichiometry, several flames at D_S = 8 mm were modeled for values of R ranging from 1.15 to 1.4. According to the growth run data, this range should just span the three regions. Clearly, R = 1.15 is too rich, R= 1.4 is too lean, and somewhere in between, faceted diamond will grow. The predictions of the model are shown in Figures 4.27 and 4.28. Figure 4.29 shows the variation in predicted growth and etch rates.

The predicted growth environments for the two limiting cases and a likely diamond growth case (R = 1.32) are presented in Table 4.6. The model predictions show that the growth environment is becoming more oxidizing with increasing R. H, OH, O_2 are increasing and all hydrocarbons are decreasing in concentration. However, the change in [H], [CH_3], and [OH] is small compared to the changes observed in [O_2]. For example, in moving from R = 1.15 to R = 1.4, H has increased 49%, OH is up by a factor of 2.4, CH_3 is down by a factor of 1.6. [H]/[CH_3] goes from 2.6 to 6.1. The largest differences are seen in O_2 and C_2H_2. O_2 shows the greatest change over the range, increasing by a factor of 31, and C_2H_2 shows a decrease by a factor of 12. The dramatic rise in O_2 as the environment goes from a non-diamond to a diamond depositing condition suggests again that O_2 plays the key role here.

The Harris mechanism prediction suggests that enough [H] and [CH_3] are present for diamond growth at all R values. However, a high quality diamond deposit only appears after the diamond etch rate of O_2 has risen nearly an order of magnitude to a value which represents a significant fraction of the diamond deposition rate. Since

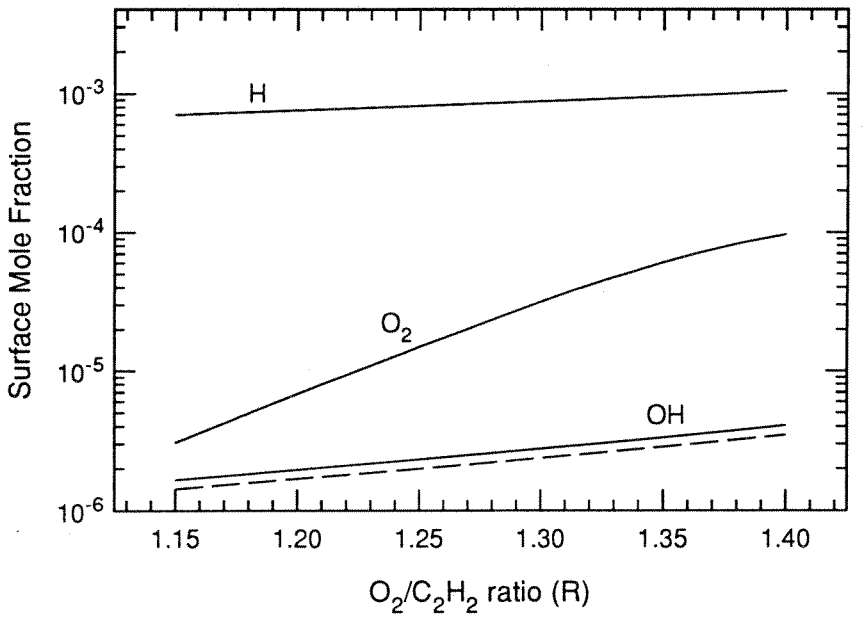

Figure 4.27: Model predictions for etchant species in the run series of Case 3. The dashed line represents the case in which diamond etching by OH is included.

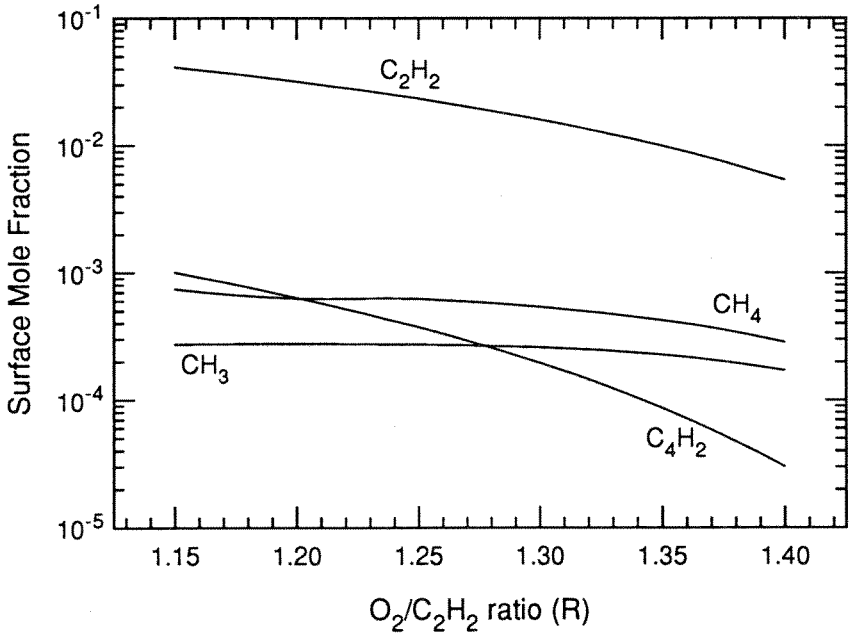

Figure 4.28: Model predictions for hydrocarbon species in the run series of Case 3.

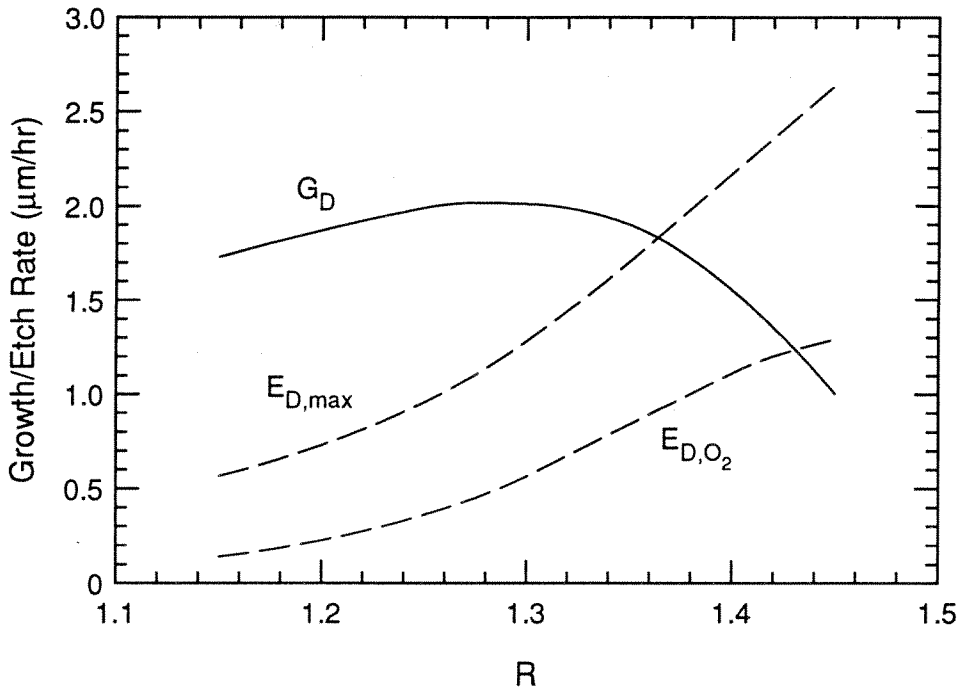

Figure 4.29: Predicted growth and etch rates vs. R in the run series of Case 3.

the values of [H]/[CH_3] (< 3 at optimal diamond conditions) suggest that additional help in etching non-diamond carbon is required for full non-diamond carbon removal, it is probable that the region of R in which diamond grows is dictated by the etch rate of non-diamond carbon by O_2 and OH. The lower R boundary is less sharply defined but likely corresponds to the region in which $E^{\star}_{ND}$ is large enough to produce a $E^{\star}_{ND}/G_{ND}$ ratio which precludes a large sp^2 component in the deposit.

Again, it is possible that OH, in addition to O_2, is etching significant amounts of both diamond and non-diamond under deposition conditions. The maximum predicted etch rate of diamond by OH under diamond growth conditions is roughly equal to the etch rate of diamond by O_2. Also, $E_{D,OH}$ increases significantly over the range

R	H	CH_3	C_2H_2	O_2	OH
1.15	7.0e-3	2.7e-4	4.1e-2	3.1e-6	1.4e-6
1.32	9.2e-4	2.4e-4	1.2e-2	4.9e-5	2.7e-6
1.40	1.0e-2	1.7e-4	5.4e-3	9.6e-5	3.5e-6
R	H/CH_3	G_D	$E^{\star}_{D,O_2}$	$E_{D,OH}$	$E_{D,O}$
1.15	2.6	1.7	0.14	0.43	.0011
1.32	3.8	1.9	0.74	0.80	.011
1.40	6.1	1.6	1.1	1.1	.032

Table 4.6: Predicted surface mole fractions of several key species and diamond growth and etch rates (in μm/hr) for a cases characterized by a non-diamond deposit ($R = 1.15$), a diamond deposit ($R = 1.32$), and no deposit ($R = 1.40$).

of R (by a factor of 2.6), though not by as much as $E^{\star}_{D,O_2}$, which increases by a factor of 7.9. Thus, while it is probable that both OH and O_2 contribute to the non-diamond etching process, the contribution of E_{ND,O_2} to E_{ND} is probably larger and is definitely more sensitive to R than the contribution of $E_{ND,OH}$.

The upper limit on diamond growth near $R = 1.4$ almost certainly corresponds to the point at which $E_D > G_D$. Figure 4.29 suggests that this is the case. If only etching by O_2 is considered, E_D exceeds G_D at $R \approx 1.43$. Adding the maximum contribution to etching by OH and O brings the crossover point to $R \approx 1.36$. Considering the factor

of two uncertainties in both G_D and E_{D,O_2}, the experimentally observed crossover at $R \approx 1.35$ is within the uncertainties of the crossover points of both etching curves. Given the large uncertainties in $E_{D,OH}$ and E_{D,O_2} these data cannot be used to infer the relative magnitude of each species' contribution to the overall diamond etch rate.

Further Analysis

The fact that the environment changes from a diamond growth environment to a non-diamond deposition environment as surface coverage increases must be explained in terms of surface chemistry. Since the initial surface is mostly silicon (or molybdenum) the surface kinetics are dominated by recombination and reaction rates of radicals on a silicon surface. Thus the gas phase composition near the surface is controlled by silicon surface kinetics. As the deposition process progresses and surface coverage by diamond increases, the near-surface gas phase composition becomes increasingly affected by diamond surface kinetics. If the two surfaces have significantly different kinetics, the change in near-surface gas phase composition can be appreciable.

Significant differences certainly exist in the surface kinetics of diamond and silicon. A simple example is reaction with oxygen. In the case of silicon, O_2 reacts to create a surface oxide layer of SiO_2 and can also create gas phase SiO through a series of reactions. When reacting with a diamond surface, O_2 predominantly etches diamond into the gas phase in the form of CO and CO_2. O_2 might possibly be able to bind

active surface sites but will not precipitate out a solid surface oxide as the case of silicon. Thus, it is expected that the rates for O_2 destruction at the surface will thus vary significantly between silicon and diamond. In addition, a second solid phase, SiO_2, will be present at the silicon surface in an oxygen environment.

In a pure hydrogen atmosphere silicon, like diamond, is hydrogen terminated at the surface. Recent surface kinetic data for hydrogen adsorption on silicon and for deuterium abstraction by hydrogen [56] allow for calculation of a reaction probability for recombination of atomic hydrogen via hydrogen abstraction from a silicon surface. The suggested reaction probability on silicon for deposition conditions is equal to or higher than the reaction probability on diamond. With this alone, the same or less H at the silicon surface would be expected. However, with the presence of oxygen, some SiO_2 will be formed at the surface, decreasing the density of hydrogen terminated sites. Extrapolated data from Green *et al.* [57] and Smith [58] suggest that at deposition temperatures, the recombination probability for H on SiO_2 may be well below the 0.13 value observed experimentally [42] at 1200 K for diamond.

If sufficient surface coverage by SiO_2 is present, then the overall H recombination rate will be lower for a silicon surface than for a diamond surface in the deposition environment. This would result in a comparatively higher surface H mole fraction and a higher $[H]/[CH_3]$ ratio. The additional H would increase the diamond growth rate as well as the etch rate of non-diamond carbon, without significant increases in the etch rate of diamond. Effectively, the best diamond growth conditions would be

observed early in the run when the diamond coverage is too small to appreciably affect the surface kinetics. Then, as diamond coverage increases, the H recombination rate would increase and the surface H mole fraction would decrease. With a reduction in H, the diamond growth rate would decrease as would the etch rate of non-diamond carbon by H. This would shift the ratio $E^{\star}_{ND}/G_{ND}$ to lower values, resulting in a poor quality deposit. This is likely the case in our flames which grow diamond isolated particles but do not grow films.

The analysis above would then suggest that switching conditions to include more O_2 or OH (perhaps by increasing R) as the film becomes continuous might allow diamond growth to continue. This increase in O_2 or OH would increase $E^{\star}_{ND}/G_{ND}$ back to values which would provide high quality diamond. The failure of many attempts to do exactly this suggests that this region of parameter space may not be capable of depositing diamond on a diamond surface no matter how much O_2 or OH is present. Reasons for this inability to grow diamond on diamond are suggested in the following analysis.

The key ratio in determining whether oxygen-assisted diamond growth is possible at a specific value of $[H]/[CH_3]$ is the deposition ratio D_r, which is defined as follows:

$$D_r = \frac{G_D}{G_{ND} - E_{ND,H}} \tag{4.9}$$

The parameter D_r can be viewed as the ratio of deposition rates of diamond and non-diamond in the absence of O_2 and OH. The denominator is the rate of non-diamond deposition that must be matched by a non-diamond etch rate due to O_2

and OH in order to allow the deposit to have some diamond component. The ratio then is the rate of diamond deposition to the required rate of non-diamond removal by O_2 and OH. The reason that this is an important parameter is that, to achieve a certain non-diamond removal rate, O_2 and/or OH concentrations must be a certain value. If these concentrations are high enough to produce a diamond etch rate which exceeds the growth rate, all non-diamond will certainly be removed, but all diamond will be removed as well. This suggests that there is a critical deposition ratio $D_{r,crit}$ which dictates whether addition of oxygen will allow a diamond film to be deposited or whether it will necessarily remove all deposited diamond leaving no deposit.

The following analysis suggests an approximate relation for $D_{r,crit}$. To begin, first order reaction kinetics are assumed for all deposition and etching reactions. G_{ND} is likely some function of residual hydrocarbons in the gas phase. To first approximation, it is assumed that $G_{ND} \propto [CH_3]$ and that the rate is the same for deposition on sp^2 sites and sp^3 sites. Also, for low concentrations of H, G_D has been predicted to be proportional to $[H][CH_3]$ [12]. Lastly, only O_2 is considered as an additional etchant species, though the analysis could be generalized to include OH without affecting the conclusions significantly. Given these assumptions, the following equations for G_D and G_{ND} in terms of the site fractions of sp^2 carbon (N_2) and sp^3 carbon (N_3) and the first order rate constants k_1-k_5 can be written:

$$G_{ND} - E_{ND} = k_1[CH_3] - (k_2[H] + k_3[O_2])N_2 \tag{4.10}$$

$$G_D - E_D = k_4[H][CH_3]N_3 - k_5[O_2]N_3 \tag{4.11}$$

Assuming that experimental conditions are chosen such that there is enough $[O_2]$ to make $E_{ND} = G_{ND}$, a relation for N_2 can be obtained as before.

$$N_2 = \frac{k_1[CH_3]}{k_2[H] + k_3[O_2]} = G_{ND}/E^{\star}_{ND} \tag{4.12}$$

The deposition ratio can be expressed in terms of the assumed rates as

$$D_r = \frac{k_4[H][CH_3]N_3}{k_1[CH_3] - k_2[H]N_2}. \tag{4.13}$$

In order to have a net diamond deposition rate, G_D must be greater than E_D. This constraint implies that the minimum possible value of D_r corresponds to the condition $G_D = E_D$. Replacing $k_4[H][CH_3]$ in equation (4.13) by $k_5[O_2]N_3$ yields an expression for $D_{r,crit}$.

$$D_{r,crit} = \frac{k_5[O_2]N_3}{k_1[CH_3] - k_2[H]N_2} \tag{4.14}$$

Inserting the relation of equation (4.12) and noting that $N_2 + N_3 = 1$, the following equation is obtained:

$$D_{r,crit} = \frac{k_5}{k_3}\left(\frac{k_2[H] + k_3[O_2]}{k_1[CH_3]} - 1\right) = \frac{k_5}{k_3}\left(\frac{E^{\star}_{ND}}{G_{ND}} - 1\right) \tag{4.15}$$

The ratio k_5/k_3 is the preferential etch ratio of O_2 ($E^{\star}_{D,O_2}/E^{\star}_{ND,O_2}$). The equation for $D_{r,crit}$ suggests that the critical deposition ratio depends also on the quality of film desired. A higher purity film demands a higher deposition ratio. To achieve a film which is predominantly diamond (i.e. $N_3 > 0.5$), the relation for $D_{r,crit}$ becomes simply:

$$D_{r,crit} = \frac{E^{\star}_{D,O_2}}{E^{\star}_{ND,O_2}} \tag{4.16}$$

In a region of parameter space in which $D_r \leq D_{r,crit}$, no predominantly diamond films can be deposited. In that case, increasing mole fraction of etchant species to the point at which all necessary non-diamond is removed would imply removal of all deposited diamond as well. In such a region, only predominantly non-diamond film deposition or no deposition is possible.

The deposition ratio has a strong dependence on [H]. From equation (4.13), the relation for N_2 can be inserted to yield:

$$D_r = \frac{k_4[H]N_3}{k_1 - \frac{k_1 k_2[H]}{k_2[H]+k_3[O_2]}} \tag{4.17}$$

From this relation, it is apparent that D_r is a monotonically increasing function of [H].

Because D_r increases with [H], it is probable that D_r decreases with surface diamond coverage, since the more efficient recombination of H on diamond decreases surface [H]. If D_r drops below its critical value before diamond coverage is complete, diamond deposition cannot continue at that condition nor any condition which does not increase D_r. This would explain the inability to grow continuous films by cycling of R as well since removal of all deposited non-diamond by an etch cycle would imply removal of all deposited diamond as well.

This variation in surface kinetics would also explain the difference in deposit quality with distance from the edge of a deposit region. Near the deposit edge, the local surface site fraction of diamond is roughly one-half (i.e., the same as that of silicon). Near-surface species concentrations are influenced by both surface reactions on dia-

mond and surface reactions on silicon. [H] is probably largest at this location in the deposit, and, if so, the deposition ratio is also at a maximum. As we move inward, the surface kinetics are controlled to a greater extent by the deposit material (diamond and non-diamond). In the gas phase above the deposit then, we have reduced [H] due to the potentially larger H recombination probability on diamond. As we move further in, eventually D_r drops below $D_{r,crit}$, and the deposit is non-diamond.

Since the model used to analyze the growth runs uses a surface chemical mechanism for diamond, the predictions of the model are strictly applicable only for the case of continuous or semi-continuous films. Thus the predicted growth conditions (i.e., those conditions which grew isolated diamond crystals) are conditions closest to diamond film growth conditions, but do not represent conditions in which diamond films would be deposited. If indeed the change in surface kinetics is the reason for the inability to grow continuous films, then it is likely that the predicted near-surface environment for a case in which isolated diamond was deposited represents a case in which D_r is only slightly less than $D_{r,crit}$.

To increase D_r in a case in which $D_r < D_{r,crit}$ and the surface is non-diamond, some simple relations suggest that the key parameters are [H] and [H]/[CH_3]. Using the same reactions as before for a small N_3 and $N_2 \approx 1$, equation (4.13) yields

$$D_r = \frac{k_4[H]N_3}{k_1 - k_2\frac{[H]}{[CH_3]}}. \tag{4.18}$$

According to this relation, we would expect the deposition ratio to increase with both [H] and [H]/[CH_3]. This suggests that to obtain continuous films on diamond,

either or both of these quantities would need to be increased over those values in the parameter space around previous isolated diamond particle growth conditions. It would still also be essential to be able to vary the additional etch rate of non-diamond at the surface by varying surface $[O_2]$ or [OH]. This could likely be accomplished relatively independently of [H] and $[H]/[CH_3]$ by small variations of R or D_S.

4.5 Summary

The analysis of the experimental results has suggested that O_2 and possibly OH play an instrumental role in the diamond deposition process by its etching of non-diamond carbon. Clearly, at these low $[H]/[CH_3]$ ratios, growth of high quality diamond is made possible by the presense of O_2 and/or OH which can, in some cases, etch away the excess non-diamond carbon which H cannot etch.

The region of parameter space in which diamond grows appears to be determined by a balance between growth of diamond and non-diamond and etching of non-diamond. Since [H] and $[CH_3]$ vary by much less in the examined region of the parameter space, $[O_2]$ and the non-diamond etch rate associated with $[O_2]$ are the most crucial factors in determining whether a particular position in the parameter space will grow diamond.

Flames richer than our growth conditions have sufficient [H] and $[CH_3]$ to grow diamond, but they lack enough [H], $[O_2]$, or [OH] to remove the non-diamond which is deposited. Making the flame leaner can, in some cases, increase $[O_2]$ to a point at

which it can etch the excess non-diamond, leaving a net diamond deposit behind.

Moving to still leaner flames simply increases the O_2 concentration to the point at which the etch rate of diamond exceeds the growth rate. The point at which this happens defines the upper boundary for diamond growth.

It is likely that the recombination kinetics of H on silicon allow for diamond growth by increasing D_r through an increased surface H mole fraction. Similarly, the increased recombination efficiency of H on diamond prevents D_r from exceeding its critical value in the regions of parameter space in which there are appropriate amounts of O_2 to remove all deposited non-diamond. Increasing D_r beyond its critical value could be accomplished by increasing surface [H] or [H]/[CH_3].

Growth of diamond films could likely be obtained by locating a region in parameter space in which $D_r > D_{r,crit}$ over a wide range of surface [O_2] and [OH]. Then, at some point in that region, all conditions for diamond film growth could be met.

Chapter 5

Diamond Films in Acetylene/Oxygen Flames

5.1 Introduction

Since most potential applications for CVD diamond require continuous films, low pressure flat flames can only be considered a viable alternative for CVD diamond synthesis if film growth conditions are achievable. The previous experiments in low pressure flat flames all failed to find such conditions in the prescribed region of parameter space, which was limited by burner design. Though no film growth conditions were found, some conditions did yield isolated diamond crystals, suggesting that such conditions were near film growth conditions but that, with a diamond surface controlling the surface kinetics, the deposition ratio was below the critical value in the probed region of parameter space.

To obtain diamond growth on a diamond surface requires that the deposition ratio be increased above its critical value. Relations from Chapter 4 suggest that, to increase the deposition ratio, the quantities [H] and [H]/[CH_3] must be increased.

Modeling results suggest that increasing the specific flow rate results in a thinner concentration boundary layer at the substrate surface. Since the concentration of H at the surface is predicted to be diffusion limited, thinning the boundary layer would result in increased transport to the surface and thus increased surface [H]. The higher flow rates would also yield higher gas phase temperatures which would lead to increases in [H] and [OH] at the flame front. In addition, the faster kinetics in the hotter flame lead to more complete combustion (i.e., a reduction in C_2H_2, CH_3, and other residual hydrocarbons at the substrate surface) while still maintaining high [H]

levels which persist because of the long time scale for ternary recombination. Thus, the [H]/[CH_3] ratio could be increased as well.

Modeling results project that by increasing specific flow rates by an order of magnitude, surface [H] could be doubled and [H]/[CH_3] could be tripled (compared with a low flow rate isolated diamond particle growth condition) with sufficient [H] and [CH_3] present for diamond growth and etch rates due to O_2 anywhere from approximately zero to several microns per hour depending on R.

Thus, the experimental setup was appropriately modified to work in this regime of flow rates. Several growth conditions were isolated in which faceted diamond films were grown. The films were verified as good quality diamond by Raman spectroscopy. The uniformity of film thickness was quantified by scanning electron microscopy and found to be excellent. The flame model was then used to analyze the growth conditions and compare them with the growth conditions at low specific flow rates.

5.2 Experimental

Burner

For the higher specific flow rates using the original burner, the burner surface temperatures exceed the design values. Thus, a new burner had to be fabricated. The burner surface diameter was reduced from 6 cm to 4 cm to increase specific flow rates for a given total flow rate, and the heat transfer from the burner face to

the cooling core was increased by changing the wall material from stainless steel to copper, which has a much higher thermal conductivity. Details of the burner design are given in Appendix B.

Substrate Cooling

The heat flux to the substrate surface was also dramatically increased. To minimize temperature non-uniformities, a thick (6 mm) molybdenum plate was used as a substrate. Under steady state conditions, the substrate reached a temperature of 1073 – 1123 K, depending on substrate geometry. However, early in the run before a deposit was formed, the emissivity of the polished substrate surface was considerably higher than the surface emissivity of a carbon deposit. The net result was decreased radiative heat transfer and a higher T_S early in the run.

To avoid this temperature overshoot, cooling was added to the system to maintain a constant substrate temperature for the duration of the run. Figure 5.1 is a schematic of the assembly for cooling the substrate. The cooling system consisted of a copper block with a central jet of helium. The block was placed below and parallel to the bottom side of the substrate. A helium flow was maintained at a flow rate sufficient for helium to be the predominant species in the gap between cooling core and the substrate bottom. The cooling rate was controlled by varying the gap width. Smaller gaps widths provide steeper gradients and, thus, more heat transfer. When the substrate reached a steady state temperature, the helium jet was turned off.

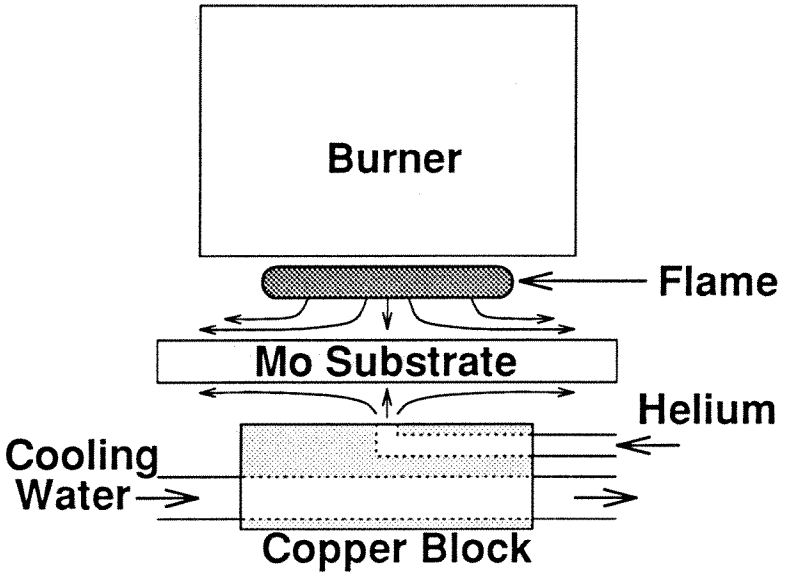

Figure 5.1: The substrate cooling system.

Substrate Preparation

Molybdenum substrates were prepared by sanding the surface to 500 grit. The surface was then scratched by a mixture of 0.5 micron and 15–25 micron sized diamond particles in a lapping paste. The grit and paste were removed by rinsing with acetone.

A few runs were performed with a segment of a silicon wafer placed on top of the molybdenum plate. The thermal contact to the molybdenum was assisted by a thin layer of copper grease between the lower surface of the silicon and the upper surface of the molybdenum plate. In one of the initial experiments with silicon, several different substrate preparations were used including: no surface pretreatment, scratching with 0.5 micron grit in paste, scratching with both 0.5 and 15-25 micron grit in paste, and scribing several scratches with a diamond scribe. The highest uniform nucleation densities were obtained using the mix of diamond grit in paste. Thus, all subsequent

runs were performed with this pretreatment.

Temperature Measurements

For all substrates, the two-color pyrometer was used to measure substrate temperatures. In the case of silicon, the pyrometer was operated at a grazing angle (70 – 80 degrees from normal) of incidence. For molybdenum substrates, the pyrometer was operated at normal incidence and was used to determine the temperature of the substrate edge. These measurements typically agree with thermocouple measurements taken near the substrate center to within 50 K.

5.3 Results

Three diamond film growth conditions were isolated. The three conditions are listed in table 5.1. On silicon, only sections of continuous film of $\sim$500 μm^2 were observed. This was likely due to the generally lower nucleation density on silicon and the large temperature non-uniformity ($>$ 100 K from center to edge of substrate) on the growth surface. Nevertheless, small sections of continuous, well faceted diamond film were grown. An SEM photograph of such a film is shown in Figure 5.2.

On molybdenum, continuous films were obtained over a surface roughly equal to the burner face (4 cm diameter). Diamond deposits were obtained at two substrate temperatures: 1073 K and 1123 K. A photograph of the deposit region for the T_S = 1073 K case is shown in Figure 5.3. The film was well faceted, as the SEM photograph

R	Flow (slm/cm^2)	T_S (K)	P (Torr)	D_S (mm)	Substrate
1.15	0.939	~1150	52	1	Si
1.165	0.939	1073	52	1	Mo
1.165	0.939	1123	52	1	Mo

Table 5.1: Three conditions for diamond growth.

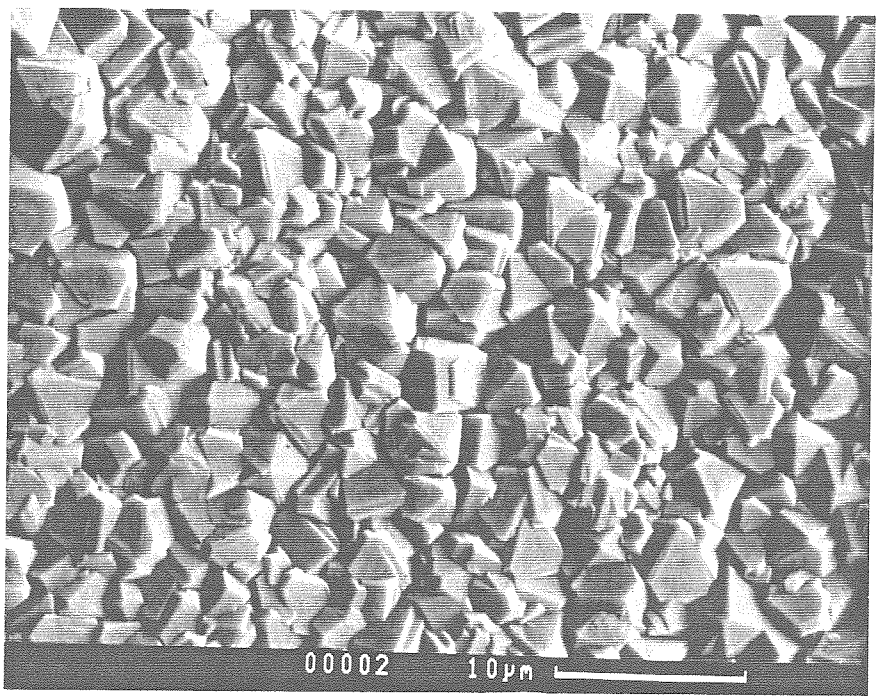

Figure 5.2: Small continuous region of diamond film on silicon.

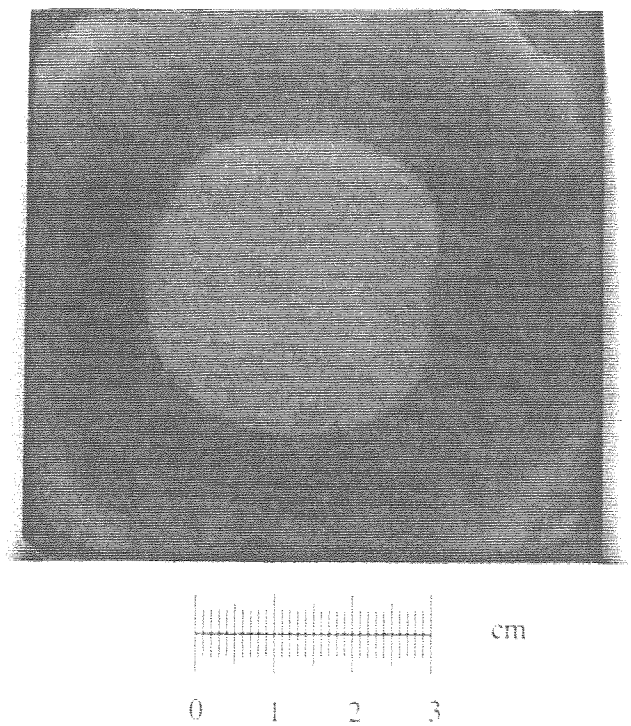

Figure 5.3: Photograph of the deposit region. The diamond film is the central gray region.

in Figure 5.4 shows. The microRaman spectrum of this film was taken at several radial positions in the deposit. Those results are given in Figure 5.5. The similarity in the spectrum at all three radial distances suggests that the film has very uniform purity. The sharp resolved peak at 1332 cm^{-1}, the rather small non-diamond peak at ~1550 cm^{-1}, and the small FWHM at 1332 cm^{-1} of ~5.4 cm^{-1} suggest that the diamond quality is very good.

The linear growth rate of the film was 0.6 μm/hour. This is within the range of

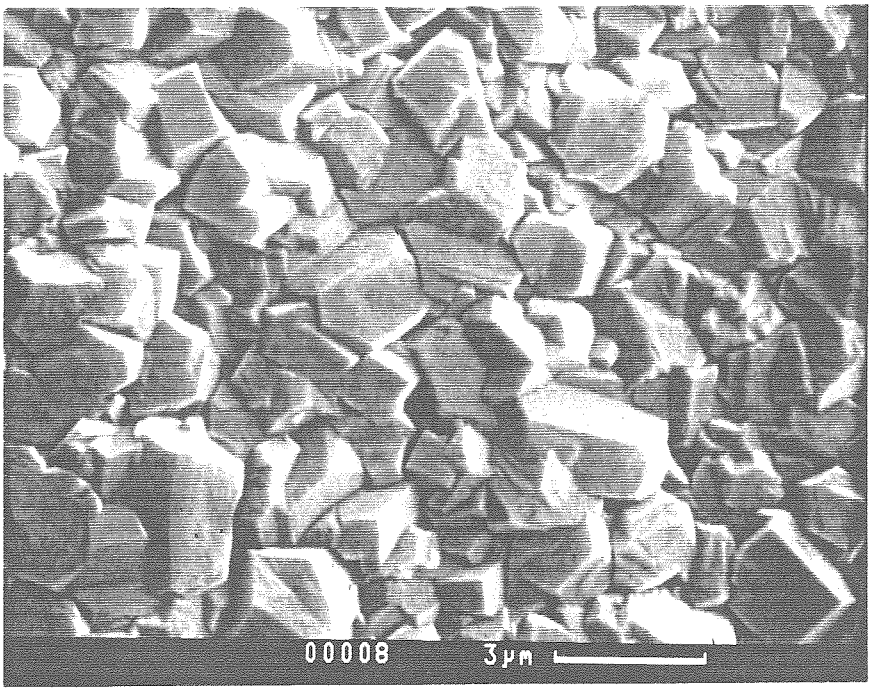

Figure 5.4: SEM photograph of diamond deposit at T_S = 1073 K.

growth rates commonly observed in hot filament and plasma reactors at the same pressure.

At T_S = 1123 K, the deposit size was the same as the lower temperature case. However, the growth rate increased to 1.0 μm/hour. Assuming similar near-surface species concentrations, the two growth rates correspond to an effective activation energy for diamond growth of 24 kcal/mole, which is in good agreement with the measured value of 23 kcal/mole of Kondoh *et al.* [54]. A plot of the growth rate with radial position in the deposit is shown in Figure 5.6. The film thickness uniformity is better than 4%. There is some evidence of a change in surface morphology with substrate temperature. The diamond surface grown at 1123 K exhibits more defects and has smaller crystal faces, though the difference between the two cases is slight.

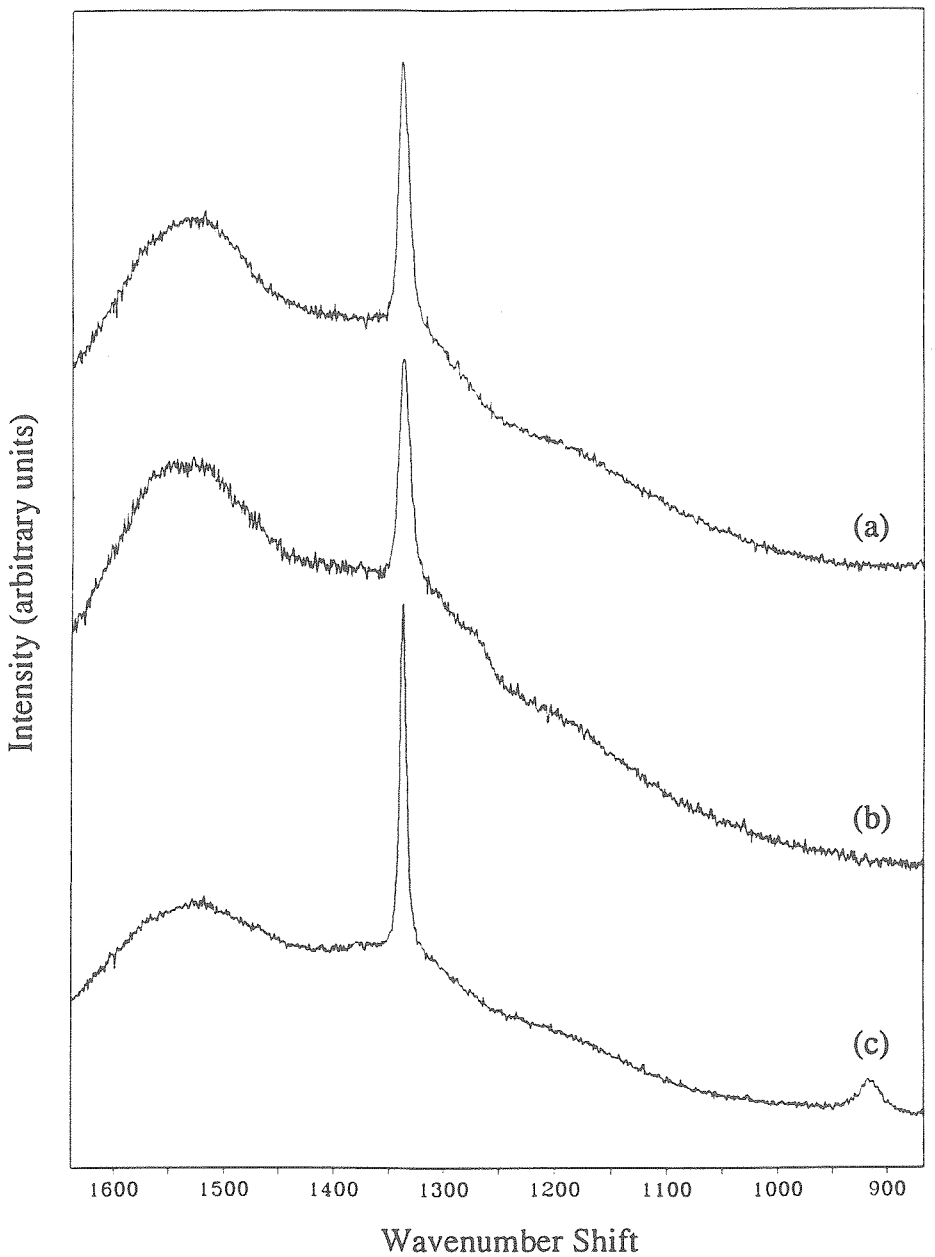

Figure 5.5: Raman spectra at various locations on the film: (a) center of deposit, (b) 6 mm from center, (c) 12.5 mm from center.

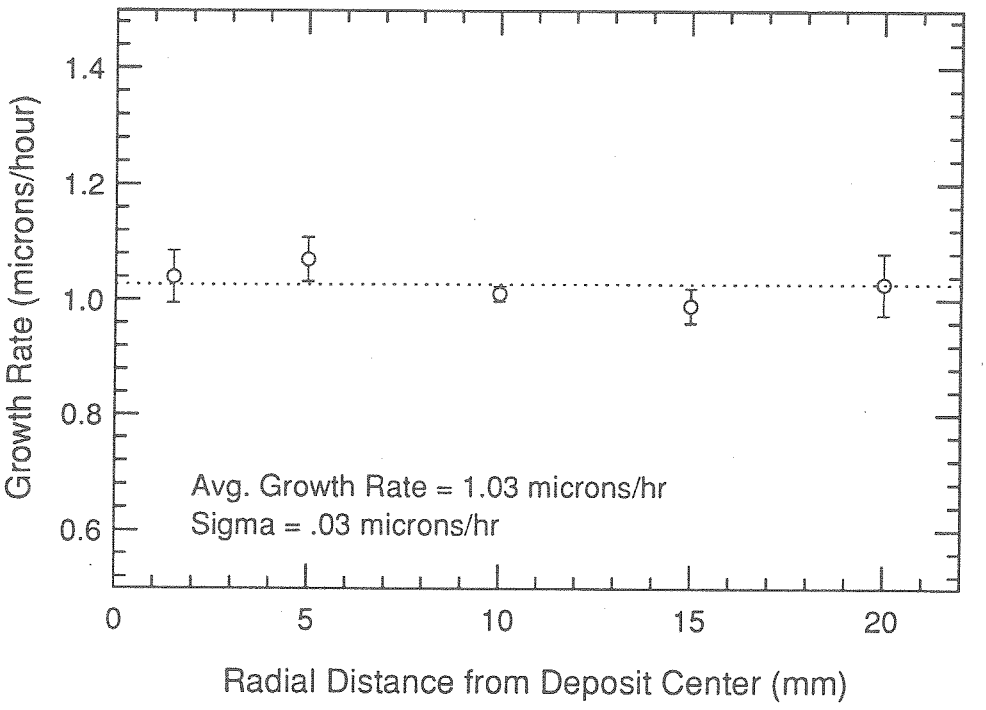

Figure 5.6: Film growth rate vs. radial position in the film.

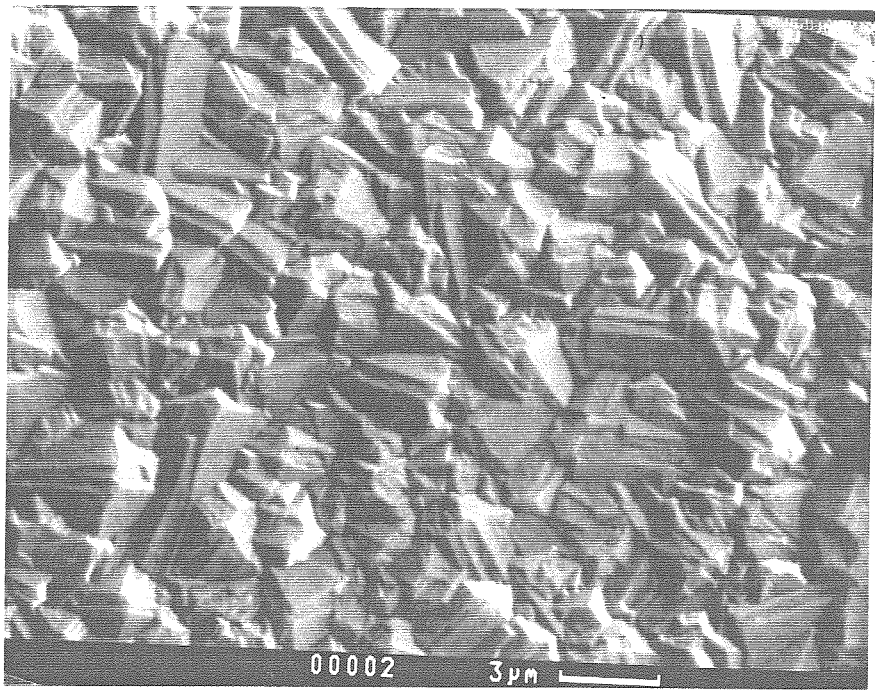

Figure 5.7: SEM photograph of diamond deposit at 1123 K.

5.4 Analysis

The flame model was applied to the T_S = 1123 K film growth case to analyze the predicted growth environment at the substrate surface. The flame, as expected, has many distinct differences from the previous low flow rate flames used to deposit isolated diamond crystals. The flame temperature is predicted to be significantly hotter at 3416 K. This is due to the increased heat release in the flame at higher flow rates. The strain rate is also higher, as expected, at 2930 s^{-1}. In general, the dramatically higher flame temperatures produce significantly more H and OH in the flame zone. Also, the faster kinetics provide for more complete combustion (at D_S = 1 cm) than observed in the low specific flow rate cases. Both C_2H_2 and O_2 are significantly lower at the substrate as are the intermediate hydrocarbon species in the acetylene oxidation chain (e.g., C_2H, CH_3, CH_2, etc.). Predicted mole fractions of the most prevalent radical species are shown in Figure 5.8.

At the substrate surface, the model predicts a sharp increase in [H] and [H]/[CH_3] over the lower specific flow rate cases. The model predictions for surface species are given in table 5.2. The high flow rate case also exhibits less O, OH, and O_2 at the surface. The predicted O_2 etch rate is .04 μm/hr, nearly two orders of magnitude smaller than the observed growth rate. It is thus likely that etching by O_2 is not a necessary process in these flames, unlike the situation at low flow rates. OH may still play a role in etching since the predicted maximum etch rate could be as large as 2.4 μm/hr, or 35% of the predicted growth rate.

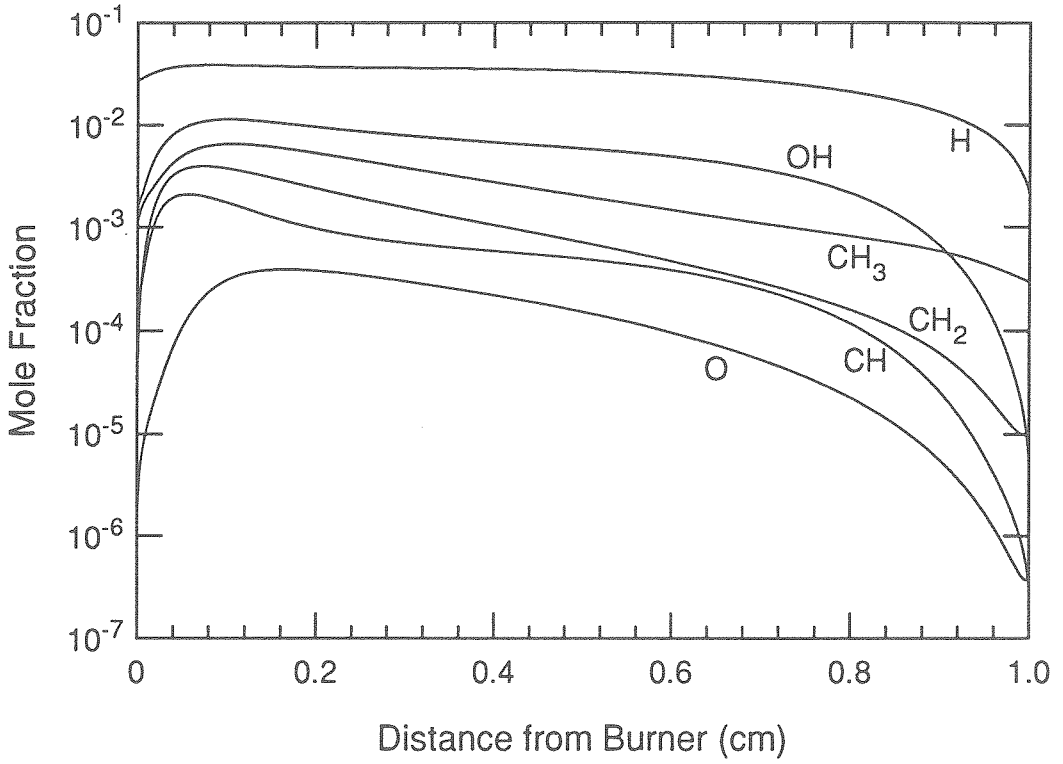

Figure 5.8: Model-predicted mole fractions of the most prevalent radical species with distance from the burner for a diamond growing flame with $D_S = 1$ cm, $T_S = 1123$ K, $P = 52$ Torr.

Surface Mole Fractions						
$\dot{m}$(g/cm^2-s)	H	CH_3	O_2	C_2H_2	OH	H/CH_3
2.0e-2	2.4e-3	2.0e-4	1.2e-5	1.7e-3	5.9e-6	12.3
2.8e-3	6.5e-4	5.8e-4	1.6e-4	3.9e-2	1.5e-6	1.1
Predicted Rates (μm/hr)						
$\dot{m}$(g/cm^2-s)	G_D	E_{D,O_2}	$E_{D,OH}$	$E_{D,O}$	$E_{D,total}$	G_D-E_D
2.0e-2	6.7	0.040	2.4	0.16	2.6	4.1
2.8e-3	2.7	0.60	0.34	0.022	0.96	1.8

Table 5.2: Comparison of experimental conditions and model predictions for high specific flow rate and low specific flow rate growth cases at T_S = 1123 K. For the high flow rate case, the conditions were: P = 52 Torr, R = 1.165, and D_S = 10 mm. For the low flow rate case, the conditions were: P = 35 Torr, R = 1.25, and D_S = 7.5 mm.

The predicted growth rates for both cases are considerably higher than the observed growth rates. In the high flow case, the predicted growth rate is 9.5 times the observed rates. Two reasons can account for some of this discrepancy. First, there is at least a factor of two uncertainty in the growth rate prediction. Second, the growth rate model is optimized for use at 1200 K. Assuming an activation energy for diamond growth of 23 kcal/mol [54], the growth rate at 1123 K would be about half the rate at 1200 K. This alone puts the predicted rate to within a factor of five of the observed rate. Still, either the model predictions for the growth environment, specifically [H] and [CH_3], are off by a factor of 2 or so, or the Harris mechanism does not predict growth rates nearly as well in the case of low pressure flames as it does for other growth methods.

This method compares favorably in term of deposition efficiency with the atmospheric torch methods. For a flame running 5.45 slm of C_2H_2 and depositing 1 μm/hr over a 12.7 cm^2 area, the method requires 40 standard liters of C_2H_2 per milligram of diamond deposit. Atmospheric torch methods require from 20 - 150 standard liters per milligram deposited [13, 16, 27]. Thus, at present, this method is competitive with the most efficient atmospheric torches.

5.5 Summary

Diamond films have been grown in low pressure acetylene/oxygen flat flames under two growth conditions. Growth rates varied from 0.6 to 1.0 μm/hr. The films are

very uniform in film thickness over the deposit area, and are also uniform in purity, as verified by a series of Raman spectra.

The linear diamond film growth rate was found to increase with substrate temperature. The amount of increase in growth rate was consistent with previously measured effective activation energies for diamond growth. Only small changes in surface morphology with deposition temperature were observed.

Model predictions for these cases project that the surface mole fraction of H is more than twice that seen in previous low pressure flat flame diamond growth conditions which could only deposit isolated diamond crystals. The [H]/[CH_3] ratio was also several times larger in the higher flow case.

The model results suggest that O_2 plays a considerably less significant role in these flames, while it is still possible that OH could be contributing significantly to the growth environment by etching sp^2 carbon.

Chapter 6

Post-Flame Injection Synthesis

6.1 Introduction

In the previous work with acetylene/oxygen flames, described in Chapters 4 and 5, the surface concentrations of H and O_2, as well as the ratio $[H]/[CH_3]$, were found to be important parameters in determining whether or not a particular environment will grow diamond. However, [H] and $[H]/[CH_3]$ could not be varied over a wide range of values nor could they be varied independently of each other or of $[O_2]$. To truly optimize the diamond growth process for deposit quality and growth rate, independent control over each of these parameters is desirable.

Flat flames can potentially offer this level of control over the growth environment using a combination of a hydrogen/oxygen flame and post-flame injection of methane. H_2/O_2 flames can produce abundant quantities of atomic hydrogen ($> 5\%$) in the post-flame zone. Also, the amount of residual O_2 and OH in the post-flame gases can be controlled relatively independently of H by varying Φ or D_S. In addition, the available range of O_2 and OH in the post-flame gases extends over a wide range from less than 10^{-4} mole fraction to about 10^{-2} mole fraction. Lastly, by injecting a methane mixture near the surface, the amount of $[CH_3]$ and thus the $[H]/[CH_3]$ ratio can potentially be varied independently of both $[O_2]$ and [H].

There are several additional reasons why this environment is interesting for diamond growth. First of all, atomic hydrogen is produced by gas-phase reactions, and therefore no filaments or cathode surfaces are present to cause film contamination problems. Also, using flat-flame burners, uniform H and OH concentrations may be

generated over arbitrarily large areas, without the significant substrate cooling problems which arise using atmospheric-pressure torch flames. Finally, hydrogen/oxygen flames are typically easy to model since the gas phase reaction mechanism is fairly small, and many gas phase diagnostics have been developed for and demonstrated in such flames.

In this chapter, diamond growth using two simple injection geometries is demonstrated and investigated. While neither of these is optimal for mixing and uniform film growth, they illustrate how mixing and reaction between the injected hydrocarbon and the surrounding flame affect diamond growth. The effects of varying experimental parameters on diamond growth are examined, and gas-phase diagnostics and numerical modeling are used to examine this growth environment.

6.2 Experimental

Apparatus

The experimental setup, shown in Figure 6.1, consists of a low-pressure flat flame burner (6 cm diameter) which is the same as described previously. The burner and substrate are contained within the Low Pressure Combustion Facility. All gases are provided from compressed gas bottles, metered by the electronic mass flow controllers, and mixed thoroughly before entering the chamber.

A silicon substrate, heated by contact with a molybdenum strip through which

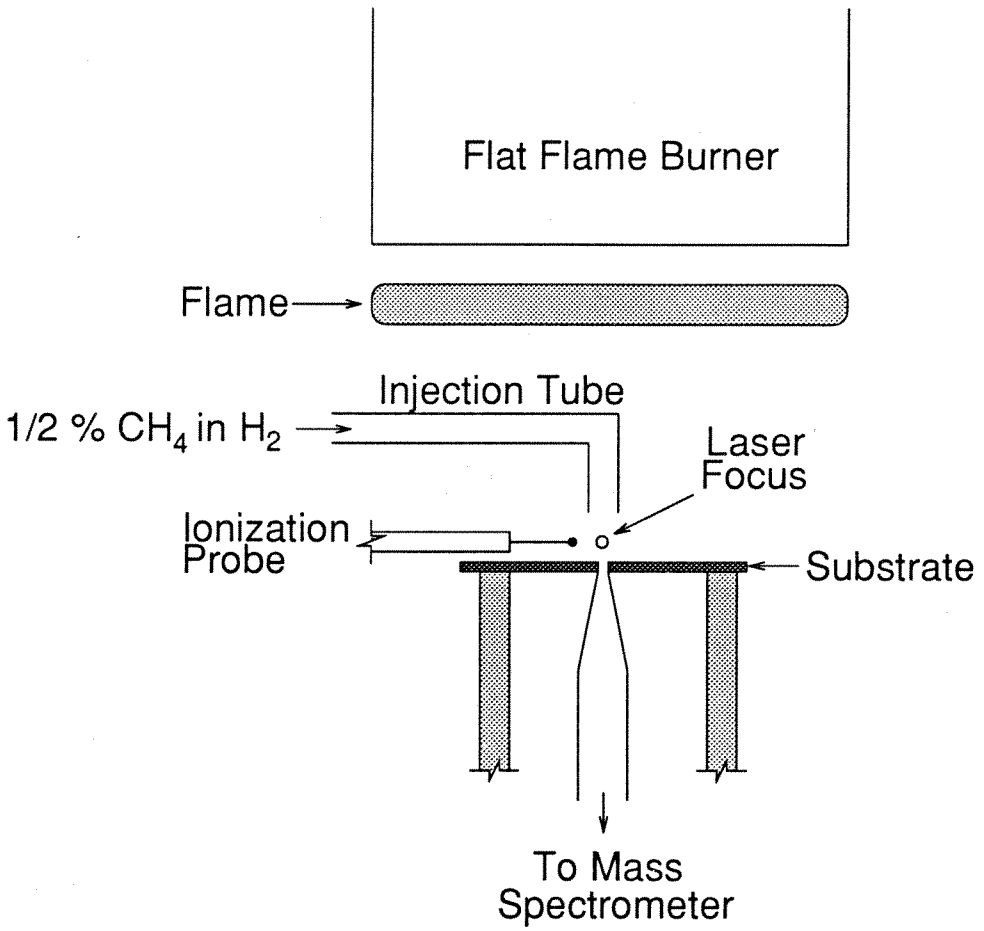

Figure 6.1: Experimental setup.

current is passed, is placed in the post-flame gases about 5 cm from the burner surface. The substrate temperature is monitored with the infrared one- and two-color pyrometers. A methane/hydrogen mixture is injected near the substrate through a small 1.7 mm ID tube (either molybdenum or alumina), which is mounted on a horizontal translation feedthrough. A quartz sampling probe allows extraction of gas through a small hole in the molybdenum substrate support for analysis with the quadrupole mass spectrometer. The setup allows for variation of burner to substrate and injection tube to substrate distances, injection tube lateral position, injection flow rates, flame stoichiometry, substrate temperature, and system pressure.

Growth conditions

For this work, slightly rich (Φ = 1.25 to 1.5) hydrogen/oxygen flames are run at 30 to 40 Torr. In some cases up to 5% of acetylene, pre-filtered through activated charcoal for acetone removal, is added to the premixed gases. As discussed below, this is done to alter the composition of the post-flame gases, specifically OH, O, and O_2. The flame conditions used for most of the experiments are as follows: flow rates: H_2 = 4 slm, O_2 = 1.6 slm, C_2H_2 = 0.33 slm (when added); pressure = 35 torr. These conditions result in an unburned gas velocity at the burner of about 75 cm/s.

An injected gas mixture of 0.5% CH_4 in H_2 was used for most of the experiments reported here. Both vertical injection, perpendicular to the substrate (as shown in Figure 6.1), and horizontal injection, parallel to the substrate, have been used

successfully to deposit diamond. From measurements of the tube surface temperature, the injected gas is estimated to exit the tube at 800 °C. The injected gas flow rate is 200 sccm, resulting in a velocity at the tube exit of about 100 m/s. Using kinetic theory estimates for the gas viscosity, we estimate a Reynolds number of ≈ 10 for the injected flow based on the tube diameter. Thus, we expect that the flowfield is laminar.

All substrates are prepared by scratching with 1 micron diamond paste before deposition. In addition, several of the substrates were exposed to additional nucleation enhancement by placing them in a rich acetylene/oxygen flame (C_2H_2:O_2 = 1) for 15–30 minutes prior to the deposition period. This procedure resulted in up to a tenfold increase in nucleation density over the substrates which were only scratched.

Diagnostics

To understand the mixing and reaction between the injected methane and the surrounding post-flame gases, measurements are made of radial species profiles at the substrate. The diagnostic measurements are done with a vertical injection tube. By translating the injection tube horizontally with respect to the measurement position, relative radial profiles of species concentration may be measured.

Profiles of stable species at the substrate are measured by mass spectrometry, sampling gas through the quartz probe. The probe orifice diameter is ≈ 0.2 mm, which based on previous studies [60] should yield a spatial resolution of ≈ 0.5 mm.

The probe pressure is kept at 0.5 torr to rapidly quench chemistry other than radical recombination. The sampling procedure is similar to that used previously by Harris, Weiner and Perry [61] in their study of filament-assisted diamond growth and is described in more detail in Chapters 2 and 3.

Radial profiles of CH_3 are acquired using resonance-enhanced multiphoton ionization (REMPI). This technique has been used in previous studies to detect CH_3 during HFCVD diamond growth [62, 63], and has proven to be a sensitive diagnostic for methyl. For the REMPI measurements, the output of a YAG-pumped dye laser is frequency doubled, yielding tunable pulses at 10 Hz near 333 nm (0.08 cm^{-1} bandwidth). The pulse duration is 7–8 ns, and typical pulse energies are 1 mJ.

The UV laser pulse pumps the $3p^2A_2'' \leftarrow X^2A_2''$ (0-0) transition of CH_3 via two-photon absorption. This is followed by an incoherent single-photon ionization ((2+1) REMPI). The electrons generated are collected by an ionization probe, which consists of a positively-biased 250 μm platinum wire supported by a ceramic tube. The measured ionization signal at the peak of the CH_3 line at 333.46 nm is a measure of the local CH_3 concentration.

With the present laser focusing scheme, we estimate that ionization takes place over roughly 5 mm along the beam waist. Since the injection tube diameter is less than this, our measured methyl profiles are not fully spatially resolved, particularly near the axis. In principle, an Abel inversion could be applied to estimate the true radial CH_3 profile, but this has not been done here.

The laser beam is focused approximately 0.5 mm above the substrate surface. The ionization probe is placed adjacent to the laser focus approximately 1-2 mm away. The probe bias voltage (100 V) is chosen to obtain saturated electron collection without significant secondary ionization [63]. For the REMPI measurements a ceramic injection tube is used, to minimize perturbation of the electric field near the probe (and therefore the REMPI collection efficiency) as the tube is translated. Since the laser focus, probe and all grounded surfaces are fixed in position throughout the data acquisition process, the REMPI collection efficiency is assumed to be constant. Since the gas temperature at the measurement location is also approximately constant, the profile with radial distance of the REMPI signal, corrected for the nonresonant background, can be interpreted as a relative CH_3 concentration profile (averaged, however, over the laser focus).

6.3 Results

Diamond Growth

Diamond growth with the present setup has been observed under a wide variety of conditions. Typical conditions yield particles such as those shown in Figure 6.2, and a typical micro-Raman spectrum for an isolated particle is shown in Figure 6.3. Deposit sizes are typically about 5 mm in diameter and circular or oval in shape, depending on injection geometry. Outside the diamond growth region, there is no carbon deposition, and the silicon substrate appears to be oxidized. This suggests

that the flame, even though run rich, is too oxidizing for film growth outside the region on the substrate near the injection tube, which is protected from oxidation by the jet flow.

Observed growth rates based on the radius of deposited crystals are between 1/2 and 1 micron/hr. Substrate temperatures were varied from about 725 to 950 °C, but no deposit (diamond or non-diamond) was observed for T_S below 850 °C. Attempts to deposit diamond with a 5% mixture of CH_4 in H_2 resulted in deposition of only non-diamond (usually ball-like) carbon. These non-diamond deposits were similar to those seen in acetylene/oxygen flames.

The nucleation density of deposits was again sparse compared to hot filament reactors, even with nucleation enhancement. Scratching of substrates increased the nucleation density. Along actual scratches, the nucleation density was very high, as shown in Figure 6.4 which depicts a diamond deposit after only 4 hours. The thick continuous region of diamond represents the location of a scratch on the surface.

In a typical deposit, the crystal morphology is observed to vary with position. An example of this is shown in Figures 6.5–6.9. Figure 6.5 is a schematic of a diamond deposit and shows the positions of the particles photographed for Figures 6.6–6.9. This deposit was obtained using horizontal injection at the substrate of 0.2 slm of 0.5% methane in hydrogen. The H_2/O_2 flame was run rich at $\Phi = 1.25$ with 5.25 total slm of flow. The substrate was held at 3.3 cm below the burner. The system pressure was 36 Torr, and T_S was 1208 K. The highest quality diamond is seen at

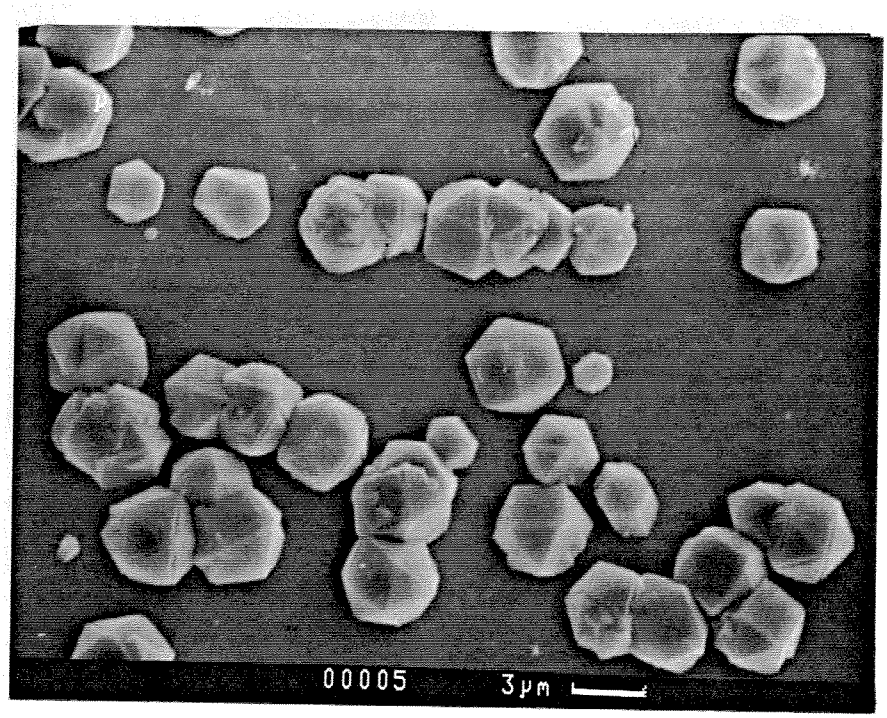

Figure 6.2: Typical deposited diamond.

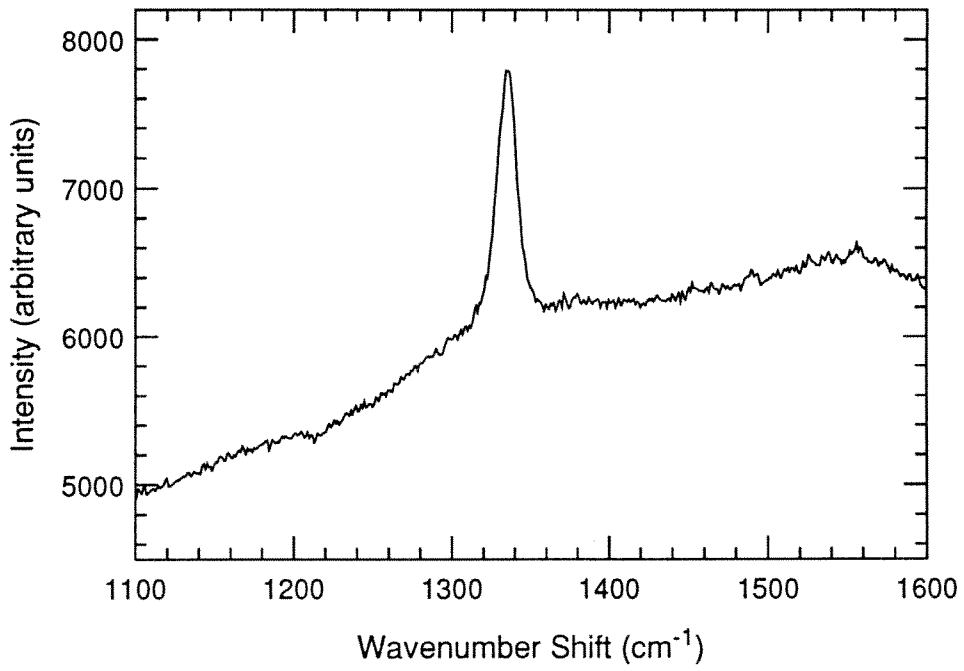

Figure 6.3: Typical microRaman spectrum of an isolated crystal.

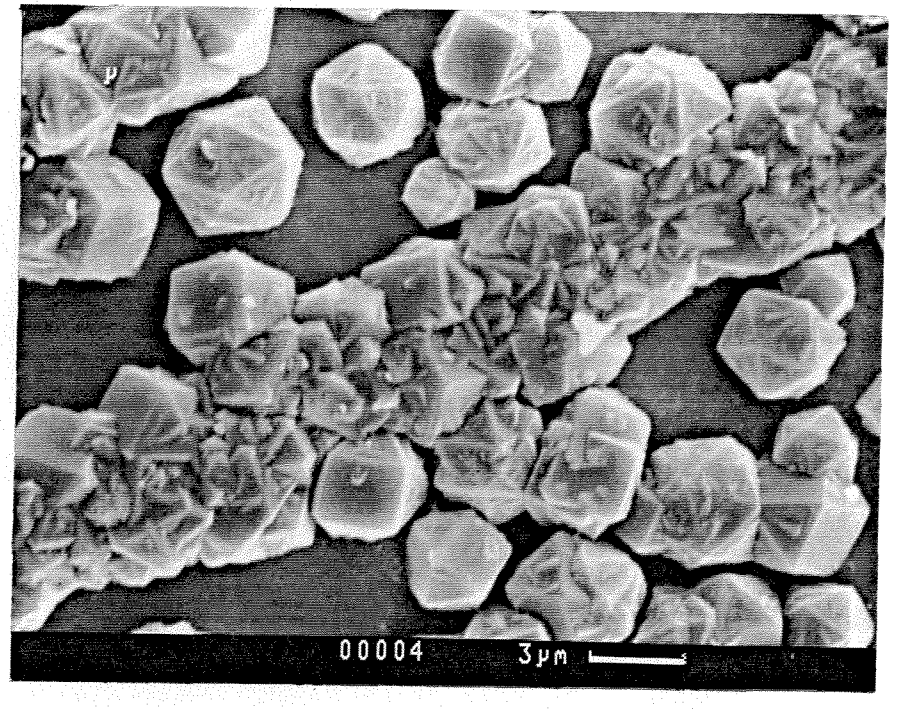

Figure 6.4: Deposit in and around a surface scratch.

the outer edges of the deposit where the injected gases are mixed to the greatest extent with the post-flame gases. Near the center of the deposit, where presumably H, OH, and O_2 penetration is poorer, more secondary nucleation is observed on the deposited crystals, and, in some cases, ball-like particles are observed. This suggests that mixing with the etchants and oxidants from the flame is crucial for maintaining high-quality diamond.

To examine the role of oxidation in determining the deposit size and quality, experiments were run with a small amount of acetylene added to the fuel, and the deposit compared to that without acetylene. The primary effect of the acetylene addition is to to consume additional oxygen, reducing OH, O, and O_2 concentrations in the post-flame region, making the environment at the substrate more reducing.

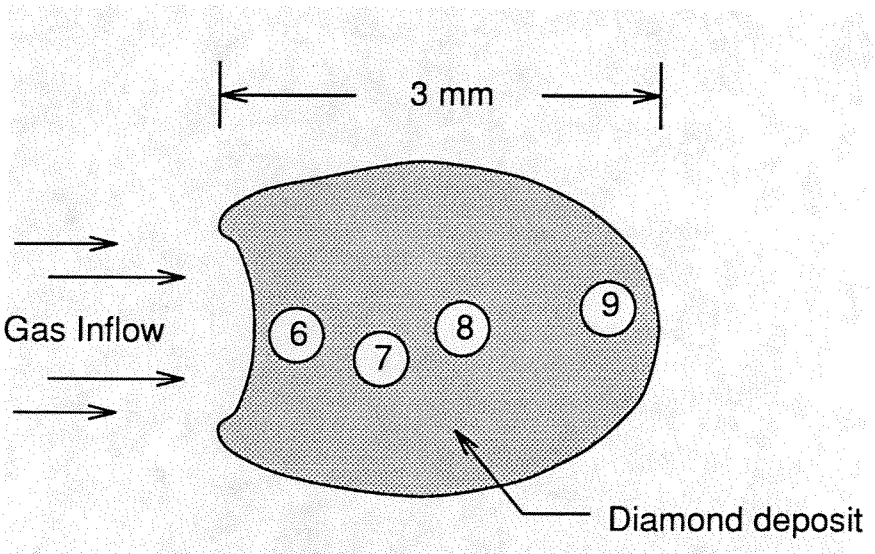

Figure 6.5: Deposit schematic and locations of Figures 6.6–6.9.

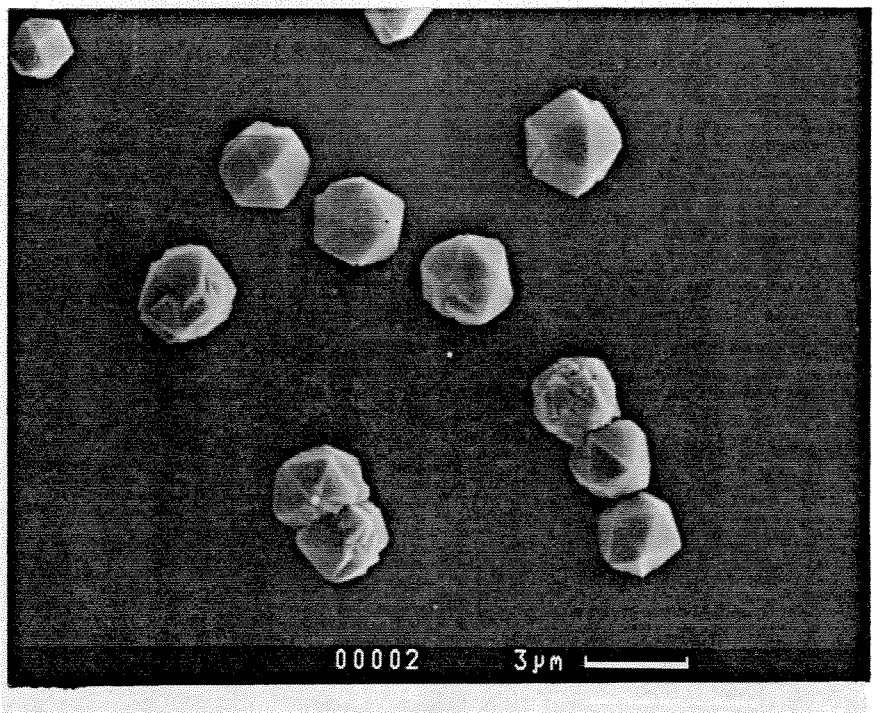

Figure 6.6: Diamond from near the leading edge of the deposit.

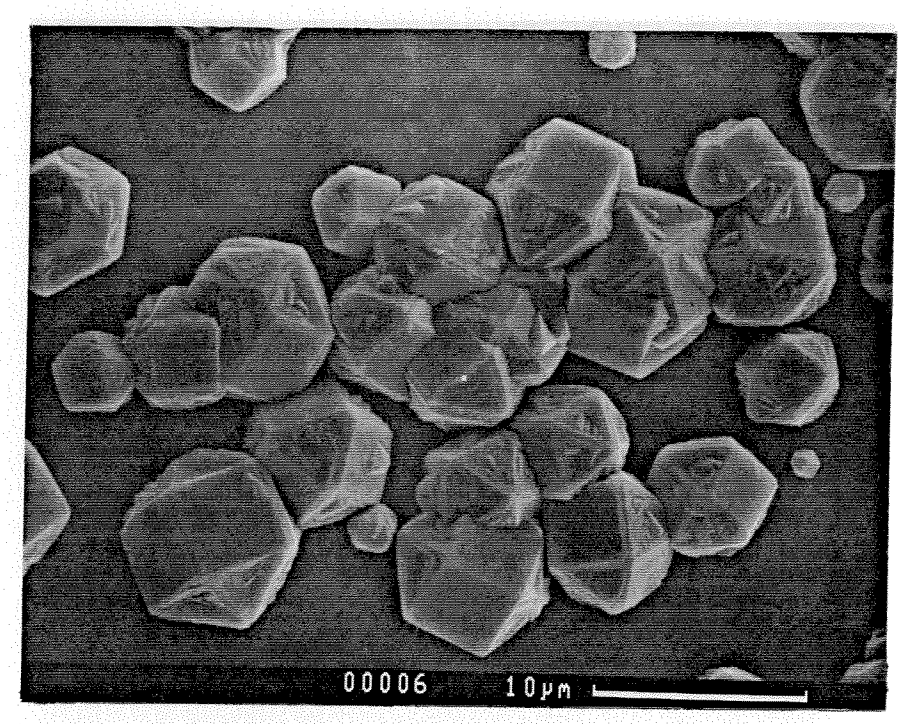

Figure 6.7: Between the leading edge and center of the deposit.

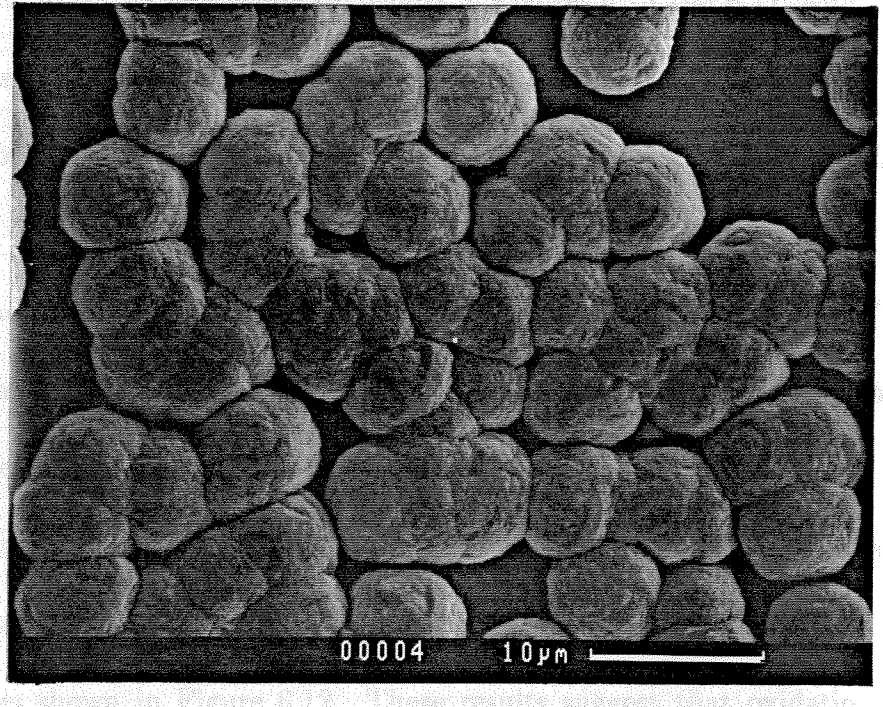

Figure 6.8: Particles at the center of the deposit.

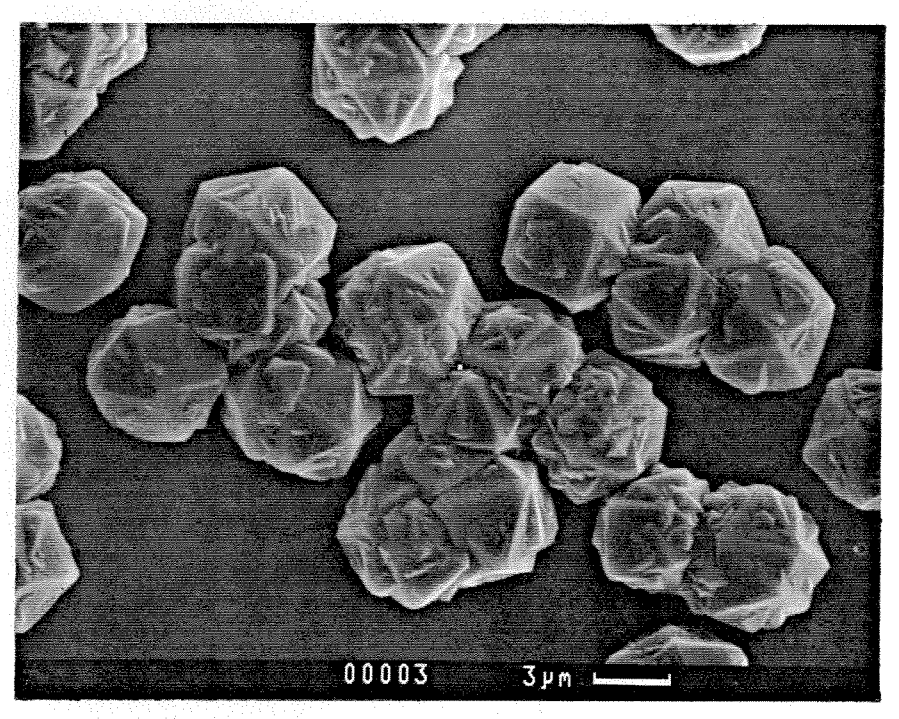

Figure 6.9: Diamond at the trailing edge of the deposit.

This is seen in the flame simulation results in Figures 6.10 and 6.11, which were done using the same reacting flow model used to analyze the acetylene/oxygen flames. The presence of the substrate is neglected in these simulations. As seen in Figure 6.11, the added C_2H_2 is oxidized in the reaction zone, and thus does not directly contribute to diamond growth. The H concentration and the flame temperature ($\approx$ 1700 K) are hardly changed by the C_2H_2 addition, but the concentrations of all oxidizing species are dropped by at least an order of magnitude.

The deposit diameter was found to increase by up to a factor of two with 5% acetylene addition. A schematic of two deposits, one with and one without acetylene addition, is shown in Figure 6.12. These results suggest that oxidation limits the deposit size with the present injection geometry. Although the deposit size increased,

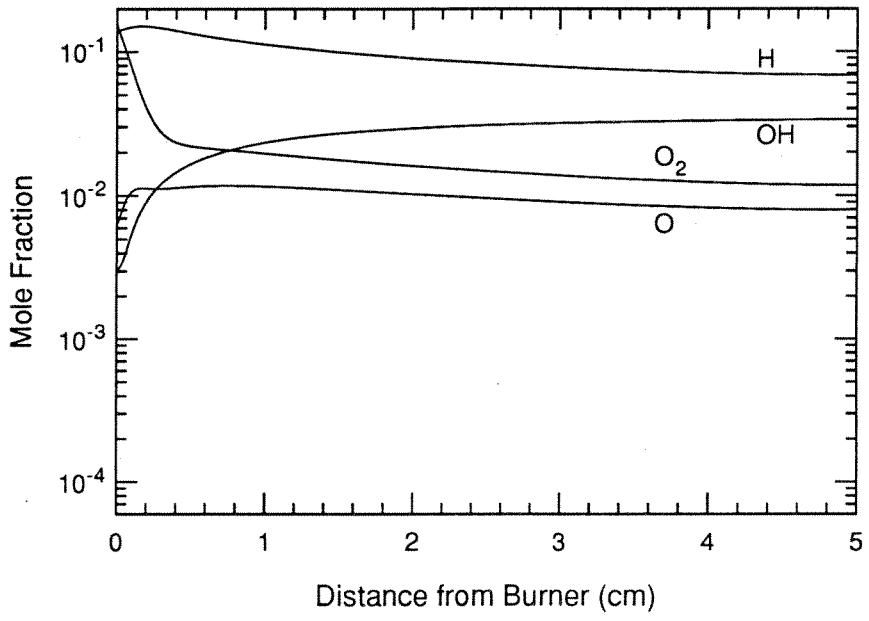

Figure 6.10: Predicted species profiles: H_2/O_2 flame.

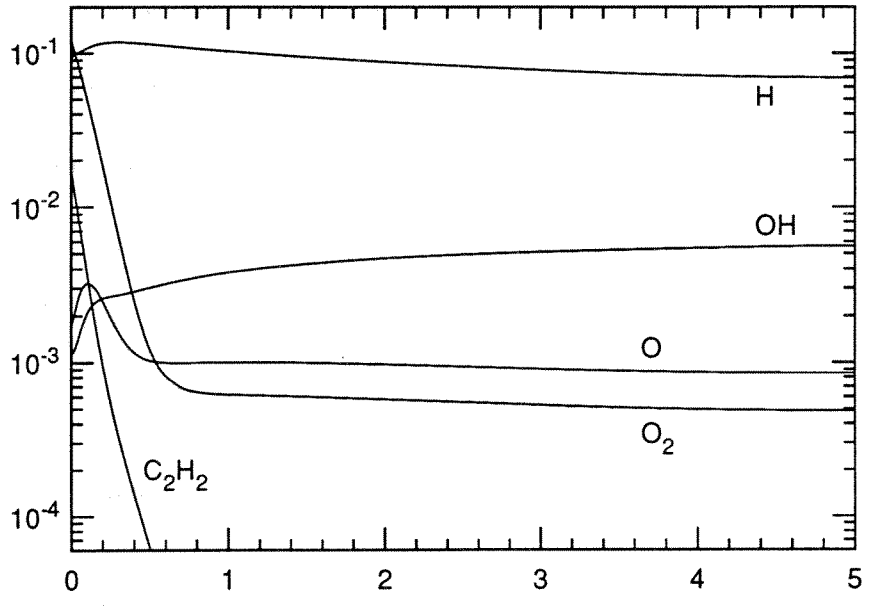

Figure 6.11: Predicted species profiles: 5% C_2H_2 addition.

the diamond quality at the center of the deposit was somewhat poorer with C_2H_2 addition, showing more secondary nucleation. This may also be due to the lower OH concentrations, resulting in less effective etching of non-diamond carbon.

Diagnostics

For a flame with acetylene addition, relative concentration profiles of H_2 and CO at the substrate surface were measured as a function of radial distance from the injection tube centerline using mass spectrometry. Figure 6.13 shows these radial relative concentration profiles. The sharp concentration gradients which persist past 7 mm suggest that the mixing zone extends out substantially further than the deposit region which is typically less than 3 mm in radius.

Relative concentration profiles of CH_4 obtained by mass spectrometry and CH_3 obtained by REMPI are shown in Figure 6.14, for a flame with no C_2H_2 addition. The CH_3 concentration is seen to peak at larger radii than the CH_4 concentration, which is largest at the injection tube centerline. Since methyl is produced by the fast bimolecular reaction

$$\mathsf{CH_4 + H \rightleftharpoons CH_3 + H_2}, \tag{6.1}$$

the methyl concentration should scale approximately as $[CH_3] \propto [CH_4][H]$, which, since H must diffuse from outside the jet toward the center, will produce a methyl radial profile like that seen in Figure 6.14. Methyl remains above 30% of its maximum value out to 15 mm from the injection jet while deposit radii are always less than 3

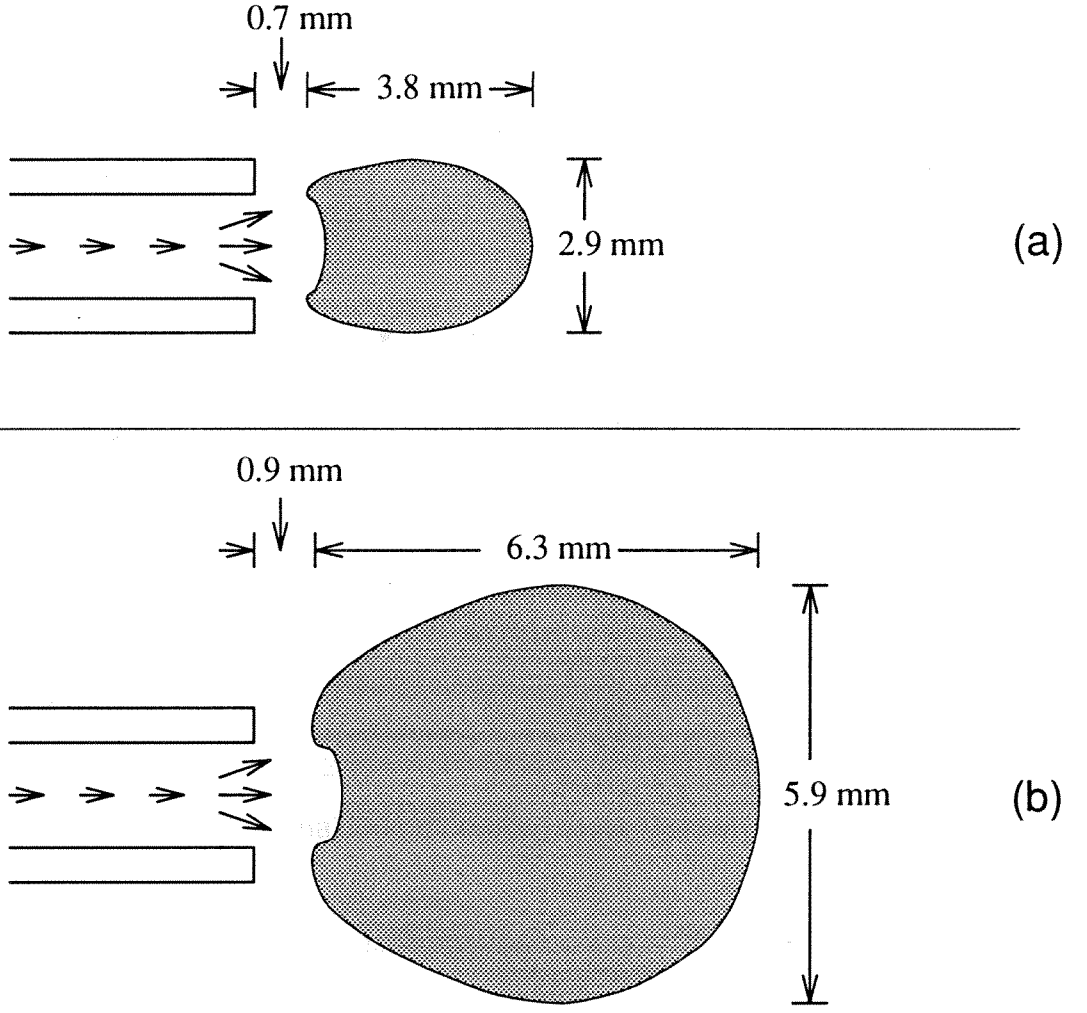

Figure 6.12: Deposit areas; (a) without acetylene addition, (b) with acetylene addition.

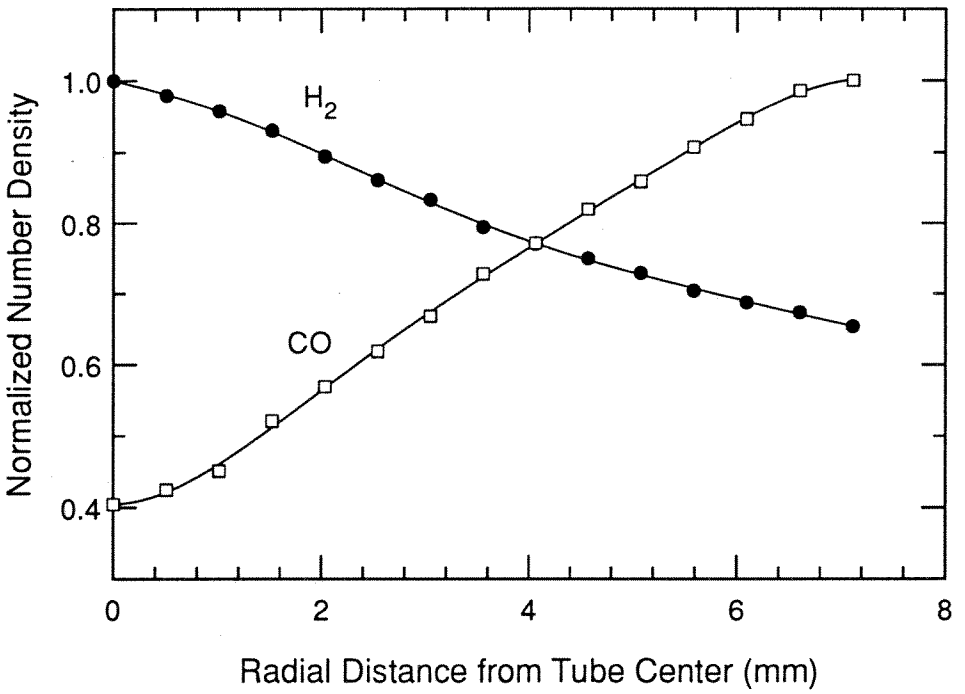

Figure 6.13: Spatial profiles of relative concentraions of H_2 and CO at the substrate surface.

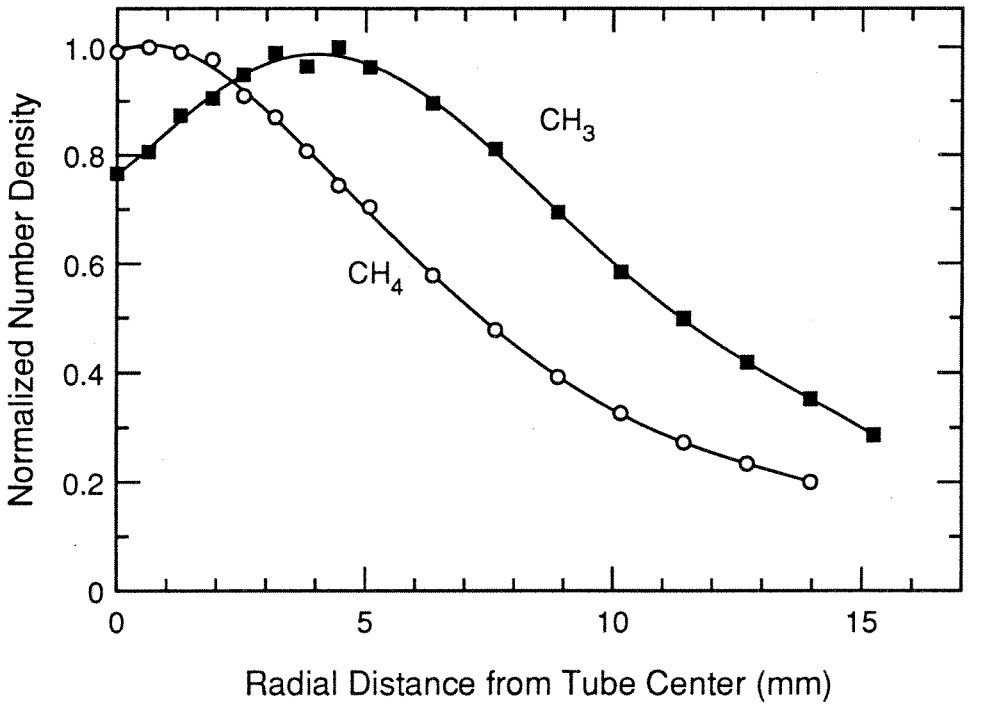

Figure 6.14: Spatial profiles of CH_3 by REMPI and CH_4 by MS.

mm. This too indicates that the lack of growth at radial distances beyond 3 mm is probably not due to lack of growth species or H atom concentration, but rather to oxidation.

Attempts were made to measure profiles of C_2H_2 and C_2H_4, but their concentrations were below the detection limits of our mass spectrometer. From this, we can estimate an upper bound on the acetylene mole fraction at the substrate of 2×10^{-5}. The low acetylene concentration at the substrate indicates the degree of control over the chemical composition of the gas at the substrate which is possible with this method, unlike most other diamond CVD techniques where the hydrocarbon gases pass through the activation region.

Modeling

To model the flow region around the injection jet and near the substrate, the commercial 3-D CFD code FLUENT (Fluent Inc., Lebanon, NH) with limited kinetic modeling capability was used. FLUENT solves the momentum, energy, and species conservation equations to yield the velocity, temperature, and concentration fields throughout the domain. For the present simulations, we use estimated diffusion coefficients, viscosity, and thermal conductivity, all assumed to be constant. The flow was modeled as a 2-D axisymmetric jet impinging on an infinite substrate. A schematic of the modeled problem is given in Figure 6.15. The composition shown in Figure 6.10 was used as the input to FLUENT for the post-flame gas composition, and the other code inputs were chosen to match experimental parameters.

In this simplified problem, the chemistry is confined to reaction 6.1 (both forward and reverse directions), plus recombination via

$$CH_3 + H + M \rightarrow CH_4 + M. \tag{6.2}$$

The reverse of reaction 6.2 is neglected since its contribution for the temperatures and concentrations of the posed problem is negligible compared with the forward rate of reaction 2.

Results for the normalized radial profiles of CH_4 and CH_3 at the surface are shown in Figure 6.16. These calculations were done for conditions simulating the experimental conditions of figure. The qualitative agreement between model and experiment is good, although the calculated CH_4 profile falls off somewhat more

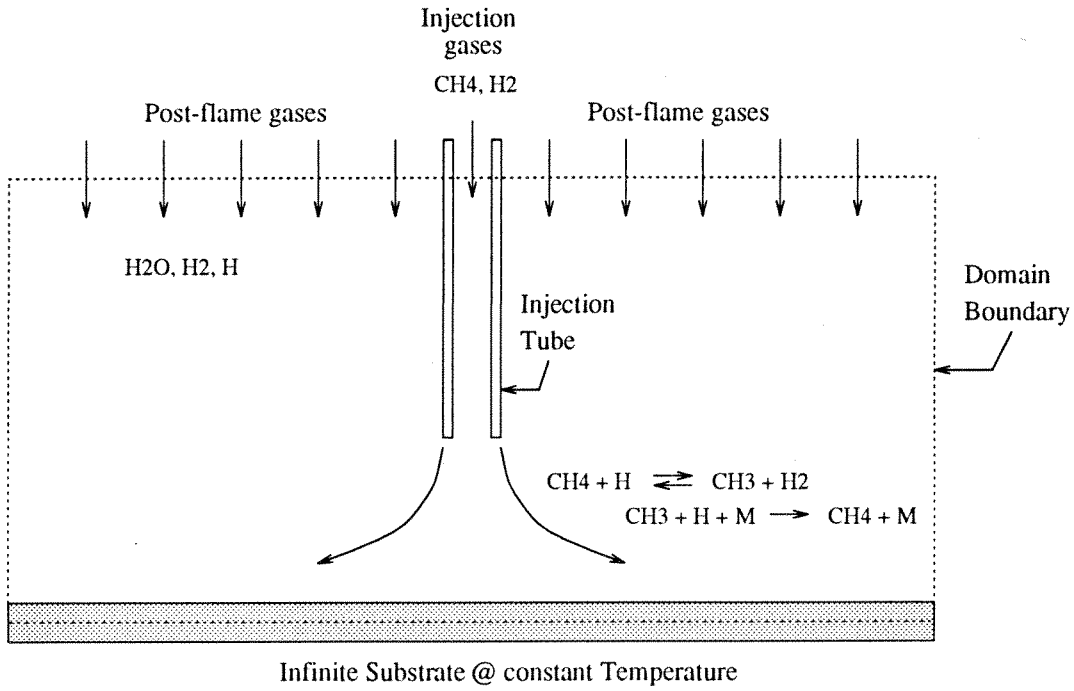

Figure 6.15: Domain of the problem modeled using FLUENT.

rapidly than that measured. Nevertheless, the FLUENT simulations are useful for providing insight into the reaction and mixing in this flow, which will allow design of optimal gas injection schemes.

6.4 Discussion

The REMPI CH_3 measurements show that $[CH_3]$ remains above 50% of its maximum concentration in a region extending out to a radius of at least 10 mm from the injection tube centerline. Since this is significantly greater than the deposit radius ($\approx$ 3 mm), we conclude that availability of methyl is not the limiting factor determining the size of the diamond deposit. The acetylene injection experiments, together with the flame simulations, show that the deposit size increases when the concentration of oxidants

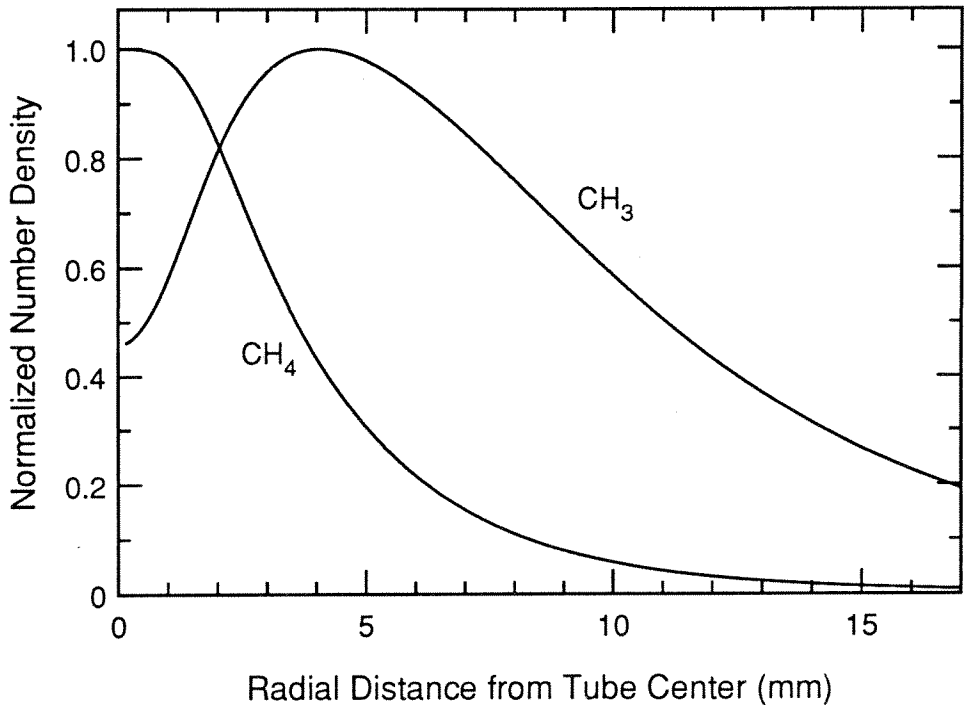

Figure 6.16: FLUENT predictions of the spatial profiles of CH_3 and CH_4.

decreases.

This suggests that oxidation (primarily by OH and O_2) controls the deposit size with the present injection scheme. Indeed, even with the acetylene addition, the predicted potential etch rate of diamond by O_2 is $\sim$ 2 microns/hour. This is significantly higher than the observed growth rate within the deposit area. Thus, obtaining larger deposits would certainly involve further decreases in the oxidant concentrations in the post-flame gases.

The relatively low nucleation densities obtained may also be related to the high oxidant levels, although no serious attempt to achieve high nucleation densities was made here. If OH, O, and O_2 oxidize nuclei during the first minutes of growth, this

may explain the limited deposit size.

6.5 Summary

The growth of well-faceted, isolated diamond crystals on silicon substrates by injecting methane/hydrogen mixtures into hydrogen/oxygen flames has been demonstrated. For the present conditions, the diamond deposits are approximately 5 mm in diameter. Adding acetylene to the flame to suppress OH, O, and O_2 was found to increase the deposit diameter by up to a factor of two; from this, it appears likely that oxidation limits the deposit size with the present injection scheme.

To better understand the chemical environment at the substrate during growth, radial profiles of CH_4, CO, H_2, and CH_3 have been measured. Concentration profiles for CH_3 and CH_4 near the substrate surface show ample growth species present for diamond growth over radii of up to 15 mm from the injection tube. These results suggest that limiting the amount of oxidants in the post-flame gases may lead to larger area deposition. Numerical simulations show qualitative agreement with the measured profiles, indicating that we understand and can model the most important features governing the CH_3 distribution near the substrate. The present experiments have served to demonstrate diamond growth and carry out some initial diagnostic measurements. Studies of the mixing and reaction in this system are now underway to find optimal conditions for large-area, continuous film growth.

Chapter 7

Summary and Conclusions

7.1 Review of Results and Conclusions

This study has attempted to evaluate low pressure flat flames as a potential method for diamond chemical vapor deposition. The results of this work have lent insight into the growth environments produced by these flames as well as the problems associated with diamond deposition in them.

To analyze the deposition environments, a flame model incorporating gas phase chemistry, surface chemistry, and all transport processes was used. The Miller/Melius mechanism was chosen for the gas phase chemistry, and a surface chemistry mechanism was assembled to account for the key processes occurring at the deposition surface including: diamond growth (*via* the Harris mechanism), recombination of H, OH, O, and etching of diamond by O_2.

The flame model was tested at conditions near those used for diamond growth using laser-induced fluorescence and mass spectrometry. The model was found to predict the gas phase temperature to within 175 K. The relative spatial OH number density profile was in excellent agreement with the model predictions as well. The mass spectrometry results revealed that the surface concentrations of CO and H_2 were predicted to within experimental uncertainty over a wide range of equivalence ratios. The surface concentrations of C_2H_2 and CH_4 were slightly underpredicted by the model, but the trends in concentration with equivalence ratio matched well with the experimental observations. These measurements suggest that the model is capable of accurately predicting trends in surface species concentrations with varying

experimental parameters and can accurately predict surface concentrations for some important species.

A series of deposition experiments was performed using acetylene/oxygen flat flames at ~40 Torr to identify experimental conditions which yield diamond growth on a heated substrate. Several growth conditions for isolated diamond particles were identified, and deposits were verified as diamond by Raman spectroscopy. The nucleation densities observed in these flames were low compared to other diamond CVD methods, but densities were increased by the use of nucleation enhancement techniques early in the growth run. The effects on diamond growth of varying experimental parameters such as T_S, D_S, and R were observed.

The flame model was then used to predict the growth environment present at the substrate surface for a series of growth runs. The results predict that the flat flame growth environment at low specific flow rates is typically characterized by a relatively small [H]/[CH_3] ratio and relatively large amounts of O_2 compared to other diamond CVD methods. Further analysis suggests that the abundance of surface O_2 allows diamond to grow at such small [H]/[CH_3] ratios by removing excess sp^2 carbon. OH may also play a similar role. Because there are no data on the diamond or non-diamond etch rate by OH, the magnitude of the contribution of OH to the diamond growth process is unclear. However, modeling results (using upper and lower bounds on the OH etch rate of diamond) suggest that, in some cases, OH may account for a similar or larger non-diamond and diamond etch rate at the substrate than O_2.

The region of parameter space in which diamond grows appears to be dictated by a balance between growth and etching of sp^2 and sp^3 carbon. Flames which leave no deposit at the surface are characterized by potential diamond etch rates which exceed the diamond growth rate. Flames which leave only sp^2 carbon in the deposit are characterized by non-diamond etch rates which are too small to remove a substantial fraction of the deposited non-diamond carbon. In between these two cases are sometimes diamond growth conditions, if the deposition ratio D_r is greater than $D_{r,crit}$. For the low specific flow rate flames, D_r exceeds $D_{r,crit}$ only as long as silicon (the substrate material) controls the surface kinetics at the substrate. As the deposit coverage increases, D_r drops below its critical value, and thus no diamond films may be grown.

The model was successful in predicting certain aspects of the growth process. In many cases, the observed diamond particle growth rates were within the uncertainty of the predictions of the Harris mechanism in the flame model. Also, for a series of experiments in which a single parameter R was varied, the value of R at which the diamond etch rate exceeds the diamond growth rate, as observed in a series of growth experiments, was within the uncertainty of the prediction of the model.

A simplified analysis was used to identify the critical parameters in the deposition ratio. The analysis suggested that D_r can be increased by corresponding increases in [H] and/or $[H]/[CH_3]$. The flame model suggests that by increasing the specific flow rates an order of magnitude, [H] can be doubled and $[H]/[CH_3]$ tripled. These

larger specific flow rates were used in a modified facility, and diamond film growth conditions were isolated. Film growth rates of 0.6 μm/hr at T_S = 1073 K and 1.0 μm/hr at T_S = 1123 K were observed. The uniformity of the deposit quality (as measured by the Raman spectrum) and the film thickness over the 2 cm radius were excellent.

The flame model predicts that these film growth conditions, in addition to the higher [H] and [H]/[CH_3] values, are characterized by significantly lower diamond etch rates due to O_2. OH may play a role in etching of non-diamond carbon in these flames, but it is likely a much smaller role than in the flames at low specific flow rates.

At least two problems with the flame model predictions were observed. First, the flame model overpredicted the observed diamond film growth rate by an amount far larger than the uncertainty of the prediction. Second, the predicted maximum flame temperature was significantly above the adiabatic flame temperature, which is physically possible, but warrants investigation.

Hydrogen/oxygen flames with post-flame injection of methane offer the potential of a tightly controllable diamond growth environment at the substrate. A preliminary investigation of this technique was performed, and diamond was successfully grown under a variety of conditions. The deposit quality was found to vary significantly as a function of position in the deposit region, indicating a highly non-uniform chemical environment at the substrate for the chosen injection geometry.

Modeling and diagnostics were applied to the environment to investigate mixing

in the injection jet. The results suggest that the deposit size is limited by oxidation of the deposit by O_2 and OH in the post-flame gases. The variation in diamond quality in the deposit results from a strong non-uniformity of $[H]/[CH_3]$ ratio at the substrate surface, as well as a non-uniformity of oxidant concentrations at the substrate in the deposit region.

7.2 Suggestions for Future Work

Though diamond film growth conditions have been isolated, very little attempt has been made to optimize growth conditions for growth rate or diamond quality at the higher specific flow rates. The search area could be minimized by modeling a series of growth experiments and looking at growth rates and $[H]/[CH_3]$ ratios. Growth experiments could then be attempted only on the most promising cases.

However, before the results of the model can be taken seriously, some refinement of the model and verification of the model results should be performed. The most important measurement would be the spatial temperature profile in the gap between the burner and substrate. Such a measurement could easily be performed by LIF and would reveal whether or not the temperature is being severely overpredicted by the model. If it is, then the growth environment at the surface will be changed dramatically due to differing kinetics in the gas phase.

Also, including the temperature dependence of the reactions in the Harris mechanism would probably significantly improve the growth rate estimates by the mech-

anism for temperatures below 1200 K. For this, further experimental reaction rate data or computational estimates of reaction rates would be required.

Better data for the etch rate of diamond by O_2 would greatly assist the modeling efforts. The existing data of Sun and Alam [44] have a large uncertainty and are for temperatures slightly lower than common deposition temperatures. Data for the etch rates of diamond by OH and O at deposition temperatures would be of great value as well. This data might be obtained by placing a diamond substrate in a hydrogen/oxygen flame in a stagnation-point flow arrangement at low pressures ($<$ 10 Torr) and measuring surface [O], [OH], and [O_2] with molecular beam mass spectrometry.

The post-flame injection method has tremendous promise as a deposition technique, provided the requisite mixing can be achieved in order to provide a uniform chemical environment at the substrate surface. Since this study only investigated two potential injection geometries, it is quite possible that other injection geometries provide much more uniform growth environments. Further work in this area would likely be helpful in helping to determine whether this technique is a commercially viable option for diamond CVD.

Appendices

A Growth Run Data

The following table gives a listing of the growth runs and results for most of the growth runs performed in the Low Pressure Combustion Facility. Separate tables are given for acetylene/oxygen flames at low specific flow rates (less than 0.16 slm/cm^2 of burner surface), for acetylene/oxygen flames with cyclic variation of R, for acetylene/oxygen flames with high flow rates (0.94 slm/cm^2), and for hydrogen/oxygen flames with post-flame injection of methane/hydrogen mixtures.

Information in the tables is defined as follows. 'Date' is the date on which the experiment was performed, P is the system pressure in Torr, 'Flow' is the specific flow rate of fuel and oxidizer in slm per cm^2 of burner surface, D_S is the burner to substrate distance in mm, R is the ratio of oxygen to acetylene flow rates, and T_S is the substrate temperature in °C. Times are given in hours. For runs with cycling of R, t_1 is the period in seconds of the portion of the cycle in which $R = R_1$. Similarly, t_2 is the period is seconds of the portion of the cycle in which $R = R_2$.

Information on the deposit type, diamond size and quality, substrate surface appearance, and run problems for each run are listed under 'Comments.' Comment codes are given in the following table.

Comment Codes for Run Data

Deposit type

e etching environment; no deposit

ep etched diamond particles

d diamond deposit

nd non-diamond deposit

Surface appearance

b substrate has a blue tint

c substrate has a clear mirrored finish

Diamond quality

sn secondary nucleation on diamond

xsn heavy secondary nucleation on diamond

Diamond size

1 particles 1 – 5 microns in diameter

2 particles 6 – 10 microns in diameter

3 particles 11 – 15 microns in diameter

Run problems

fc mass flow controllers out of calibration tolerance

tt time varying T_S

st spatially varying T_S

A.1 Standard Acetylene/Oxygen Flames

	Nucl. Enh.		Run Conditions						
Date	R	Time	R	T_S	D_S	Flow	P	Time	Comments
8-5-91	1.0	0.5	1.35	925	6.0	0.126	40	6.0	d(2),b
8-6-91	1.0	0.5	1.30	860	6.0	0.126	40	5.0	e,c,b
10-31-91	1.0	0.5	1.32	975	15	0.164	40	6.0	nd
10-31-91	1.0	0.5	1.37	925	6.0	0.127	40	6.0	e,c
11-6-91	1.0	1.0	1.30	950	6.0	0.127	40	3.0	
			1.37	950	6.0	0.127	40	1.5	nd,e
11-7-91	1.0	0.5	1.25	975	6.0	0.127	40	3.0	
			1.37	975	6.0	0.127	40	3.0	nd
11-8-91	1.0	0.5	1.34	825	6.0	0.099	40	6.0	e,c
11-11-91	1.0	0.5	1.35	940	8.7	0.099	30	6.0	nd
11-12-91	1.0	0.5	1.40	935	8.7	0.092	30	6.0	nd
11-13-91			1.00	900	10	0.138	40	0.5	nd
11-14-91	1.0	0.3	1.45	935	8.7	0.127	30	6.5	nd
11-15-91	1.0	0.1	1.32	950	6.0	0.127	40	2.0	
			1.34	875	6.0	0.127	40	2.5	e,ep
11-18-91	1.0	0.3	1.34	940	6.0	0.127	40	5.0	nd,e
11-19-91	1.0	0.3	1.34	940	6.0	0.127	40	5.0	
			1.34	875	6.0	0.127	40	4.0	ep

	Nucl. Enh.		Run Conditions						
Date	R	Time	R	T_S	D_S	Flow	P	Time	Comments
11-20-91	1.0	0.3	1.20	937	5.0	0.127	60	4.0	nd,e
11-21-91	1.0	0.3	1.25	950	5.0	0.160	60	4.0	nd
11-22-91	1.0	0.3	1.30	950	5.0	0.156	60	2.5	nd
11-25-91	1.0	0.3	1.30	950	6.0	0.127	40	6.0	
			1.34	875	6.0	0.127	40	2.0	ep
11-26-91	1.0	0.3	1.20	860	6.5	0.127	40	5.0	nd,e
12-3-91	1.0	0.5	1.11	825	8.0	0.104	40	7.0	nd,e
12-5-91	1.0	0.5	1.11	825	8.0	0.104	40	7.5	nd,e
12-15-91	1.0	0.2	1.10	850	8.0	0.149	40	5.0	e,b
12-16-91	1.0	0.5	1.10	810	8.5	0.124	40	7.0	e,nd
12-19-91	1.0	0.4	1.10	830	7.5	0.124	40	2.0	ep
12-27-91	1.0	0.3	1.10	830	7.5	0.124	40	6.0	e,st
12-30-91	1.0	0.5	1.10	780	11	0.149	40	5.0	nd
1-6-92	1.0	0.3	1.10	825	11	0.149	40	6.0	nd
1-7-92	1.0	0.3	1.15	825	10	0.149	40	6.0	nd
8-31-92			1.30	940	6.3	0.126	40	11	d(1),b
9-3-92			1.20	950	7.3	0.126	40	2.0	
			1.30	950	7.3	0.126	40	6.0	nd,d(1)
9-4-92			1.22	950	7.3	0.126	40	1.0	
			1.30	950	7.3	0.126	40	7.0	d(1),b,tt,st

	Nucl. Enh.		Run Conditions						
Date	R	Time	R	T_S	D_S	Flow	P	Time	Comments
9-7-92			1.22	950	7.4	0.126	40	1.0	
			1.30	930	7.4	0.126	40	7.5	e,b,tt
9-8-92			1.20	960	7.2	0.126	40	1.5	
			1.30	950	7.2	0.126	40	8.0	e,b
9-10-92			1.22	950	7.0	0.126	40	1.0	
			1.26	950	7.0	0.126	40	7.5	ep,d(1),b
9-15-92			1.20	950	7.5	0.126	40	2.0	
			1.30	1000	6.7	0.126	40	5.5	e,b
9-17-92			1.22	960	7.5	0.126	40	3.0	
			1.23	950	7.5	0.126	40	2.0	
			1.27	970	7.2	0.158	40	4.0	nd,d(2),tt
9-21-92			1.20	950	6.7	0.159	40	4.0	d(1),c
9-22-92			1.15	950	7.5	0.159	40	0.8	
			1.20	950	7.5	0.159	40	5.0	e,b
9-29-92			1.15	950	7.5	0.159	40	0.5	
			1.20	950	7.5	0.159	40	5.0	d(1)
10-2-92			1.15	970	7.1	0.159	40	0.3	
			1.20	960	7.1	0.159	40	6.0	nd,d(1),st
10-31-92			1.14	980	11	0.159	40	?	
			1.33	980	11	0.159	40	?	e,d(1)

	Nucl. Enh.		Run Conditions						
Date	R	Time	R	T_S	D_S	Flow	P	Time	Comments
12-11-92			1.30	970	8.0	0.159	40	5.0	d(2,sn,xsn)
12-18-92			1.30	960	8.4	0.159	40	0.3	
			1.40	960	8.4	0.159	40	2.8	ep
1-8-93			1.30	967	8.0	0.159	40	0.3	
			1.34	967	8.0	0.159	40	7.0	d(2)
1-11-93			1.22	960	8.7	0.159	40	0.8	
			1.35	960	8.0	0.159	40	3.5	e,ep, fc
1-11-93			1.20	960	9.0	0.159	40	0.8	
			1.28	960	8.5	0.159	40	3.5	nd,e
1-13-93			1.34	960	7.7	0.159	40	0.4	fc
			1.39	960	7.7	0.159	40	3.5	nd,fc
1-18-93			1.25	975	8.6	0.159	40	0.6	
			1.33	975	8.6	0.159	40	3.5	nd,fc
1-19-93			1.25	965	8.7	0.159	40	0.6	
			1.35	965	8.7	0.159	40	5.0	nd,d,st
1-20-93			1.25	967	8.7	0.159	40	0.5	
			1.38	967	8.7	0.159	40	2.0	nd,d(xsn))
1-21-93			1.25	967	9.0	0.159	40	0.6	
			1.40	967	9.0	0.159	40	4.5	d(1,sn)
5-28-93			1.30	950	9.0	0.203	40	3.5	e

	Nucl. Enh.		Run Conditions						
Date	R	Time	R	T_S	D_S	Flow	P	Time	Comments
5-31-93			1.20	950	7.5	0.203	40	3.8	nd
6-1-93			1.25	980	7.5	0.203	40	3.5	nd,d,st
6-2-93			1.25	1025	6.8	0.203	40	2.3	nd,d
1-29-94			1.29	955	7.5	0.127	35	3.0	d(xsn)
1-31-94			1.35	940	7.5	0.127	35	4.1	d(xsn)
2-1-94			1.38	950	7.5	0.127	35	3.3	d(xsn)
2-2-94			1.20	850	8.5	0.127	35	3.0	nd
2-2-94			1.30	850	7.5	0.127	35	3.5	e
2-3-94			1.25	850	7.5	0.127	35	3.3	d(sn)
2-7-94			1.35	950	11	0.127	35	1.3	nd

A.2 Runs with Cycling of Oxygen/Acetylene Ratio

Date	R_1	R_2	t_1/t_2	T_S	D_S	Flow	P	Time	Comments
8-24-92	1.25	1.40	105/15	955	6.3	0.127	40	6.0	d(1)
12-16-92	1.30			950	7.9	0.159	40	0.3	
	1.30	1.40	60/10	950	8.0	0.159	40	3.5	d(1,xsn)
12-21-92	1.30			960	8.5	0.159	40	0.3	
	1.30	1.40	30/10	960	8.5	0.159	40	3.5	d(1,xsn)
12-22-92	1.30			960	8.5	0.159	40	0.2	
	1.34	1.40	30/10	960	8.5	0.159	40	5.0	d(1)
12-24-92	1.30			960	8.5	0.159	40	0.2	
	1.34	1.40	29/10	960	8.5	0.159	40	9.0	d(2,sn)
12-28-92	1.30			970	8.5	0.159	40	0.2	
	1.34	1.40	30/10	970	8.5	0.159	40	4.0	d(2,sn)
1-4-92	1.30			970	8.7	0.159	40	0.2	
	1.35	1.40	30/10	970	8.7	0.159	40	3.0	
	1.35	1.40	20/20	970	8.7	0.159	40	3.0	d(2,sn)
1-4-92	1.25			970	8.7	0.159	40	0.6	
	1.40			970	8.7	0.159	40	0.3	
	1.35	1.40	20/10	970	8.7	0.159	40	2.2	d(1)

A.3 C_2H_2/O_2 Flames at High Flow Rates

In all runs, $P = 52$ Torr, $D_S = 1.0$ cm, and the specific flow rate is 0.939 slm/cm^2. All deposits showed some form of diamond except where noted with an 'nd.' The

temperatures shown are the minimum and maximum run temperatures.

Date	R	T_S	Time	Comments
7-8-93	1.150	980–1020	2.5	tt
7-9-93	1.125	900–1000	5.0	tt
7-12-93	1.150	970	3.0	tt
7-14-93	1.150	825–1025	4.0	st,tt
7-15-93	1.150	825–1025	2.2	st,tt
7-23-93	1.150	760–890	3.3	st,tt
7-26-93	1.165	775–800	3.8	tt
10-8-93	1.165	870–1020	3.1	tt
10-20-93	1.165	850–940	5.6	tt
11-4-93	1.165	925–1090	3.5	tt,nd
11-6-93	1.165	865–965	2.8	tt
11-10-93	1.165	850–940	5.5	tt
11-24-93	1.165	860	3.5	
1-5-94	1.165	860	4.3	

A.4 Post-flame injection runs

For runs using post-flame injection of methane/hydrogen mixtures, '% CH_4' denotes the mole fraction of methane in hydrogen in the injected gas. D_i is the distance from the injection tube outlet to the substrate in mm. $D_i = 0$ implies horizontal injection at the substrate surface. '$H_2/C_2H_2/O_2$' are the flow rates of fuels and oxidizer into the

premixed flame in standard liters per minute. The flow rate of the injected mixture was 0.2 slm except for the case noted 'hf' in which the flow rate was 0.5 slm. For runs in which nucleation enhancement was used early in the run to increase nucleation density, 'ne' appears in the 'Comments' column.

Date	$H_2/C_2H_2/O_2$	% CH_4	T_S	D_i	D_S	P	Time	Comments
1-9-92	6.0/0.0/2.7	5.0	850	0	40	40	4.9	e,b,fc
1-10-92	6.0/0.0/2.7	0.5	850	0	40	40	6.4	nd
1-13-92	6.8/0.0/2.9	0.5	885	0	25	40	6.5	d(1,2,sn,xsn)
1-14-92	4.0/0.0/1.65	0.5	755	0	30	36	6.3	nd
1-16-92	5.25/0.0/2.25	0.5		0	20	35	4.1	nd
1-22-92	3.75/0.0/1.5	0.5	935	0	33	36	5.8	d(1)
1-23-92	3.75/0.0/1.5	0.5	930	0	33	36	6.1	nd
1-24-92	3.75/0.0/1.5	0.5	930	0	50	46	6.9	d(1,sn)
1-28-92	3.75/0.0/1.5	0.5	930	0	50	46	14.5	d(1,2)
2-11-92	3.0/0.0/1.2	0.5	950	0	44	46	5.9	nd
2-14-92	2.0/0.0/0.8	0.5	900	0	42	40	6.3	nd

Date	$H_2/C_2H_2/O_2$	% CH_4	T_S	D_i	D_S	P	Time	Comments
2-17-92	3.0/0.25/1.2	0.5	930	0	40	36	7.2	d(1)
2-18-92	3.0/0.25/1.2	0.5	920	0	40	50	6.5	nd
2-20-92	4.0/0.33/1.6	0.5	930	0	40	36	13.4	d(1,sn,xsn),nd
2-27-92	4.0/0.33/1.6	0.5	775	0	40	36	6.8	e,c
3-2-92	4.0/0.33/1.6	0.5	805	0	40	36	5.9	e,c
3-3-92	4.0/0.33/1.6	0.5	850	0	40	36	6.4	d(1,sn,xsn),nd
3-4-92	4.0/0.33/1.6	1.0	950	0	40	36	5.8	nd,tt
3-27-92	4.0/0.33/1.6	0.5	935	1	22	35	7.1	nd
3-30-92	4.0/0.33/1.6	5.0	930	8	21	35	6.0	nd
3-31-92	4.0/0.33/1.6	0.5	930	8	21	35	8.0	e,b,d(1)
4-2-92	4.0/0.33/1.6	0.5	880	3	51	35	7.0	d(1,sn,xsn)
4-7-92	4.0/0.33/1.6	0.5	880	4	51	35	7.7	hf,nd
4-10-92	4.0/0.33/1.6	0.5	880	3	51	35	6.8	ne,d(1,sn,xsn)
4-14-92	4.0/0.33/1.6	0.5	880	3	51	35	8.9	ne,d(1,sn,xsn)
4-15-92	4.0/0.33/1.6	0.5	880	3	51	35	6.6	ne,d(1,sn,xsn)
4-21-92	4.0/0.33/1.6	0.5	930	2	51	35	4.5	ne,nd
4-30-92	4.0/0.33/1.6	0.5	980	3	51	35	13.5	ne

B Burner Design

Two different burner designs were used to produce low pressure flat flames for the deposition experiments. The original burner was a porous plug flat flame burner (McKenna Products, Pittsburg, Ca.). The burner face was a sintered brass disk which had embedded inside it a coil of copper tubing for water cooling. In an annulus around the burner face was a sintered brass ring through which a shield gas could flow.

The flame produced by the sintered brass burner was extremely uniform and stable. However, during runs with rich acetylene/oxygen mixtures, the burner became clogged with carbon deposits, destroying the uniformity of the flame front. In addition, these carbon deposits were extremely difficult to remove. Also, at higher specific flow rates, the heat flux to the burner became great enough to anneal the brass plug and the stainless steel tube into which it was press fit. After annealing, flow of premixed gases was able to escape around the sintered brass disk, and the uniformity of the flame was again destroyed.

To alleviate these problems, a new burner was designed and built. The design is based loosely on that of Bittner [30]. The burner is a cylinder with a radius of approximately 6 cm and a height of 10 cm. At one end of the cylinder is the burner face, and at the other end are pipe fittings which allow cooling water and premixed gases to enter the burner. The burner face is a 0.5% tellurium-copper plate (12 mm thick) with an array of 559 1 mm diameter holes drilled in it. The holes are spaced in an hexagonal array with a distance between hole centers of 2.5 mm. The copper

disk is press fit into the end of a stainless steel tube. A cross-section of the burner design is shown in Figure 1.

The flow straightener is an aluminum disk (12 mm thick) drilled with the same array of holes as the burner face. The flow straightener is set in place with a slip fit inside the stainless steel tube approximately 10 mm above the burner face.

The aluminum cooling core is a two piece welded design which allows water to cool the top 4 cm of the stainless steel tube. It is press fit for optimal thermal contact into the top end of the tube.

The radial thermal resistance in the thick copper disk is extremely low as compared to the thermal resistance up the thin stainless steel walls. Therefore, the temperature profile across the burner face is relatively flat. Also, the burner operates at an elevated surface temperature. Burner surface temperatures of up to 1000 K were measured with a thermocouple placed in a hole near the array center. The high burner surface temperatures place an upper limit on range of usable specific flow rates. For this burner, specific flow rates of 0.159 slm/cm^2 in rich acetylene/oxygen flames produced surface temperatures above the design limit.

To explore the higher specific flow rates, a second burner was constructed. The design is basically the same except that the hole array is only 4 cm in diameter, and the stainless steel tube and copper disk are replaced by a single copper piece. The flow straightener and the aluminum core are identical to those used in the previous model. The copper walls have much lower thermal resistance than stainless steel, and thus the burner surface temperature is reduced significantly.

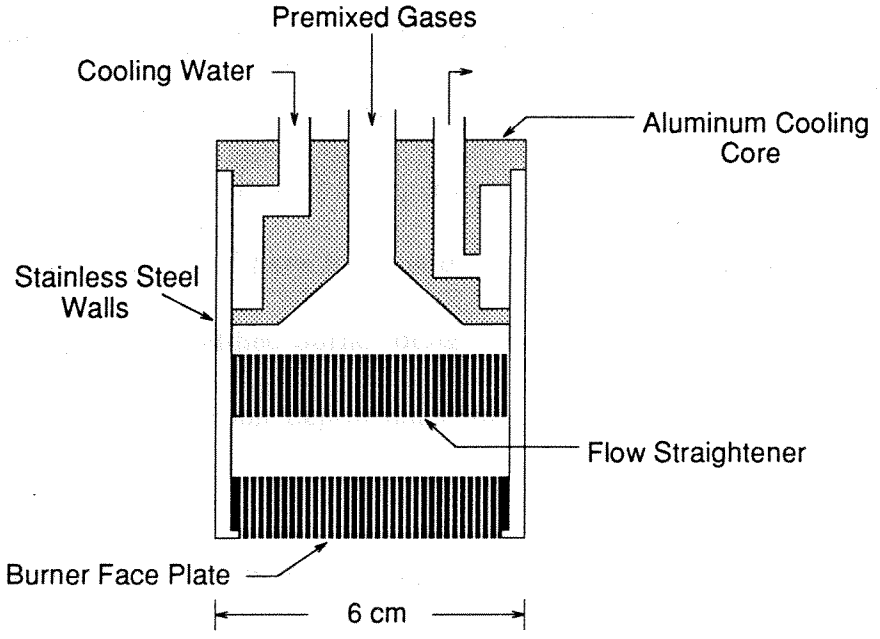

Figure 1: Cross section of the flat flame burner.

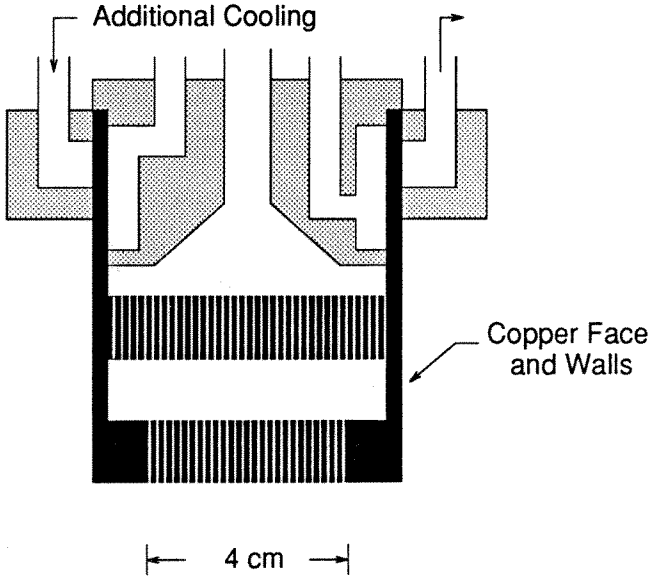

Figure 2: The modified flat flame burner for high flow rates.

Since the modified burner is designed to operate at specific flow rates nearly an order of magnitude larger than the original model, additional cooling is required. An external aluminum cooling jacket is added to the top 2.5 cm of the copper tube and provides the necessary additional heat removal. With the modified burner, specific flow rates of 0.939 slm/cm^2 have been used, and yet the burner surface temperature is only $\sim$ 500 K. The modified burner design is shown in Figure 2.

Though much less carbon deposition is observed on the drilled copper burners than on the sintered brass burner, in rich acetylene/oxygen flames significant carbon is deposited within the holes of the copper disk during each run. After roughly 75 hours of run time, some non-uniformity in the flame front can be observed due to blockage of the flow. However, both drilled copper burners are cleanable in less than 1 hour by redrilling the holes using a slightly undersize drill bit and a hand-held electric drill.

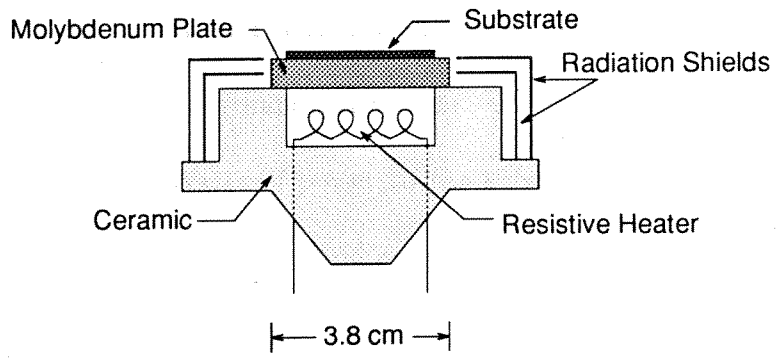

Figure 3: The original substrate holder.

C Substrate Holder Design

C.1 Nichrome-based Substrate Heaters

Several different substrate holder designs were used in this work. With the exception of the substrates used in the high specific flow rate acetylene/oxygen flames, all substrates required some form of heating in order to achieve growth temperatures (1100 - 1300 K).

The substrate holder originally used to heat substrates in acetylene/oxygen flames used a Nichrome (80% Ni, 20% Cr) resistive heating element to provide heat for the substrate. Figure 2 is a schematic of the substrate holder. The heating element was embedded in a ceramic cavity below a thick (6 mm) molybdenum plate. The plate was thick enough to insure that temperature non-uniformities at the top surface were less than 50 K. Molybdenum radiation shields reduced the radiative losses to the cold vacuum chamber walls.

Silicon substrates were placed on top of the molybdenum plate. To improve thermal contact, a thin layer of MoS_2 or copper-containing grease was placed between

the substrate and plate. Nevertheless, the surface temperatures often varied by more than 100 K due to uneven thermal contact. The resistive heating element was capable of providing up to ~300 Watts of power to the substrate. With this range of input powers, the substrate temperature could be varied over a 150 K range. The maximum achievable temperature depended on the flame parameters R, specific flow rate, P, and D_S. The highest temperature attained with this heater was 1260 K.

Due to the limited T_S range of the original design and the large temperature variation across the substrate, a new substrate holder was designed for use in the low specific flow rate acetylene/oxygen flames. The second design is shown in Figure 3. With the new holder, the molybdenum plate itself served as the substrate. The temperature non-uniformities were reduced to below 50 K across the substrate by eliminating the contact resistance. The new design also had a larger heating element, improved radiation shielding, reduced conduction losses to its supports, and a flatter, more uniform top surface. With the improved design and increased power input (> 400 W), T_S could be easily varied over a 250 K range, and substrate temperatures of 1300 K were possible in nearly all flames

C.2 The Resistive Heater

To allow for control of T_S independent of other flame parameters, the substrate was heated directly in a series of experiments by passing current through it. A schematic of the resistive heating substrate holder is shown in Figure 4. A silicon wafer was cut into rectangular pieces with dimensions 2.5 cm × 5 cm. The ends of the silicon

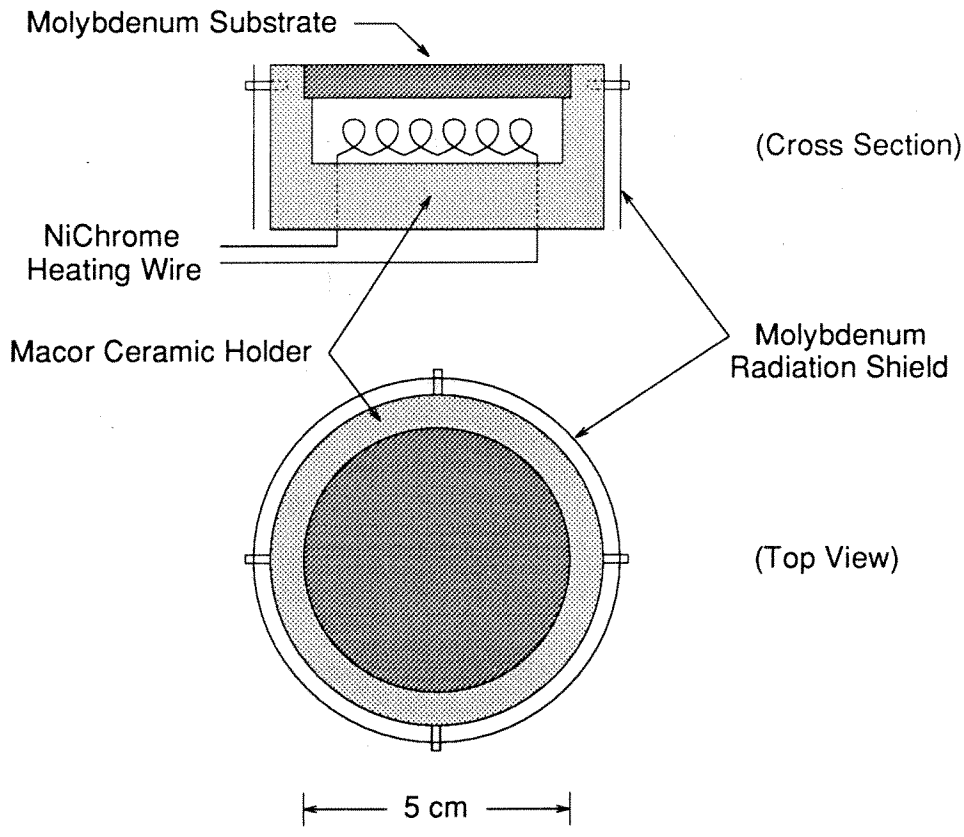

Figure 4: The improved design of the original substrate holder.

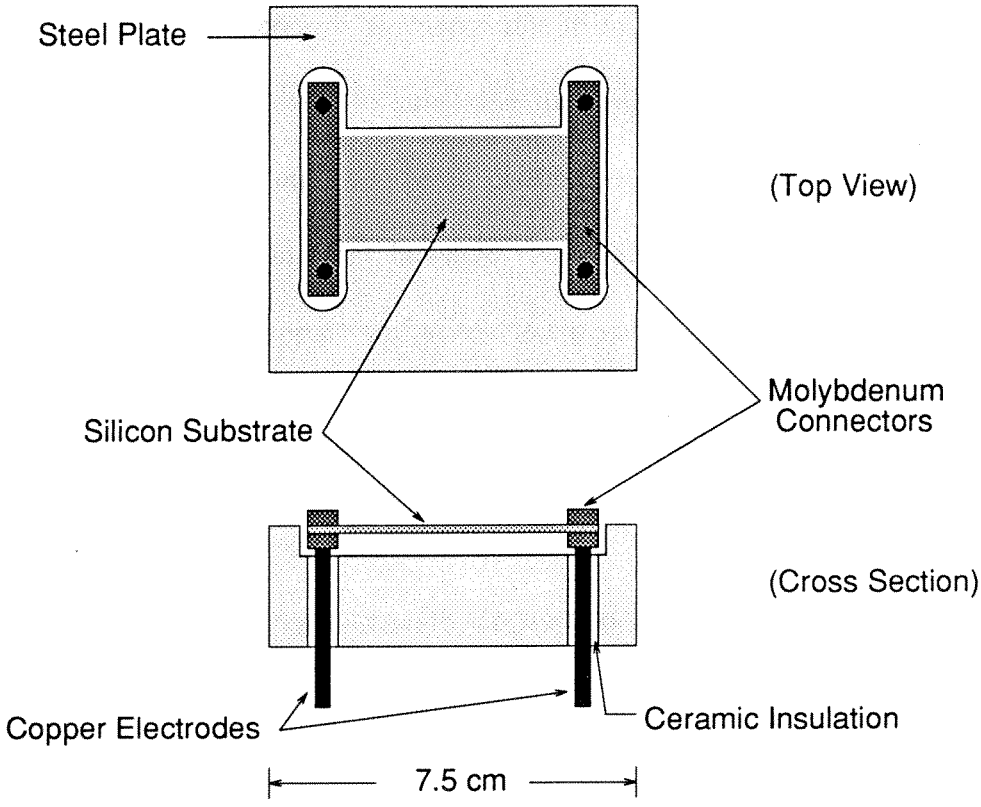

Figure 5: Substrate holder for resistive heating of silicon substrates.

substrate were clamped into molybdenum connectors which were attached to copper electrodes. Under ideal circumstances, the electrical contact between the silicon and molybdenum was uniform, and the passage of current through the substrate resulted in a uniform temperature over a central 3.5 cm $\times$ 2.5 cm area. Near the electrical connectors, the temperature dropped significantly due to conduction losses. The current passing through the substrate could be varied arbitrarily up to the point at which the silicon melted. Thus, great control over the substrate temperature was possible.

Though the control over the T_S was excellent, uniform electrical contact at the substrate ends was difficult to achieve at the high temperatures due to the brittle

nature of the silicon. Therefore, in many runs using this heater, the substrate temperature was not uniform over the substrate. In addition, the rather bulky electrical contacts at the substrate ends produced obstructions which made the flow deviate from the desired stagnation-point flowfield. Near the center of the substrate where the T_S was most uniform, the perturbations to the stagnation-point flowfield were the smallest. Thus, in runs in which the electrical contact was uniform, uniform deposits were observed in the central region of the substrate.

C.3 Heaters for Post-flame Injection

For the post-flame injection experiments, the heat flux from the hydrogen post-flame gases to the substrate was extremely small. Thus, the substrates required large amounts of heat to attain deposition temperatures. For these experiments, the substrate heating setup shown in Figure 5 was used. A 250 μm thick molybdenum strip was used as the resistive heater. A rectangular silicon substrate (0.5 cm $\times$ 2 cm) was cemented to the molybdenum strip using ceramic cement. The electrical resistance of both the cement and the silicon substrate were significantly higher than that of the molybdenum strip. Currents of up to 70 A (@ $\sim$6 V) were passed through the molybdenum strip, and the temperature of the silicon substrate was again controllable up to its melting point. The deviations in T_S across the silicon were usually much less than 50 K.

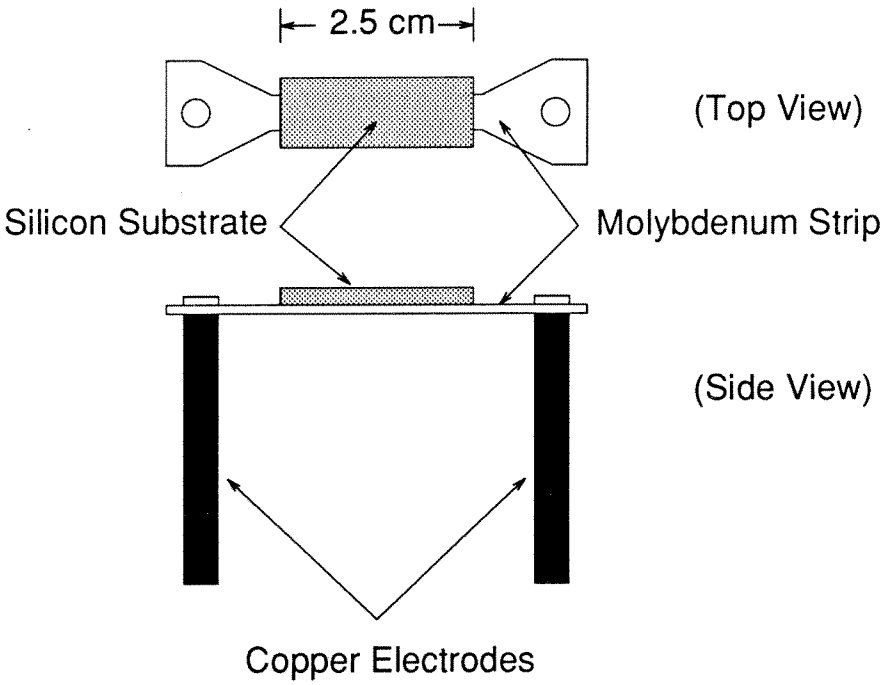

Figure 6: Substrate heater used in post-flame injection experiments. The substrate is held in place with ceramic cement.

D Surface Chemistry Mechanism

The surface chemistry mechanism used in the flame model is listed in Tables 1 and 2. The model assumes a surface site density of 3×10^{-9} moles/cm^2. Eight different surface site types are assumed to be present at the surface.

The units of A are cm^3/mol/sec and E_A is given in kcal/mol. Rates are given in terms of the sticking probability for reactions with 'Stick' in the 'Comments' column. 'Fast' denotes that the reaction rate is set high enough such that the reaction is not the rate limiting step in the mechanism.

As described in Chapter 3, C_dH represents a hydrogen terminated site, C_d* an active site, C_dM an adsorbed methyl radical, and C_dM* a C_dM site after abstraction of one hydrogen atom.

Reactions 1 and 2 represent hydrogen abstraction from the surface by H and filling of active sites by H. Together these reactions yield a recombination probability for H on diamond. The reaction rate data for these two reactions were chosen to match the measured sticking probability for recombination of H on diamond (γ_H) at 1200 K and the observed temperature dependence of (γ_H) at high temperatures ($E_A = 6.0$ kcal/mol) [43]. Reactions 1–6 represent the reduced Harris mechanism for diamond growth after Goodwin [12].

Reactions 7 and 8 account for recombination of O and OH radicals at the surface by hydrogen abstraction. Details are given in Chapter 3.

Reactions 9 and 10 account for diamond etching by O_2 with an empirical fit to the experimental data of Sun and Alam [44].

Etching of diamond by OH and O is estimated in the upper limit by reactions 11 and 12. A single carbon atom is assumed to be etched into the gas phase each time an OH or O radical strikes an active site.

Reactions 13–15 allow recombination of C at the surface through the intermediate sites SA and SB. The mechanism is not intended to be a physical representation of the recombination process, but rather a means to avoid non-physical excesses of C radicals at the substrate surface. The overall reaction for this recombination is:

$$2C + H_2 + C_dH \rightarrow C_2H_2 + C_dH \quad (1)$$

Reactions 16 and 17 similarly account for recombination of CH at the surface through an intermediate site SD. The overall reaction is:

$$2CH + C_dH \rightarrow C_2H_2 + C_dH \quad (2)$$

Reactions 18–21 account for recombination of CH_2 at the surface in the same manner through the intermediate site SE. The overall reaction is:

$$2CH_2 + C_dH \rightarrow C_2H_4 + C_dH \quad (3)$$

No.	Reaction	A	n	E_A	Comments
1.	$C_dH + H \rightleftharpoons C_d^* + H_2$	5.06E13	0	6.84	ΔG:-16.0
2.	$C_d^* + H \rightarrow C_dH$	0.43	0	0.0	Stick
3.	$C_d^* + CH_3 \rightarrow C_dM$	3.3E12	0	0.0	
4.	$C_dM \rightarrow C_d^* + CH_3$	1.E4	0	0.0	
5.	$C_dM + H \rightarrow C_dM^* + H_2$	2.E12	0	0.0	
6.	$C_dM^* + H \rightarrow C_dH + H_2$	1.E16	0	0.0	
7.	$C_dH + OH \rightleftharpoons C_d^* + H_2O$	2.47E6	2.152	0.3217	ΔG:-31.14
8.	$C_dH + O \rightleftharpoons C_d^* + OH$	2.14E5	2.5	0.924	ΔG:-19.74
9.	$C_dH + O_2 \rightarrow CO_2 + C_dH$	2.1E16	0	54.7	Order in O_2: 0.6
10.	$C_d^* + O_2 \rightarrow CO_2 + C_d^*$	2.1E16	0	54.7	Order in O_2: 0.6
11.	$C_d^* + OH \rightarrow CO + C_dH$	1.0	0	0.0	Stick
12.	$C_d^* + O \rightarrow C_d^* + CO$	1.0	0	0.0	Stick

Table 1: Reactions 1–12 in the surface chemistry mechanism.

No.	Reaction	A	n	E_A	Comments
13.	$C + C_dH \rightarrow SA$	1.0	0	0.0	Stick
14.	$C + SA \rightarrow SB$	1.0E17	0	0.0	Fast
15.	$H_2 + SB \rightarrow C_dH + C_2H_2$	1.0E17	0	0.0	Fast
16.	$CH + C_dH \rightarrow SD$	1.0	0	0.0	Stick
17.	$CH + SD \rightarrow C_dH + C_2H_2$	1.0E17	0	0.0	Fast
18.	$CH_2 + C_dH \rightarrow SE$	1.0	0	0.0	Stick
19.	$CH_2 + SE \rightarrow C_2H_4 + C_dH$	1.0E17	0	0.0	Fast
20.	$CH_2(S) + C_dH \rightarrow SE$	1.0	0	0.0	Stick
21.	$CH_2(S) + SE \rightarrow C_2H_4 + C_dH$	1.0E17	0	0.0	Fast

Table 2: Reactions 13–21 in the surface chemistry mechanism.

E Gas Phase Chemistry Mechanism

The gas phase chemistry mechanism is that of Miller and Melius [37], and is listed in this appendix. The reaction rates are given in the form:

$$k = A\,T^n\,exp[-E_A/RT] \tag{4}$$

The units for A are $cm^3/mol/sec$, and E_A is given in kcal/mol. The following 49 species are considered in the model:

Monatomic species: H, O, C, Ar

Homonuclear diatomics: H_2, O_2, C_2

H-O compounds: OH, HO_2, H_2O, H_2O_2

C-O compounds: CO, CO_2, C_2O

C_1 hydrocarbons: CH, CH_2, CH_2^1, CH_3, CH_4

C_2 hydrocarbons: C_2H, C_2H_2, C_2H_3, C_2H_4, C_2H_5, C_2H_6

C_3 hydrocarbons: C_3H_2, H_2CCCH, C_3H_4, C_3H_4P

C_4 hydrocarbons: C_4H_2, H_2CCCCH, $HCCHCCH$, CH_2CHCCH, $CH_2CHCHCH_2$, $CH_2CHCHCH$, CH_2CHCCH_2

C_5 hydrocarbons: C_5H_2, C_5H_3

C_6 hydrocarbons: C_6H_2, C_6H_5, C_6H_6

H-C-O compounds: HCO, HCCO, HCCOH, CH_2O, CH_3O, CH_2OH, C_6H_5O, H_2C_4O

No.	Reaction	A	n	E_a
1.	$H_2 + O_2 = 2OH$	0.170E+14	0.000	47780.000
2.	$OH + H_2 = H_2O + H$	0.117E+10	1.300	3626.000
3.	$O + OH = O_2 + H$	0.400E+15	-0.500	0.000
4.	$O + H_2 = OH + H$	0.506E+05	2.670	6290.000
5.	$H + O_2 + M = HO_2 + M$	0.361E+18	-0.720	0.000
	3rd body efficiencies: H_2O: 18.6, CO_2: 4.2, H_2: 2.86, CO: 2.11			
7.	$OH + HO_2 = H_2O + O_2$	0.750E+13	0.000	0.000
8.	$H + HO_2 = 2OH$	0.140E+15	0.000	1073.000
9.	$O + HO_2 = O_2 + OH$	0.140E+14	0.000	1073.000
10.	$2OH = O + H_2O$	0.600E+09	1.300	0.000
11.	$H + H + M = H_2 + M$	0.100E+19	-1.000	0.000
	3rd body efficiencies: H_2O: 0.0, H_2: 0.0, CO_2: 0.0			
12.	$H + H + H_2 = H_2 + H_2$	0.920E+17	-0.600	0.000
13.	$H + H + H_2O = H_2 + H_2O$	0.600E+20	-1.250	0.000
14.	$H + H + CO_2 = H_2 + CO_2$	0.549E+21	-2.000	0.000
15.	$H + OH + M = H_2O + M$	0.160E+23	-2.000	0.000
	3rd body efficiency: H_2O: 5			
16.	$H + O + M = OH + M$	0.620E+17	-0.600	0.000
	3rd body efficiency: H_2O: 5			
17.	$O + O + M = O_2 + M$	0.189E+14	0.000	-1788.000
18.	$H + HO_2 = H_2 + O_2$	0.125E+14	0.000	0.000
19.	$HO_2 + HO_2 = H_2O_2 + O_2$	0.200E+13	0.000	0.000
20.	$H_2O_2 + M = OH + OH + M$	0.130E+18	0.000	45500.000
21.	$H_2O_2 + H = HO_2 + H_2$	0.160E+13	0.000	3800.000
22.	$H_2O_2 + OH = H_2O + HO_2$	0.100E+14	0.000	1800.000
23.	$CH_3 + CH_3(+M) = C_2H_6(+M)$	9.030E+16	-1.200	654.000
	Low Pressure limit: 3.180E41 -7.000 2762.0			
	Troe: 0.604 6927. 132.			
	3rd body efficiencies: H_2: 2, CO: 2, CO_2: 3, H_2O: 5			
24.	$CH_3 + H(+M) = CH_4(+M)$	6.00E16	-1.000	0.000
	Low Pressure limit: 8.0E26 -3.0 0.0			
	SRI: 0.45 797. 979.			
	3rd body efficiencies: H_2: 2, CO: 2, CO_2: 3, H_2O: 5			
25.	$CH_4 + O_2 = CH_3 + HO_2$	0.790E+14	0.000	56000.000
26.	$CH_4 + H = CH_3 + H_2$	0.220E+05	3.000	8750.000
27.	$CH_4 + OH = CH_3 + H_2O$	0.160E+07	2.100	2460.000
28.	$CH_4 + O = CH_3 + OH$	1.020E+09	1.500	8604.000
29.	$CH_4 + HO_2 = CH_3 + H_2O_2$	0.180E+12	0.000	18700.000
30.	$CH_3 + HO_2 = CH_3O + OH$	0.200E+14	0.000	0.000
31.	$CH_3 + O = CH_2O + H$	8.000E+13	0.000	0.000
32.	$CH_3 + O_2 = CH_3O + O$	0.205E+19	-1.570	29229.000
33.	$CH_2OH + H = CH_3 + OH$	0.100E+15	0.000	0.000
34.	$CH_3O + H = CH_3 + OH$	0.100E+15	0.000	0.000
35.	$CH_3 + OH = CH_2 + H_2O$	0.750E+07	2.000	5000.000
36.	$CH_3 + H = CH_2 + H_2$	0.900E+14	0.000	15100.000
37.	$CH_3O + M = CH_2O + H + M$	0.100E+15	0.000	25000.000
38.	$CH_2OH + M = CH_2O + H + M$	0.100E+15	0.000	25000.000
39.	$CH_3O + H = CH_2O + H_2$	0.200E+14	0.000	0.000
40.	$CH_2OH + H = CH_2O + H_2$	0.200E+14	0.000	0.000
41.	$CH_3O + OH = CH_2O + H_2O$	0.100E+14	0.000	0.000
42.	$CH_2OH + OH = CH_2O + H_2O$	0.100E+14	0.000	0.000
43.	$CH_3O + O = CH_2O + OH$	0.100E+14	0.000	0.000

No.	Reaction	A	n	E_a
44.	$CH_2OH + O = CH_2O + OH$	0.100E+14	0.000	0.000
45.	$CH_3O + O_2 = CH_2O + HO_2$	0.630E+11	0.000	2600.000
46.	$CH_2OH + O_2 = CH_2O + HO_2$	0.148E+14	0.000	1500.000
47.	$CH_2 + H = CH + H_2$	0.100E+19	-1.560	0.000
48.	$CH_2 + OH = CH + H_2O$	0.113E+08	2.000	3000.000
49.	$CH_2 + OH = CH_2O + H$	0.250E+14	0.000	0.000
50.	$CH + O_2 = HCO + O$	0.330E+14	0.000	0.000
51.	$CH + O = CO + H$	0.570E+14	0.000	0.000
52.	$CH + OH = HCO + H$	0.300E+14	0.000	0.000
53.	$CH + OH = C + H_2O$	4.000E+07	2.000	3000.000
54.	$CH + CO_2 = HCO + CO$	0.340E+13	0.000	690.000
55.	$CH + H = C + H_2$	0.150E+15	0.000	0.000
56.	$CH + H_2O = CH_2O + H$	1.170E+15	-0.750	0.000
57.	$CH + CH_2O = CH_2CO + H$	0.946E+14	0.000	-515.000
58.	$CH + C_2H_2 = C_3H_2 + H$	0.100E+15	0.000	0.000
59.	$CH + CH_2 = C_2H_2 + H$	0.400E+14	0.000	0.000
60.	$CH + CH_3 = C_2H_3 + H$	0.300E+14	0.000	0.000
61.	$CH + CH_4 = C_2H_4 + H$	0.600E+14	0.000	0.000
62.	$C + O_2 = CO + O$	0.200E+14	0.000	0.000
63.	$C + OH = CO + H$	0.500E+14	0.000	0.000
64.	$C + CH_3 = C_2H_2 + H$	0.500E+14	0.000	0.000
65.	$C + CH_2 = C_2H + H$	0.500E+14	0.000	0.000
66.	$CH_2 + CO_2 = CH_2O + CO$	0.110E+12	0.000	1000.000
67.	$CH_2 + O = CO + H + H$	0.500E+14	0.000	0.000
68.	$CH_2 + O = CO + H_2$	0.300E+14	0.000	0.000
69.	$CH_2 + O_2 = CO_2 + H + H$	0.160E+13	0.000	1000.000
70.	$CH_2 + O_2 = CH_2O + O$	0.500E+14	0.000	9000.000
71.	$CH_2 + O_2 = CO_2 + H_2$	0.690E+12	0.000	500.000
72.	$CH_2 + O_2 = CO + H_2O$	0.190E+11	0.000	-1000.000
73.	$CH_2 + O_2 = CO + OH + H$	0.860E+11	0.000	-500.000
74.	$CH_2 + O_2 = HCO + OH$	0.430E+11	0.000	-500.000
75.	$CH_2O + OH = HCO + H_2O$	0.343E+10	1.180	-447.000
76.	$CH_2O + H = HCO + H_2$	0.219E+09	1.770	3000.000
77.	$CH_2O + M = HCO + H + M$	0.331E+17	0.000	81000.000
78.	$CH_2O + O = HCO + OH$	0.180E+14	0.000	3080.000
79.	$HCO + OH = H_2O + CO$	0.100E+15	0.000	0.000
80.	$HCO + M = H + CO + M$	0.250E+15	0.000	16802.000
	3rd body efficiencies: CO: 1.87, H_2: 1.87, CH_4: 2.81, CO_2: 3., H_2O: 5.			
81.	$HCO + H = CO + H_2$	0.119E+14	0.250	0.000
82.	$HCO + O = CO + OH$	0.300E+14	0.000	0.000
83.	$HCO + O = CO_2 + H$	0.300E+14	0.000	0.000
84.	$HCO + O_2 = HO_2 + CO$	0.330E+14	-0.400	0.000
85.	$CO + O + M = CO_2 + M$	0.617E+15	0.000	3000.000
86.	$CO + OH = CO_2 + H$	0.151E+08	1.300	-758.000
87.	$CO + O_2 = CO_2 + O$	2.53E+12	0.000	47688.000
88.	$HO_2 + CO = CO_2 + OH$	0.580E+14	0.000	22934.000
89.	$C_2H_6 + CH_3 = C_2H_5 + CH_4$	0.550E+00	4.000	8300.000
90.	$C_2H_6 + H = C_2H_5 + H_2$	0.540E+03	3.500	5210.000
91.	$C_2H_6 + O = C_2H_5 + OH$	0.300E+08	2.000	5115.000
92.	$C_2H_6 + OH = C_2H_5 + H_2O$	0.870E+10	1.050	1810.000
93.	$C_2H_4 + H = C_2H_3 + H_2$	0.110E+15	0.000	8500.000
94.	$C_2H_4 + O = CH_3 + HCO$	0.160E+10	1.200	746.000
95.	$C_2H_4 + OH = C_2H_3 + H_2O$	0.202E+14	0.000	5955.000

No.	Reaction	A	n	E_a
96.	$CH_2 + CH_3 = C_2H_4 + H$	0.400E+14	0.000	0.000
97.	$H + C_2H_4(+M) = C_2H_5(+M)$	0.221E+14	0.000	2066.000
	Low Pressure limit: 6.369E27 -2.76 -54.0			
	3rd body efficiencies: H_2: 2, CO: 2, CO_2: 3, H_2O: 5			
98.	$C_2H_5 + H = CH_3 + CH_3$	1.000E+14	0.000	0.000
99.	$C_2H_5 + O_2 = C_2H_4 + HO_2$	0.843E+12	0.000	3875.000
100.	$C_2H_2 + O = CH_2 + CO$	0.102E+08	2.000	1900.000
101.	$C_2H_2 + O = HCCO + H$	0.102E+08	2.000	1900.000
102.	$H_2 + C_2H = C_2H_2 + H$	0.409E+06	2.390	864.300
103.	$H + C_2H_2(+M) = C_2H_3(+M)$	0.554E+13	0.000	2410.000
	Low Pressure limit: 2.67E27 -3.5 2410.			
	3rd body efficiencies: H_2: 2, CO: 2, CO_2: 3, H_2O: 5			
104.	$C_2H_3 + H = C_2H_2 + H_2$	0.400E+14	0.000	0.000
105.	$C_2H_3 + O = CH_2CO + H$	0.300E+14	0.000	0.000
106.	$C_2H_3 + O_2 = CH_2O + HCO$	0.400E+13	0.000	-250.000
107.	$C_2H_3 + OH = C_2H_2 + H_2O$	2.000E+13	0.000	0.000
108.	$C_2H_3 + CH_2 = C_3H_4 + H$	3.000E+13	0.000	0.000
109.	$C_2H_3 + C_2H = C_2H_2 + C_2H_2$	0.300E+14	0.000	0.000
110.	$C_2H_3 + C_2H_3 = CH_2CHCCH_2 + H$	4.000E+13	0.000	0.000
111.	$C_2H_3 + CH = CH_2 + C_2H_2$	0.500E+14	0.000	0.000
112.	$OH + C_2H_2 = C_2H + H_2O$	3.370E+07	2.000	14000.000
113.	$OH + C_2H_2 = HCCOH + H$	5.040E+05	2.300	13500.000
114.	$OH + C_2H_2 = CH_2CO + H$	2.180E-04	4.500	-1000.000
115.	$OH + C_2H_2 = CH_3 + CO$	4.830E-04	4.000	-2000.000
116.	$HCCOH + H = CH_2CO + H$	0.100E+14	0.000	0.000
117.	$C_2H_2 + O = C_2H + OH$	0.316E+16	-0.600	15000.000
118.	$CH_2CO + O = CO_2 + CH_2$	0.175E+13	0.000	1350.000
119.	$CH_2CO + H = CH_3 + CO$	0.113E+14	0.000	3428.000
120.	$CH_2CO + H = HCCO + H_2$	0.500E+14	0.000	8000.000
121.	$CH_2CO + O = HCCO + OH$	0.100E+14	0.000	8000.000
122.	$CH_2CO + OH = HCCO + H_2O$	0.750E+13	0.000	2000.000
123.	$CH_2CO(+M) = CH_2 + CO(+M)$	0.300E+15	0.000	70980.000
	Low Pressure limit: 3.6E15 0.0 59270.			
124.	$C_2H + O_2 = CO + CO + H$	3.520E+13	0.000	0.000
125.	$C_2H + C_2H_2 = C_4H_2 + H$	0.300E+14	0.000	0.000
126.	$HCCO + C_2H_2 = H_2CCCH + CO$	1.000E+11	0.000	3000.000
127.	$H + HCCO = CH_2^1 + CO$	0.100E+15	0.000	0.000
128.	$O + HCCO = H + CO + CO$	0.100E+15	0.000	0.000
129.	$HCCO + O_2 = CO_2 + CO + H$	1.400E+09	1.000	0.000
130.	$CH + HCCO = C_2H_2 + CO$	0.500E+14	0.000	0.000
131.	$HCCO + HCCO = C_2H_2 + CO + CO$	0.100E+14	0.000	0.000
132.	$HCCO + OH = C_2O + H_2O$	3.000E+13	0.000	0.000
133.	$C_2O + H = CH + CO$	5.000E+13	0.000	0.000
134.	$C_2O + O = CO + CO$	5.000E+13	0.000	0.000
135.	$C_2O + OH = CO + CO + H$	2.000E+13	0.000	0.000
136.	$C_2O + O_2 = CO + CO + O$	2.000E+13	0.000	0.000
137.	$CH_2^1 + M = CH_2 + M$	0.100E+14	0.000	0.000
	3rd body efficiencies: H: 0.0, H_2O: 0.0, C_2H_2: 0.0			
138.	$CH_2^1 + CH_4 = CH_3 + CH_3$	0.400E+14	0.000	0.000
139.	$CH_2^1 + C_2H_6 = CH_3 + C_2H_5$	0.120E+15	0.000	0.000
140.	$CH_2^1 + O_2 = CO + OH + H$	7.000E+13	0.000	0.000
141.	$CH_2^1 + H_2 = CH_3 + H$	0.700E+14	0.000	0.000
142.	$CH_2^1 + H_2O = CH_3 + OH$	1.000E+14	0.000	0.000

No.	Reaction	A	n	E_a
143.	$CH_2^1 + H_2O = CH_2 + H_2O$	3.000E+13	0.000	0.000
144.	$CH_2^1 + C_2H_2 = H_2CCCH + H$	1.800E+14	0.000	0.000
145.	$CH_2^1 + C_2H_2 = CH_2 + C_2H_2$	4.000E+13	0.000	0.000
146.	$CH_2^1 + H = CH_2 + H$	0.200E+15	0.000	0.000
147.	$CH_2^1 + O = CO + H + H$	3.000E+13	0.000	0.000
148.	$CH_2^1 + OH = CH_2O + H$	3.000E+13	0.000	0.000
149.	$CH_2^1 + H = CH + H_2$	3.000E+13	0.000	0.000
150.	$CH_2^1 + CO_2 = CH_2O + CO$	3.000E+12	0.000	0.000
151.	$CH_2^1 + CH_3 = C_2H_4 + H$	2.000E+13	0.000	0.000
152.	$CH_2^1 + CH_2CO = C_2H_4 + CO$	1.600E+14	0.000	0.000
153.	$C_2H + O = CH + CO$	0.500E+14	0.000	0.000
154.	$C_2H + OH = HCCO + H$	0.200E+14	0.000	0.000
155.	$C_2H + OH = C_2 + H_2O$	4.000E+07	2.000	8000.000
156.	$C_2 + H_2 = C_2H + H$	4.000E+05	2.400	1000.000
157.	$C_2 + O_2 = CO + CO$	5.000E+13	0.000	0.000
158.	$C_2 + OH = C_2O + H$	5.000E+13	0.000	0.000
159.	$CH_2 + CH_2 = C_2H_2 + H + H$	0.400E+14	0.000	0.000
160.	$CH_2 + HCCO = C_2H_3 + CO$	0.300E+14	0.000	0.000
161.	$CH_2 + C_2H_2 = H_2CCCH + H$	0.120E+14	0.000	6600.000
162.	$C_4H_2 + OH = H_2C_4O + H$	0.666E+13	0.000	-410.000
163.	$C_3H_2 + O_2 = HCCO + CO + H$	5.000E+13	0.000	0.000
164.	$C_3H_2 + OH = C_2H_2 + HCO$	5.000E+13	0.000	0.000
165.	$C_3H_2 + CH_2 = H_2CCCCH + H$	3.000E+13	0.000	0.000
166.	$H_2C_4O + H = C_2H_2 + HCCO$	5.000E+13	0.000	3000.000
167.	$H_2C_4O + OH = CH_2CO + HCCO$	1.000E+07	2.000	2000.000
168.	$H_2CCCH + O_2 = CH_2CO + HCO$	0.300E+11	0.000	2868.000
169.	$H_2CCCH + O = CH_2O + C_2H$	0.200E+14	0.000	0.000
170.	$H_2CCCH + H = C_3H_2 + H_2$	5.000E+13	0.000	3000.000
171.	$H_2CCCH + OH = C_3H_2 + H_2O$	0.200E+14	0.000	0.000
172.	$H_2CCCH + CH_2 = CH_2CHCCH + H$	4.000E+13	0.000	0.000
173.	$H_2CCCH + CH = HCCHCCH + H$	7.000E+13	0.000	0.000
174.	$H_2CCCH + CH = H_2CCCCH + H$	7.000E+13	0.000	0.000
175.	$CH_2CHCCH + OH = HCCHCCH + H_2O$	7.500E+06	2.000	5000.000
176.	$CH_2CHCCH + H = HCCHCCH + H_2$	2.000E+07	2.000	15000.000
177.	$CH_2CHCCH + OH = H_2CCCCH + H_2O$	1.000E+07	2.000	2000.000
178.	$H + HCCHCCH = H_2CCCCH + H$	1.000E+14	0.000	0.000
179.	$H_2CCCCH + O_2 = CH_2CO + HCCO$	1.000E+12	0.000	0.000
180.	$H_2CCCCH + OH = C_4H_2 + H_2O$	3.000E+13	0.000	0.000
181.	$H_2CCCCH + O = CH_2CO + C_2H$	2.000E+13	0.000	0.000
182.	$H_2CCCCH + O = H_2C_4O + H$	2.000E+13	0.000	0.000
183.	$H_2CCCCH + H = C_4H_2 + H_2$	5.000E+13	0.000	0.000
184.	$H_2CCCCH + CH_2 = C_3H_4 + C_2H$	2.000E+13	0.000	0.000
185.	$CH_2CHCCH + H = H_2CCCCH + H_2$	3.000E+07	2.000	5000.000
186.	$CH_2CHCHCH + OH = CH_2CHCCH + H_2O$	2.000E+07	2.000	1000.000
187.	$CH_2CHCHCH + H = CH_2CHCCH + H_2$	3.000E+07	2.000	1000.000
188.	$C_6H_6 + H = C_6H_5 + H_2$	3.000E+07	2.000	5000.000
189.	$C_6H_6 + OH = C_6H_5 + H_2O$	7.500E+06	2.000	5000.000
190.	$C_2H_3 + C_2H_2 = CH_2CHCCH + H$	2.000E+12	0.000	5000.000
191.	$C_2H_2 + CH_2CHCHCH = C_6H_6 + H$	2.800E+03	2.900	1400.000
192.	$HCCHCCH + C_2H_2 = C_6H_5$	2.800E+03	2.900	1400.000
193.	$C_3H_4 + H = H_2CCCH + H_2$	5.000E+07	2.000	5000.000
194.	$C_3H_4 + OH = H_2CCCH + H_2O$	2.000E+07	2.000	1000.000
195.	$C_3H_4P + H = H_2CCCH + H_2$	5.000E+07	2.000	5000.000

No.	Reaction	A	n	E_a
196.	$C_3H_4P + H = CH_3 + C_2H_2$	1.000E+14	0.000	4000.000
197.	$C_3H_4P + OH = H_2CCCH + H_2O$	2.000E+07	2.000	1000.000
198.	$C_6H_5 + OH = C_6H_5O + H$	5.000E+13	0.000	0.000
199.	$C_6H_5 + O_2 = C_6H_5O + O$	1.000E+13	0.000	0.000
200.	$CH_2 + C_4H_2 = C_5H_3 + H$	0.130E+14	0.000	4326.000
201.	$CH + C_4H_2 = C_5H_2 + H$	0.100E+15	0.000	0.000
202.	$CH_2^1 + C_4H_2 = C_5H_3 + H$	0.300E+14	0.000	0.000
203.	$C_4H_2 + O = C_3H_2 + CO$	0.120E+13	0.000	0.000
204.	$C_4H_2 + C_2H = C_6H_2 + H$	0.400E+14	0.000	0.000
205.	$C_2H_2 + O_2 = HCCO + OH$	0.200E+09	1.500	30100.000
206.	$C_2H_2 + M = C_2H + H + M$	0.420E+17	0.000	107000.000
207.	$C_2H_4 + M = C_2H_2 + H_2 + M$	0.150E+16	0.000	55800.000
208.	$C_2H_4 + M = C_2H_3 + H + M$	0.140E+17	0.000	82360.000
209.	$C_2H_3 + C_2H_4 = CH_2CHCHCH_2 + H$	3.000E+12	0.000	1000.000
210.	$CH_2CHCHCH_2 + H = CH_2CHCHCH + H_2$	3.000E+07	2.000	13000.000
211.	$CH_2CHCHCH_2 + H = CH_2CHCCH_2 + H_2$	3.000E+07	2.000	6000.000
212.	$CH_2CHCHCH_2 + OH = CH_2CHCHCH + H_2O$	2.000E+07	2.000	5000.000
213.	$CH_2CHCHCH_2 + OH = CH_2CHCCH_2 + H_2O$	2.000E+07	2.000	2000.000
214.	$CH_2CHCHCH + H = CH_2CHCCH_2 + H$	1.000E+14	0.000	0.000
215.	$H_2CCCCH(+M) = C_4H_2 + H(+M)$	1.000E+14	0.000	55000.000
	Low Pressure limit: 2.0E15 0.0 48000.			
216.	$HCCHCCH(+M) = C_4H_2 + H(+M)$	1.000E+14	0.000	36000.000
	Low Pressure limit: 1.0E14 0.0 30000.			
217.	$CH_2CHCCH_2(+M) = CH_2CHCCH + H(+M)$	1.000E+14	0.000	50000.000
	Low Pressure limit: 2.0E15 0.0 42000.			
218.	$CH_2CHCHCH(+M) = CH_2CHCCH + H(+M)$	1.000E+14	0.000	37000.000
	Low Pressure limit: 1.0E14 0.0 30000.			
219.	$H + C_6H_5 = C_6H_6$	5.000E+13	0.000	0.000

Bibliography

[1] W. Eversole, Synthesis of Diamond; U.S. Patents 3,030,187 and 3,030,188, 1962.

[2] A. R. Badzian and R. C. DeVries, Mat. Res. Bull. **23**, 385 (1988).

[3] S. J. Harris and A. M. Weiner, J. Appl. Phys. **70**, 1385 (1991).

[4] L. R. Martin and M. W. Hill, J. Mater. Sci. Lett. **9**, 621 (1990).

[5] S. J. Harris and L. R. Martin, J. Mater. Res. **5**, 2313 (1990).

[6] M. H. Loh and M. A. Cappelli, Diamond and Related Materials **2**, 454 (1993).

[7] M. Frenklach and K. E. Spear, J. Mater. Res. **3**, 133 (1991).

[8] M. Frenklach and H. Wang, Phys. Rev. B **43**, 1520 (1991).

[9] S. J. Harris, Appl. Phys. Lett. **56**, 2298 (1990).

[10] D. N. Belton and S. J. Harris, J. Chem. Phys. **96**, 2371 (1992).

[11] B. J. Garrison, E. J. Dawnkaski, D. Srivastava, and D. W. Brenner, Science **255**, 835 (1992).

[12] D. G. Goodwin, J. Appl. Phys. **74**, 6888 (1993).

[13] Y. Hirose and M. Mitsuizumi, New Diamond **4**, 34 (1988).

[14] Y. Tzeng, C. Cutshaw, R. Phillips, and T. Srivinyunon, Appl. Phys. Lett. **56**, 134 (1990).

[15] Y. Matsui, A. Yuuki, M. Sahara, and Y. Hirose, Jpn. J. Appl. Phys. **28**, 1718 (1989).

[16] L. M. Hanssen, W. A. Carrington, J. E. Butler, and K. A. Snail, Mater. Lett. **7**, 289 (1990).

[17] M. A. Cappelli and P. H. Paul, J. Appl. Phys. **67**, 2596 (1990).

[18] K. A. Snail *et al.*, Carbon **28**, 794 (1990).

[19] L. M. Hanssen *et al.*, Thin Solid Films **196**, 271 (1991).

[20] K. A. Snail, J. A. Freitas, Jr., C. L. Void, and L. M. Hanssen, in *Proc. 2nd Intl. Symp. Diamond and Related Materials*, edited by A. J. Purdes *et al.* (The Electrochemical Society, Pennington, NJ, 1991), pp. 81–90.

[21] K. Komaki, M. Yanagisawa, I. Yamamoto, and Y. Hirose, Jpn. J. Appl. Phys. **32**, 1814 (1993).

[22] Y. Matsui, H. Yabe, T. Sugimoto, and Y. Hirose, Diamond and Related Materials **1**, 19 (1991).

[23] P. W. J. Morrison, J. E. Cosgrove, J. R. Markhan, and P. R. Solomon, in *Proc. 2nd Intl. Conf. New Diamond Sci. Tech.*, edited by R. Messier, J. T. Glass, J. E. Butler, and R. Roy (Materials Research Society, Pittsburgh, PA, 1991), pp. 219–224.

[24] E. Meeks, R. J. Kee, D. S. Dandy, and M. E. Coltrin, Combustion and Flame **92**, 144 (1993).

[25] D. G. Goodwin, Appl. Phys. Lett. **59**, 277 (1991).

[26] K. V. Ravi, C. A. Koch, and D. Olson, in *Proc. 2nd Int. Conf. Appl. Diamond Films and Related Materials*, edited by M. Yoshikawa, M. Murakawa, Y. Tzeng, and W. A. Yarbrough (MYU, Tokyo, 1993), pp. 491–496.

[27] M. Murayama and K. Uchida, Combustion and Flame **91**, 239 (1992).

[28] K. F. McCarty, E. Meeks, R. J. Kee, and A. E. Lutz, Appl. Phys. Lett. **63**, 1498 (1993).

[29] J. A. Cooper, Jr. and W. A. Yarbrough, in *Diamond Optics III (SPIE Proceedings Vol. 1325)*, edited by A. Feldman and S. Holly (SPIE, Bellingham, Washington, 1990), pp. 41–54.

[30] J. D. Bittner, Ph.D. thesis, Massachusetts Institute of Technology, 1981.

[31] S. J. Harris and A. M. Weiner, J. Appl. Phys. **67**, 6520 (1990).

[32] D. G. Goodwin and G. G. Gavillet, J. Appl. Phys. **68**, 6393 (1990).

[33] T. von Kármán, Zeit. f. Angew. Math. u. Mech. **1**, 70 (1921).

[34] G. Evans and R. Greif, Trans. ASME **109**, 928 (1987).

[35] R. J. Kee, J. A. Miller, G. H. Evans, and G. Dixon-Lewis, in *Twenty-second Symposium (International) on Combustion* (The Combustion Institute, Pittsburgh, Pa., 1988), pp. 1479–1494.

[36] R. J. Kee *et al.*, Technical Report No. SAND86-8246, Sandia National Laboratories (unpublished).

[37] J. A. Miller and C. F. Melius, Comb. Flame **91**, 21 (1992).

[38] J. A. Miller and C. T. Bowman, Prog. Energy Combust. Sci. **15**, 287 (1989).

[39] J. Fleming, K. A. Burton, and H. D. Ladouceur, Chem. Phys. Lett. **175**, 395 (1990).

[40] J. S. Bernstein *et al.*, Combustion and Flame **92**, 85 (1993).

[41] J. A. Miller *et al.*, in *Twenty-third Symposium (International) on Combustion* (The Combustion Institute, Pittsburgh, Pa., 1990), p. 187.

[42] S. J. Harris and A. M. Weiner, J. Appl. Phys. **74**, 1022 (1993).

[43] L. N. Krasnoperov, I. J. Kalinovski, H. N. Chu, and D. Gutman, J. Phys. Chem. **97**, 11787 (1993).

[44] Q. Sun and M. Alam, J. Electrochem. Soc. **139**, 933 (1992).

[45] J. S. Kim and M. A. Cappelli, J. Appl. Phys. **72**, 5461 (1992).

[46] N. G. Glumac and D. G. Goodwin, Materials Letters **18**, 119 (1993).

[47] M. D. Smooke, J. Crump, K. Seshadri, and V. Giovangigli, in *Twenty-third Symposium (International) on Combustion* (The Combustion Institute, Pittsburgh, Pa., 1990), p. 463.

[48] K. J. Rensberger *et al.*, Appl. Opt. **28**, 3556 (1989).

[49] V. Huong, Diamond and Related Materials **1**, 33 (1991).

[50] J. Wei, J. M. Chang, and Y. Tzeng, Thin Solid Films **212**, 91 (1992).

[51] W. L. Hsu, Appl. Phys. Lett. **59**, 1427 (1991).

[52] T. Kawato and K. Kondoh, Jpn. J. Appl. Phys. **26**, 2429 (1987).

[53] A. Joshi, R. Nimmagada, and J. Herrington, J. Vac. Sci. and Tech. A - Vacuum Surfaces and Films **8**, 2137 (1992).

[54] E. Kondoh, T. Ohta, T. Mitomo, and K. Ohtsuka, Appl. Phys. Lett. **59**, 488 (1991).

[55] C. J. Chu, R. H. Hauge, J. L. Margrave, and M. P. D'Evelyn, Appl. Phys. Lett. **61**, 1393 (1992).

[56] D. D. Koleske and S. M. Gates, J. Chem. Phys. **99**, 5619 (1993).

[57] M. Green, K. R. Jennings, J. W. Linnett, and D. Schofield, Trans. Faraday Soc. **55**, 2152 (1959).

[58] W. V. Smith, J. Chem. Phys. **11**, 110 (1943).

[59] S. J. Harris and A. M. Weiner, Appl. Phys. Lett. **55**, 2179 (1989).

[60] S. J. Harris, A. M. Weiner, R. J. Blint, and J. E. M. Goldsmith, in *Twenty-first Symposium (International) on Combustion* (The Combustion Institute, Pittsburgh, PA, 1986), p. 1033.

[61] S. J. Harris, A. M. Weiner, and T. A. Perry, Appl. Phys. Lett. **53**, 1605 (1988).

[62] F. G. Celii and J. E. Butler, J. Appl. Phys. **71**, 2877 (1992).

[63] E. J. Corat and D. G. Goodwin, J. Appl. Phys. **74**, 2021 (1993).